An Investigation into Nucleosynthesis in Common Envelope Neutron Star Systems

James Douglas Keegans

MSc by Research

University of York

Physics

January 2017

Abstract

In this thesis, the burning processes in common envelope neutron star systems are investigated. The production of key isotopes which have been shown to be overproduced in observations of HV2112 is investigated, and finds that for a large range of accretion rates and depths into the neutron star envelope, significant enrichment in these elements is achieved. The production of p nuclei is also looked and it is found that at an accretion rate of $\dot{M} = 10^3 M_\odot/yr$, 7 of the investigated isotopes are significantly enriched in the processed material. Finally, the extent of nucleosynthesis for different accretion rates and depths is discussed and it is found that for a wide range of these parameters nucleosynthesis proceeds into the A $\approx$ 130 mass range, unexpected in the rp-process due to α unbound cycles. This may indicate the action of α capture and provides a method for the synthesis of massive, proton rich nuclei. Further study would be necessary to determine the exact increase of material in this mass range. These results together provide a possibility for observational candidates in the spectrum of HV2112, and also motivation for a full hydrodynamic model of the system to fully investigate the nucleosynthesis in the system.

Contents

List of Figures

Acknowledgements

I would like to thank the members of the NuGrid collaboration, for all the help they have provided. I would like to thank my supervisor Dr. Laird, for her support and patience over the last year. And I would like to thank my family, for their continued berating to ensure that I actually produced something.

i mam, yr wyf yn dweud i chi byddwn i'n gorffen

Declaration

I declare that all work presented as my own contained in this thesis is original and has not been submitted for assessment at any university for any degree. Images and work reproduced from published work have been indicated as appropriate. I am the sole author.

Chapter 1

Introduction

"In the beginning there was nothing, which exploded"

- Terry Pratchett, Lords and Ladies

1.1 Introduction

The goal of this thesis is to identify the main burning products in common envelope neutron star (CENS) systems - a proposed astrophysical site in which a neutron star spirals through the envelope of a massive companion, such as a red supergiant, accreting material from the envelope of the companion. These astrophysical systems provide extreme conditions where proton rich nuclei may be synthesised in nature, due to the high temperatures and access to hydrogen and helium fuel accreted from the envelope of the companion star.

Beginning in 1957 with the work of Burbidge, Burbidge, Fowler and Hoyle [12], our understanding of the origin of the elements and isotopes present in nature has improved and developed. Current theories can explain the presence of a wide variety of these naturally occurring isotopes, through the action of hydrostatic burning and the s- and r- processes however there remain isotopes, particularly those which are proton rich, who's origin is not clear.

Investigations into common envelope systems have been concluded previously. Taam, Bodenheimer

and Ostriker [13], explored the evolution of a 1 $M_{\odot}$ neutron star and a 16$M_{\odot}$ companion. They concluded that such a system will eventually end it's life in one of two ways:

1. The ejection of the companion envelope

2. Core merger and the subsequent production of a TŻO

So-called Thorne-Żytkow objects (TŻOs) were first propoesd by Kip Thorne and Anna Żytkow in 1975, and consist of a giant or supergiant star with a neutron star core [14]. Ejection of the envelope results, eventually, in an event observable with a gravitational wave detector, such as LIGO (discussed in section 2.4) where the compact remnants of the two stars coalesce. Core merger results in the formation of a Thorne-Żytkow object [15] which is very difficult to identify observationally as it's spectral features are expected to be very similar to those of a regular red supergiant [1]. Thorne-Żytkow objects are known to have many problems relating to the stability of the system and as such are not expected to survive for any significant length of time - Podsiadlowski et al [16] states a characteristic lifetime for TŻOs of around 100 years however, this is calculated assuming an accretion rate of 10^{-6} as a maximum, which may not be physical as they neglect the effect of neutrino cooling on the accretion rate. Despite the problems associated with TŻOs, as a transient common envelope system it presents a unique environment for the production of proton rich nuclei.

In this thesis, a brief (and necessarily incomplete) introduction to the astrophysical conditions and relevant nuclear physics of common envelope systems is presented, and the results of the 50 mass accretion rate and depths analysed. The goal of this is to find which, if any, of the products of the rp-process might be produced in the common envelope system and whether this presents a viable site to explain their abundances in stellar material.

1.2 Observations and Motivation

The observations of the Thorne-Żytkow object candidate HV2112 in the Small Magellanic Cloud by Levesque et al [1] provided strong evidence to support it's possible nature as a TŻO. Over-abundances of

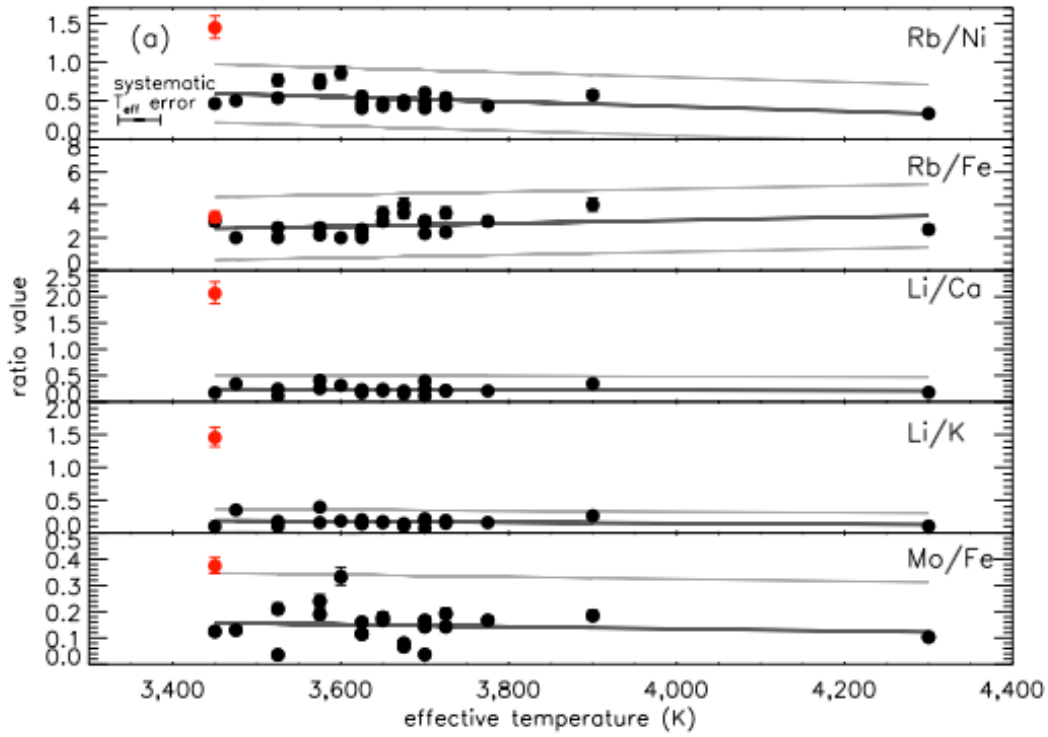

Figure 1.1: Line ratios for Small Magellanic Cloud RSGs, showing features expected to be enhanced in a TŻO. The line ratios of HV2112 are the data in red. It can be seen that the Rb/Ni, Li/Ca and Mo/Fe lines all lie outside the 3σ limit (light grey lines). Reproduced from [1]

the elements Rb, Li and Mo were consistent with previous models of TŻOs, enhancements which are not predicted to occur in any other stellar environment. The observations for Rb, Li and Mo are presented in Figure 1.1, reproduced from [1].

Difficulty with this model however arises due to the unexpected spectral features present in the spectrum of HV2112 - an enhancement of K and Ca lines which is present in none of the previous work undertaken to model the system. These results are reproduced in Figure 1.2. There is also a strong Balmer emission observed however it is not the intent of this thesis to explain the origin of these emission lines.

Levesque et al propose that updated mixing regimes used in modelling the environment may improve agreement with observations, along with the more extensive reaction networks that would allow a more flexible and comprehensive description of the nucleosynthetic processes under way in such a burning regime. Both more extensive reaction networks and new models of mixing in stellar environments have become available since the first work on TŻOs was carried out in 1977 [15], however there are a number

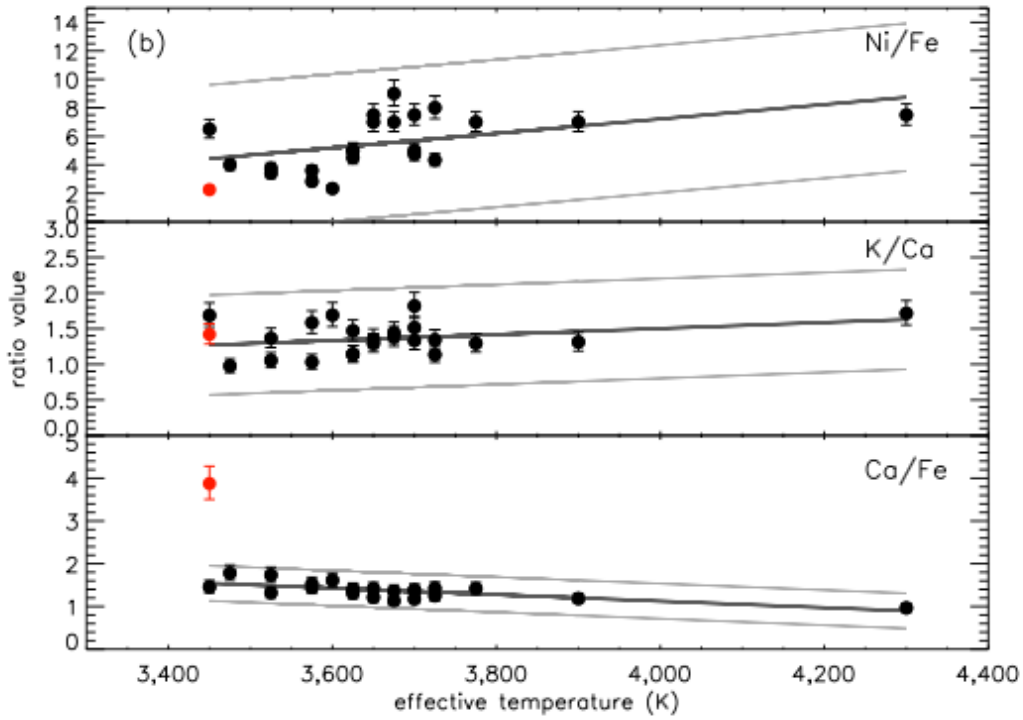

Figure 1.2: Line ratios for Small Magellanic Cloud RSGs, showing the enhancement of line ratios for K and Ca. Reproduced from [1]

of problems with the standard TŻO model - for instance it is predicted to be unstable on short time-scales (for a fuller discussion see section 3.5).

The transient common envelope scenario incorporates aspects of the TŻO model - hydrogen rich fuel and temperatures of $T_9 > 1$ - which make it a strong candidate for the site of production of rp-process material. As an alternative or precursor to the TŻO stage of a binary system it offers a possible accretion stage under stable conditions, allowing more material to be produced before the neutron star collapses or disrupts the companion star. As such, it is an exciting environment that presents an alternative or complimentary system to the TŻO, and allows for the study of exotic burning conditions.

1.3 Outline of Thesis

Chapter 2 will outline the astrophysical background for the project, describing the properties of the red supergiant companion in section 2.2.1 and the neutron star in section 2.2.3. Next, section 2.3 describes how the extreme temperature and density conditions in the CENS system are achieved, through the accretion

of material into the strong gravitational field of the neutron star, and conversion of gravitational potential energy to kinetic. Section 2.3 will also describe the effect that neutrinos have on the system - specifically in allowing accretion rates higher than Eddington in section 2.3.2 and the effect on the temperature in the system of neutrino losses in section 2.3.4. Finally in section 2.4, the role of gravitational waves in finding the remnants of common envelope systems is briefly discussed.

Chapter 3 introduces the nuclear theory relevant to this investigation. Section 3.2 gives an overview of reaction rates in stellar environments, section 3.3 discusses hydrostatic burning and section 3.4 goes on to describe key aspects of the rp-process.

Chapter 4 describes the NuGrid codes, and section 4.5 outlines how the trajectories for these simulations have been produced. Results are presented in chapter 5 and conclusions and ideas for future work in chapter 6.

Chapter 2

Astrophysical Theory

2.1 Overview

The evolution of a star is governed by a number of different factors - it's mass, metalicity, rotation and whether it forms as part of a binary system, as well as others. The first stars in our universe were formed from the products of nucleosynthesis during the big bang, with essentially zero metalicity. Each subsequent generation of stars is formed from the ashes of the previous one, along with fresh hydrogen fuel. In this way, the metalicity of the universe has increased and become increasingly more diverse, as different stellar environments have contributed to it.

In a star, lighter elements are fused together to release energy and halt the collapse of the whole under gravity. This must eventually fail as the star runs out of fuel to burn, resulting in the collapse and death of the star. Depending on the mass of the system under consideration this death can vary significantly, from the relatively quiet white dwarf to the violent supernova explosion. It is necessary when describing the common-envelope neutron star (CENS) system to consider the lives of both the neutron star progenitor and the red super giant, their burning pathways and products and their physical properties in order to understand the conditions in which the transient phase of the system may take place.

In this section the properties and evolution of the stars of the binary system are discussed - factors such as their radii and chemical composition; the likely masses of the progenitor star and the companion

are identified in order to better describe the conditions in the transient system; and the properties of the compact object remnant are presented as this is vital to an accurate description of the burning conditions. In section 2.3, the accretion onto the compact object is discussed, and it's role as a very efficient source of heating considered. Section 2.4 briefly outlines the possibility of observing gravitational waves from the remnants of these systems, as this constitutes one of the most rigourous methods of identifying these systems unambiguously.

The theoretical background describing Thorne-Żytkow Objects was first developed by Thorne and Żytkow in 1975 [14]. In this paper the model of a central neutron star accreting matter was investigated, and it was concluded that, in this regime, there were two possible methods of generating the energy required for a stable envelope, which depended on the size of the companion. For a comparatively small companion - a red giant - the bigest contribution to energy generation was found to be from accretion onto the neutron star core. For larger companions, in the form of red super giants, the energy generation needed to support the convective envelope was thought to be provided by nuclear burning in a thin shell around the neutron star. In this first paper however, and in subsequent work (for instance Refs [15] and [17]) many difficulties with the formation and stability of the TŻO have been identified - collapse of the central NS to form a black hole, instabilities due to neutrino losses and the method of formation being a few.

Despite the difficulties with a theoretical description of the TŻO environment, the observational evidence for this has grown over the last few years. The work of Levesque et al [1] identified a red super giant candidate with spectral features in line with those expected (although with aditional features, see below). Despite subsequent challenges to the validity of these observations [18], further analysis of the data confirmed the original placement of the candidate in the Small Magellanic Cloud [19] and so support the hypothesis that this is a TŻO-like star.

It is because of these difficulties with the stability of the TŻO, and the discrepancies with the theoretical yields and the spectrum of HV2112, that efforts towards a modified model of the TŻO have been made. The scenario presented in this work is that of a common envelope transient, where the neutron star is travelling through the red super giant companion. This system is expected to be stable for around 1 year,

as the neutron star in the envelope spirals inwards and merges or interacts with the core of the companion star.

2.2 Formation and Properties of the Neutron Star RSG System

2.2.1 The Red Super Giant

A red supergiant star is a cool, massive star with surface temperature in the region of 5000k. They can be difficult to identify experimentally due to the similarities with less massive but closer stars [20]. The largest theoretical radius for a red supergiant is around 1500 $R_{\odot}$ but typically lie around 700 $R_{\odot}$. At this size, If a red supergiant were to sit in our solar system at the current position of the sun, it's surface would sit almost exactly at the outer edge of the asteroid belt between Mars and Jupiter. A red super giant is nearing the end of its life, having exhausted its core hydrogen fuel. Core burning continues, preventing collapse, with the extended massive hydrogen envelope (and helium envelope if the star is sufficently massive and old) being weakly gravitationally bound. Burning in the cores of these stars ends in production of the iron group elements and eventual core collapse. AGB stars lie in the mass range of approximately 1-10 $M_{\odot}$ and constitute the end stages of burning for stars of intermediate mass [21], they form from from less massive progenitors than the red supergiants, have smaller radii and are less luminous.

A full description of these stars is difficult, mixing and dredging in the envelope results in very complicated and difficult to model phenomena [22] [21]. Multi zone post processing, sophisticated hydrodynamics simulations and mixing theories are required to adequately describe stars in this mass range. However, due to the high temperatures in the CENS system it is likely to be sufficient for this investigation to treat the material as having approximately solar metalicity. As the material enters NSE the effect of initial metalicity is minimised as nuclei are in equilibrium determined by their nuclear properties. Having an initial solar metalicity also allows easier analysis and comparison with the observations, as enhancements in the spectrum of HV2112 are relative to solar abundances. Seed nuclei in the CNO mass

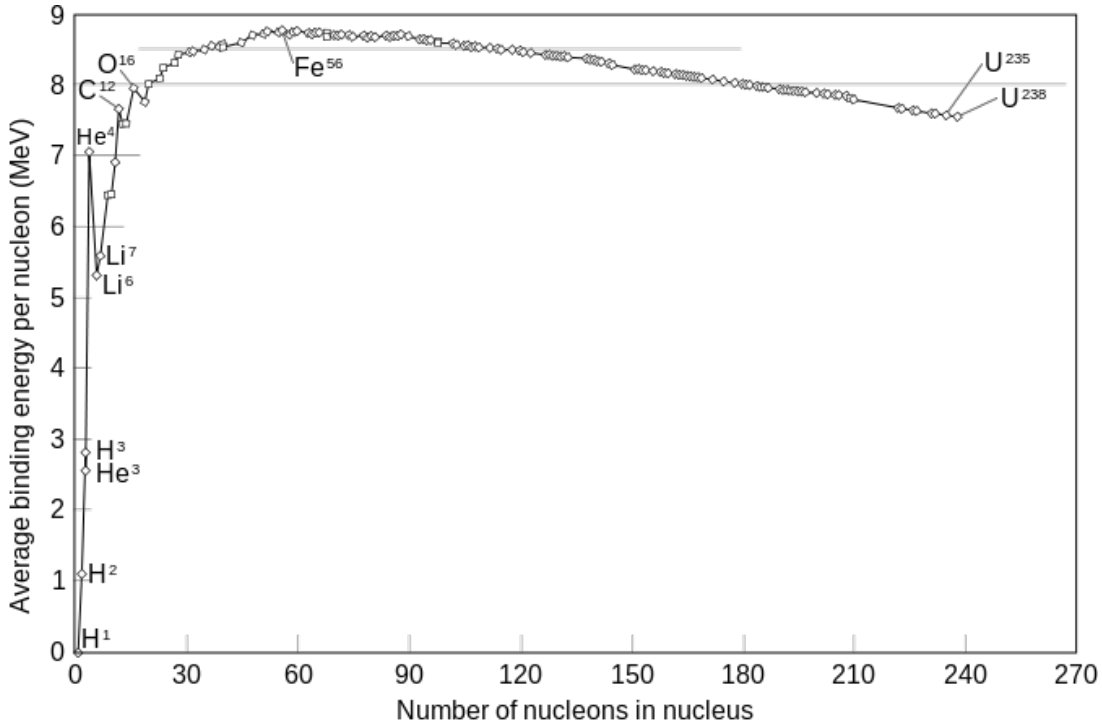

Figure 2.1: The binding energy curve shows a broad maximum around ^{56}Fe. These 'iron group' isotopes have binding energies $\approx$ 8.8MeV and represent the most tightly bound nuclei. As such, once these have been synthesised in a stellar interior, no further energy can be liberated by the fusion of material to higher masses.

region to facilitate production of higher mass nuclei, and higher mass material with A > 130, beyond the α unbound SnSbTe cycle, may have a significant effect in the lower temperature burning regions, where material does not enter NSE however, initial abundances for HV2112 were not available and therefore solar matalicity was seen as the most appropriate choice, thanks to the benefits it offers with regards to data analysis.

2.2.2 The Neutron Star

A neutron star is formed in the final stages of life of a massive star. The progenitor star has fused nuclei in it's core to Fe group isotopes, which have the largest binding energy per nucleon(see figure 2.1). This means that no further nuclear energy can be liberated from the material, and there is therefore no outward force to resist gravitational collapse. Material is accreted onto this inert core and, when the mass of the core increases sufficiently, induces a collapse [3].

Material in the core increases in density during the collapse until it increases past the nuclear density.

Once this occurs there is a bounce, and a shockwave propagates through the star, ejecting material in a supernovae explosion. The exact mechanism for this is not clear, and may be dependent on many aspects such as neutrino interactions [23] or acoustic modes of the remnant object [24], however for the purposes of this project it is sufficient to know that the outer layers of the star are ejected, and the compact core in the form of a neutron star remains (if the fall back of material is not too great so as to form a black hole [3]). Fryxell and Arnette [25] find that the effect on the companion of this explosion is small, and the ejected shell of material does not disrupt the binary system. Kalogera [26] discusses the effect of supernova explosions with kicks and also finds that these systems can survive, although there is a dependence on the masses of the progenitors which determines the fraction which do. Both these findings support the possibility that these common envelope systems can form.

The neutron star is supported by neutron degeneracy pressure, analogous to the electron degeneracy pressure in a white dwarf. The pressure exerted by the neutrons is much larger however due to their larger mass and they can therefore support a larger upper mass than electron degeneracy pressure can.

Taking into consideration the mass range available for the red super giant (9-25$M_{\odot}$), we can conclude that the progenitor of the compact object in a binary system must be more massive than the companion, as it must exhaust its fuel first, and that the lower limit for this mass is greater than 9 $M_{\odot}$. Heger et. al. [2] present the expected remnants from stars of various masses and metalicities (Figure 2.2). It is not therefore unresonable to expect the progenitor of the NS to be a star of $\approx$11 $M_{\odot}$ for a 9 $M_{\odot}$ companion star, although no hard limit to the NS progenitor mass can be supplied at this time, other than that it be lower than the 25$M_{\odot}$ upper limit shown in Figure 2.2.

The large extent of the RSG envelope allows for the possibility of a common envelope phase during the evolution of the binary system. As stars above 25 $M_{\odot}$ are rare, the most likely masses for the progenitor star are between 9 and 25 $M_{\odot}$

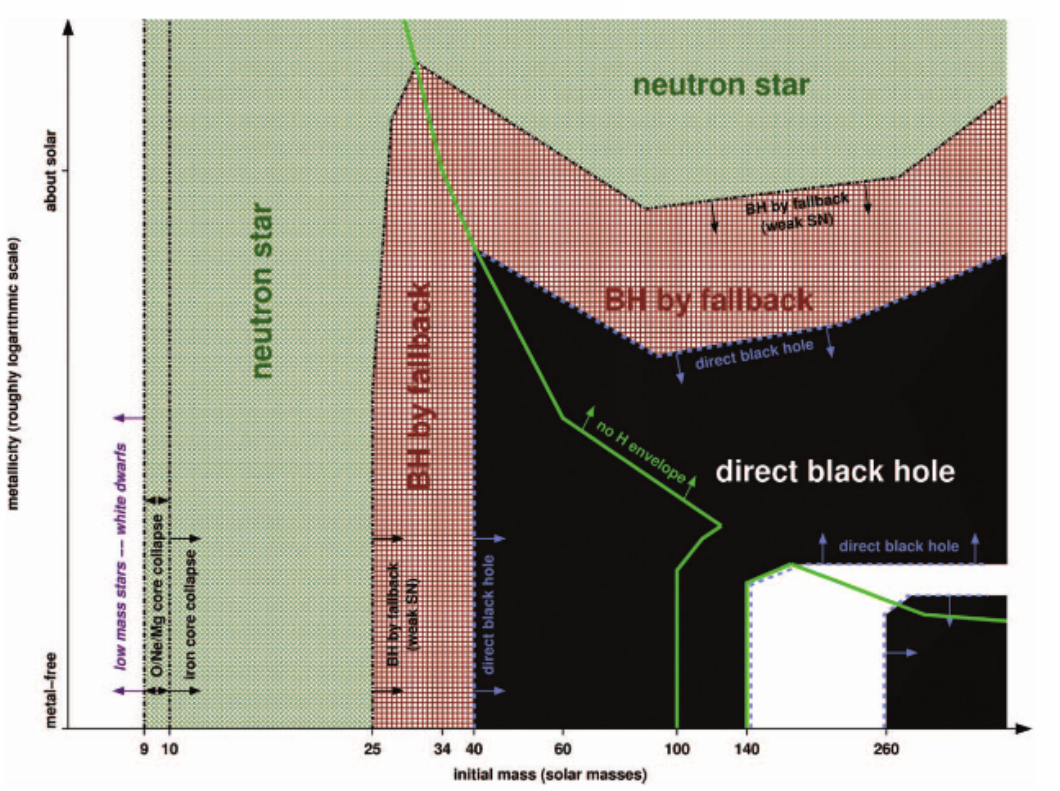

Figure 2.2: Graph showing the dependency on metalicity and progenitor mass of the final remnant object. Reproduced from [2]. It can be seen that a large range of masses would allow a NS remnant to be formed given the constraints outlined above. At all metalicities of the progenitor it would be possible to form a neutron star remnant.

2.2.3 Neutron Star Properties

The properties of the neutron star are critical in determining the temperature and density conditions during burning, details of this are presented in section 2.3. Lipunov [27] identifies four important observable parameters of the neutron star. These are:

1. The mass
2. The radius
3. The moment of inertia
4. The Tolman-Oppenheimer-Volkoff limit

The Tolman-Oppenheimer-Volkoff limit is given by the Tolman-Oppenheimer-Volkoff equations (TOV) which describe the hydrostatic equilibrium conditions for compact objects and other relativistic

objects [3]. They are a series of 4 equations, and add four corrections to classical hydrodynamics. Further discussion of these will not be pursued as their impact on the burning conditions is not important.

The two parameters which influence the burning conditions in the system are the mass and radius of the neutron star, the mass as this prescribes the potential well of the system, and the radius as this dictates how deeply into this potential well the accreting material can fall.

Both of these conditions are constrained by nuclear physics, specifically through considerations of the nuclear equation of state and the compresibility of nuclear matter (see, for example, [28]). Observations have shown that the masses of all known binary neutron stars lie between $1.25 - 1.44 M_{\odot}$ [3] and that the typical radius of a neutron star is approximately 10km.

The mass-radius relationship of neutron stars is illustrated in Figure 2.3. The curves labeled SLy4 and FPS refer to different equations of state describing the NS, and give the mass radius relationship under these conditions. It can be seen that the radius decreases steaply with increasing mass below $0.3 M_{\odot}$. In the mass range of $\approx$ 1.25 - 1.44 $M_{\odot}$ the radius the radius decreases much more slowly to between 10-12 km. A lower value of 10 km was chosen for the CENS investigation, as this is close to the lower limit of the radius of the neutron star. Smaller radii than this would clearly be unphysical. Figure reproduced from [3]

2.3 Accretion

2.3.1 Energy Generation Through Accretion

Accretion onto a compact object represents an efficient method of generating energy. Frank, King and Raine [29] give the energy yielded from accretion onto a neutron star of $1 M_{\odot}$ and R = 10 km to be approximately 20 times that of fusion of hydrogen to helium for the same unit mass. This must be an undermestimate for real neutrons stars however, as all measured masses of neutron stars have been larger than this. Lipunov [27] presents a similar argument, giving the efficiency of accretion as 100 times that of nuclear fusion. A slightly modified argument is presented to illustrate this.

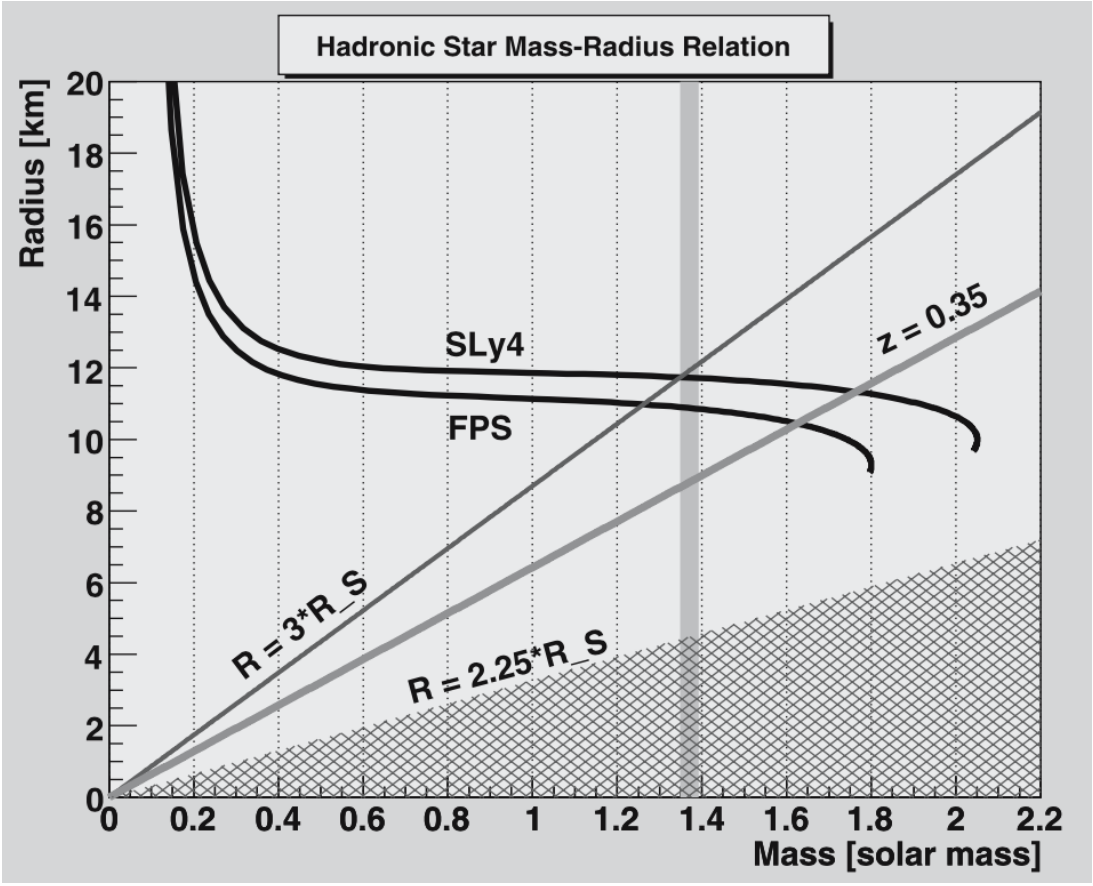

Figure 2.3: Mass-radius relationship for neutron stars. It can be seen that in the mass range where all observed neutron star masses lie, the radius of the neutron star lies between approximately 10-12 km. Reproduced from [3]

Imagine a small mass of material m, falling onto the surface of a neutron star. The gravitational energy release by this in-fall is given by the equation:

$$\Delta E_{acc.} = \frac{GM_{NS}m}{R_{NS}}$$

Where M_{NS} is the mass of the neutron star, m is the mass of in-falling material and R_{NS} is the radius of the neutron star. The energy released from nuclear fusion is given by:

$$\Delta E_{fus.} = \Delta mc^2$$

where Δm is the change in mass of the material. The energy released in the fusion of 4 ^{1}H particles to one ^{4}He is 26.7 MeV [7], meaning that the energy per nucleon released is 6.675 MeV. Taking a NS mass of 1.4 $M_\odot$ mass and 10km radius, the energy released from the in-fall of one atomic mass unit of

mass is 137 MeV. Clearly the energy evolved by accretion into the gravitational well of the neutron star is much larger than that from fusion. As such, this environment has the potential to produce extreme nucleosynthetic conditions necessary for the production of the proton rich material of the rp-process.

2.3.2 The Eddington Limit

The Eddington luminosity is the luminosity beyond which accretion is halted by the outward radiation pressure provided by the object. The Eddington luminosity depends on three factors:

1. The mass of the accreting object
2. The luminosity
3. The oppacity of the accreted material

The gravitational force exerted by a neutron star of mass M_{NS} is given by:

$$F_{grav} = \frac{GM_{NS}}{R_{NS}}, \tag{2.1}$$

R_{NS} is the radius and of the neutron star and G is the universal gravitational constant. The force exerted by radiation pressure in a gas with opacity κ, assuming spherical geometry, is given by:

$$F_{rad} = \frac{\kappa L}{4\pi c r^2}, \tag{2.2}$$

where L is the luminosity of the system. In the CENS system, the vast majority of radiation pressure is caused by Thomson scattering from free electrons, as the material is mainly ionised hydrogen. For accreted material consisting of a significant fraction of heavier elements, factors such as absorption must be included. In the outer layers of the RSG star, the fraction of higher mass material will be small however, as the neutron star travels further through the envelope of the companion, helium will make up a significant fraction of material being accreted. At the densities and temperatures that this occurs however, it is also likely to also be fully ionised, and so Thomson scattering remains a good approximation.

When the force provided by radiation and the gravitational force are equal, the Eddington limit is reached. We can rearange Equ. 2.1 and Equ. 2.2 to give:

$$L_{edd} = \frac{4\pi GM}{\kappa} \tag{2.3}$$

A luminosity above L_{edd} will result in material being ejected from the star. If the luminosity of the object is due to accretion, as it is in the CENS system, then the luminosity can be expressed as:

$$L_{acc} = \epsilon \dot{M} c^2 \tag{2.4}$$

where ϵ is that fraction of the rest mass energy which can be converted to radiation and $\dot{M}$ is the accretion rate. Combining Equ. 2.3 and 2.4, the maximum accretion rate is therefore given by:

$$\dot{M}_{edd} = \frac{4\pi GM}{\epsilon \kappa} \tag{2.5}$$

The exact value of ϵ is therefore key in determining the maximum accretion rate and depends on the viscosity and angular momentum in the accreting material - and the efficiency with which the released gravitational potential energy can be converted to radiation.

2.3.3 Hyper Accretion

Chevalier [30] sets out the theoretical basis for investigation of the conditions during a common envelope epoch. According to C Fryer (personal communication, June 2016), the solutions to the equation derived by Chevalier differ only by a few percent from full hydrodynamic simulations of the common envelope system. As such it can be assumed that this presents a good estimate of the actual conditions during burning. This is especially true when other sources of error are taken into account. For example the mass of the neutron star, for which a small change in input parameters may vary conditions significantly, due to the strong dependency of the temperature and density of the in-falling material on the mass of the compact object. A full investigation of the effect of neutron star mass on the products of burning in the system has not been undertaken due to time constraints, however this would be a useful investigation to undertake.

The Eddington limit may be exceeded when neutrinos are responsible for the luminosity of the system. In this scenario, matter can fall onto the surface of the neutron star unimpeded as the neutrinos will only interact with extremely dense material. As the mater falls through the gravitational well of the system, some of the energy is converted to heat as photons are trapped in the inward flow. Accretion proceeds at the Bondi-Hoyle accretion rate [30].

There are many factors which may affect the rate of accretion onto the surface of the neutron star. These include:

1. Density of the accreted material
2. Density gradient in the companion star envelope
3. Position of the neutron star in the envelope
4. Angular momentum in the system (both of the NS around the center of mass and of the NS itself)

And others beyond the scope of this thesis. Addressing each of these in turn:

Density of Accreted Material

The density of the medium increases towards the center of the companion, and the accretion reaches a maximum at the interface of the NS and the He core. Chevalier [30] provides the theory to describe this accretion and shows that for the case of two companion stars of different radii, one a RSG of radius $R \approx 4 \times 10^{11}$ km and the second of radius $R \approx 4 \times 10^{12}$ km the accretion rate increases by a factor of $\approx$ 25 between the larger and smaller RSG. The less extended, denser envelope is the one which accretes at a higher rate. Due to the fact that accretion varies so strongly with density, and it was desired to follow a significant proportion of the in-spiral of the NS, a range of accretion rates from $10^{-2} - 10^{5} M_{\odot}/yr$ was selected to model. This covers all expected accretion rates, from the first interaction of the NS with the giant envelope, to contact with the core. Whether the system would remain stable on this time-scale is unclear.

Density gradient in the companion star envelope

MacLeod and Ramirez-Ruiz [4] discuss the effect of a density gradient in the envelope of the companion star. They argue that a density gradient across the accretion radius of the neutron star results in significant angular momentum which inhibits accretion. Figure 2.4 (reproduced from Addapted from [4])shows this effect. It is important to note that in this diagram, the density gradient is not that between the orange neutron star envelope and the envelope of the companion, but from the top (or outer edge) of the companion envelope and bottom (or inner edge - towards the core). It is therefore clear that a small density gradient results in significant turbulence. This model is flawed however for two reasons, firstly, as has been mentioned in previous sections, the radius at which the effects of angular momentum become important are small compared to the accretion radius of the NS [5] and secondly, this paper does not address the effect of neutrino cooling on the accretion rate and so must necessarily underestimate it. 'y' and 'v' in the diagram are in units of accretion radius and are distances from the central compact object. The highly turbulent nature of the panels where $\epsilon_p = 0.55$ and $\epsilon_p = 1.75$ correspond to the accretion conditions with the highest density gradient. From these images it can be seen that material from close to the neutron star can be ejected into the companion star's envelope, providing a mechanism by which the companion star might be enriched.

Angular Momentum

Reduction of the flow of material on the neutron star due to the effects of conservation of angular momentum is not necessarily to be expected, as the radius at which this becomes important is smaller than the accretion radius [30]. This implies that the model is again a reasonable approximation to the environment, even without the inclusion of angular momentum considerations.

2.3.4 Neutrino Losses

Due to the very high temperatures and large neutrino fluxes in the CENS system, it was decided to investigate the effects of neutrino losses on the temperature in the model due to deleptonisation. In order

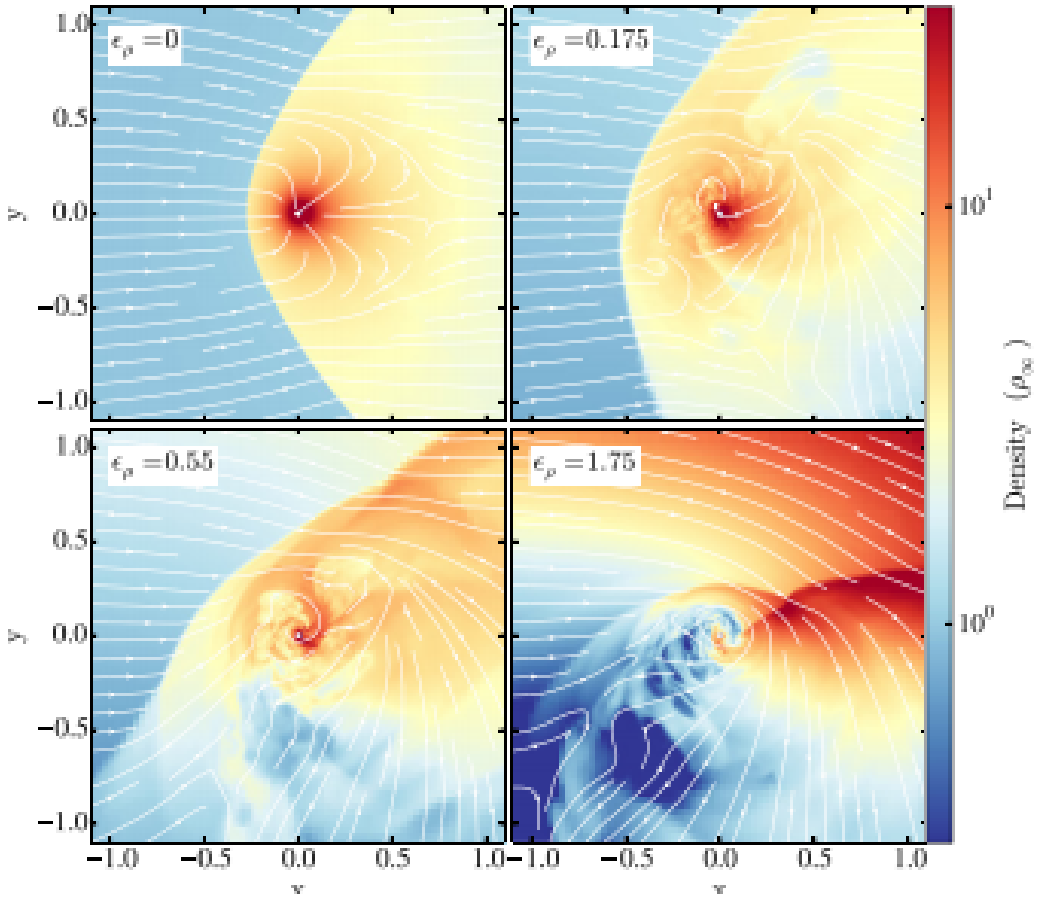

Figure 2.4: Image showing the effect of a density gradient across the accretion radius of the neutron star, ϵ_p. It can be seen that introducing a significant density gradient introduces large turbulent effects which MacLeod and Ramirez-Ruiz [4] argue significantly reduces the accretion rate in the CENS system. This is at odds with the work of Chevalier [5], and does not account for the effect of neutrino cooling. 'y' and 'v' are in units of accretion radius, and are distances from the central neutron star as it passes through the companion envelope. Reproduced from [4].

to achieve this, analytic expression dedveloped by Fryer, Benz and Herant [31] was used. This gives the change in energy due to deleptonisation in the system as:

$$\partial E_{nuc} = 2 \times 10^{18} T^6_{MeV} \partial t \tag{2.6}$$

Where T^6_{MeV} is the temperature in units of MeV. It was found for the parameters of the simulations run that the change in temperature was negligible. Although the temperature is high in the system, the burning time is very short and material is ejected too quickly for the effects of deleptonisation to be felt.

2.4 Gravitational Waves

An interesting consequence of the mechanics of the common envelope system is concerned with the Laser Interferometer Gravitational-wave Observatory (LIGO) experiment to detect gravitational waves. Whilst some neutron-star neutron-star binaries may form without the need for a common envelope system (see for instance Ref. [32]) for binaries which form without super nova kicks - where the super nova explosion imparts significant velocity to the remnant object - it is understood that, for neutron star systems to coalesce in less time than the age of the universe, the progenitors of these compact objects must have, at some stage of their evolution, undergone a common envelope phase (see, for instance, Ref. [4]).

LIGO detects the compression and expansion of space-time as a gravitational wave propagates through the experiment. These waves are caused by a number of phenomena, amongst which are compact object binaries. Figure 2.5 shows an artist's impression. Larger distortions are generated by more massive, more compact, or faster rotating objects. Due to the relatively small mass of NS-NS mergers, the waves produced are fairly small in amplitude and so difficult to detect. As the sensitivity of LIGO increases however, the frequency at which NS pairs orbit will be perfectly suited to be detected by the experiment [33]

Two reviews of the data colected by the LIGO experiment in it's fith and sixth runs [6] [34], searching for compact object binary mergers with total mass $2M_{\odot} < M_{tot.} < 25M_{\odot}$, showed that no coalescing neutron star binaries had been observed, placing upper limits of the frequency of this phenomenon in the galaxy at $1.4 \times 10^{-2}\mathrm{yr}^{-1}\mathrm{L}_{10}^{-1}$ (L_{10} is defined as 10^{10} times the blue solar luminosity - for more details on this see Ref. [6]).

The limits of these events can be seen in Figure 2.6. It remains unclear whether the lack of observational evidence for NS-NS mergers is due to a lack of progenitors for these systems, or if the currently predicted rates of NS-NS mergers will be observable with the upgrade of LIGO to advanced-LIGO. With the current efforts to upgrade LIGO, it is expected that the number of compact binary mergers observed will be in the region of $10^2 - 10^3$ per year, providing a wealth of information and allowing constraints to be placed on the conditions of massive binaries and binary compact object systems.

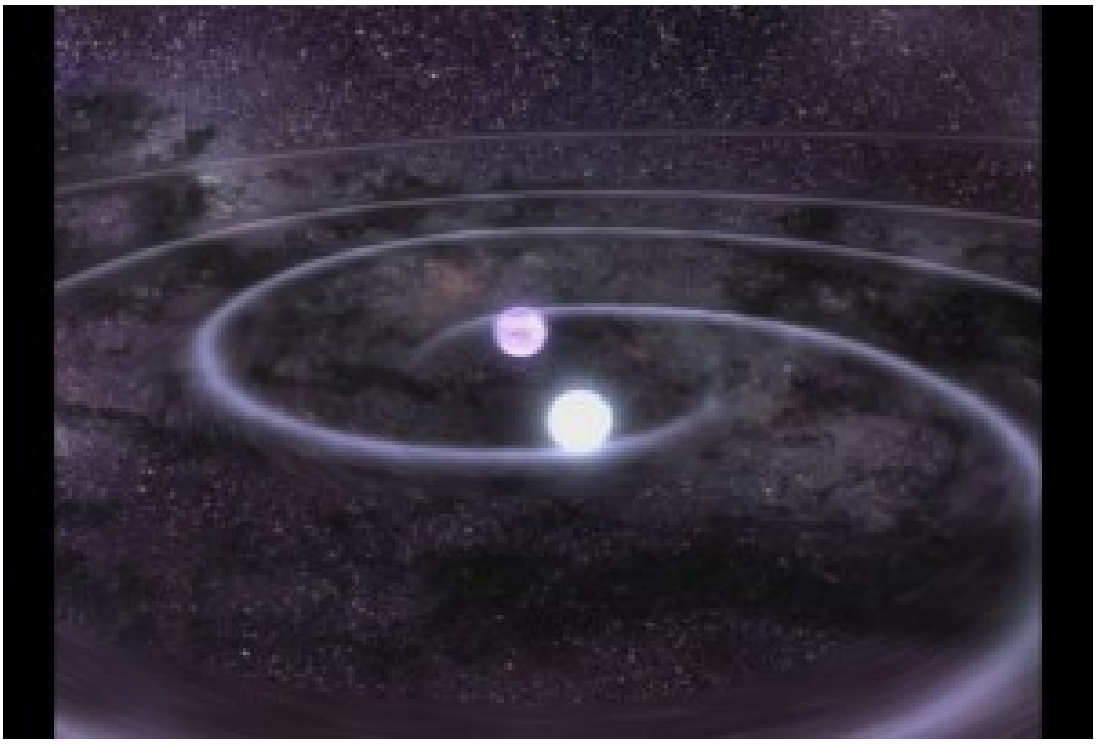

Figure 2.5: Artist's impression of a NS-NS merger, showing the gravitational waves propagating from the orbiting massive objects. Credit: NASA/Goddard Space Flight Center

System	BNS	NSBH	BBH
Component masses ($M_\odot$)	1.35/1.35	1.35/5.0	5.0/5.0
D_{horizon} (Mpc)	40	80	90
Nonspinning upper limit ($\text{Mpc}^{-3}\,\text{yr}^{-1}$)	1.3×10^{-4}	3.1×10^{-5}	6.4×10^{-6}
Spinning upper limit ($\text{Mpc}^{-3}\,\text{yr}^{-1}$)	...	3.6×10^{-5}	7.4×10^{-6}

Figure 2.6: Limits imposed by the LIGO experiment on the frequency of NS-NS merger events. Until further upgrades are undertaken on the LIGO experiment it is not possible to say whether the lack of mergers is due to a lack of events, as the predicted rates of NS-NS mergers are of order 10^3 smaller than the current upper limit imposed by the data. Reproduced from [6]

Also part of the difficulty of observations presently is that there are a large number of unknowns. There may be a number of reasons that these systems become disrupted and are less common than expected - if during the common envelope phase of these systems, one or both of the compact objects is disrupted, or if the probability of these systems occurring is low due to other effects such as supernova kicks disrupting massive binaries.

Chapter 3

Nuclear Physics Theory

3.1 Overview

In Main sequence stars, nuclear burning processes generate energy which halts the collapse of the star under gravity. For accretion onto the surface of a neutron star, fusion occurs because of the high densities and temperatures achieved in the accretion processes, where the energy liberated from in-falling material is an order of magnitude larger than the energy generated from nuclear processes.

Observations of the object HV 2112 show an apparent over-abundance of several elements - Rb, Li and Mo as expected in a TŻO - and other enhancements (e.g Ca) which are not predicted from previous models [1] - see section 1.2 for discussion of the results of Levesque et al.

The pp-chains and CNO cycle are outlined as the major burning pathways in the companion star This section will then go on to describe the rp- and interrupted rp-processes, and the αp-process, their waiting-points and burning products. The effects of nuclear structure on the products of stellar burning will also be addressed.

3.2 Reaction Rates in the Stellar Environment

In order to discuss the products of nuclear burning in stars it is necessary to first give a brief introduction to the mechanics of nuclear processes and burning in a stellar environment.

Nuclear reactions can be represented with the general form:

$$a + X \rightarrow Y + b \tag{3.1}$$

Where a and b can be any of a number of particles, and X and Y are any of a number of nuclei. For example, reaction 3.2:

$$\gamma + {}^{13}N \rightarrow {}^{12}C + p, \tag{3.2}$$

represents the photodisintegration of ^{13}N, a process which can influence the production of ^{13}C, reducing the production of free neutrons in certain stellar environments [35]. The likelihood of reaction 3.1 occurring is given by the reaction cross section, σ, and has units of area. There may be many types of reactions for a particular nucleus, the sum of all possible reactions will give the total cross section, σ_T.

Classically the cross section for the reaction of two particles would be given by the area of the two particles and thus the likelihood of them colliding:

$$\sigma = \pi(R_1 + R_2)^2, \tag{3.3}$$

however the cross section does not depend purely on geometric considerations, as the objects which are reacting are quantum mechanical in nature. We must take into account quantum mechanical effects in order to accurately describe the reactions of particles, as well as considerations such as the Coulomb repulsion.

The Coulomb potential inhibits reactions between like-charged particles. Classically, incoming particles would require at least the energy of the Coulomb barrier to form a compound nucleus. It was quickly realised that this did not agree with observation (in this regime our sun would not be hot enough to burn). Quantum mechanical tunnelling allows nuclear reactions to take place at much lower energies, as there is still a small probability of a reaction. This probability is given by 3.4:

$$C = exp\left(\frac{-2\pi z_1 z_2 e^2}{\hbar v}\right). \tag{3.4}$$

Where C is the Coulomb penetrability. This tunnelling probability therefore depends on the charge of the two interacting particles (z_1 and z_2) and their velocity relative to each other (v). Using the Coulomb penetrability it is possible to derive an expression for the cross-section of a reaction, given in Equation 3.5:

$$\sigma\left(E\right) = \frac{1}{E} exp(-2\pi\eta) S(E) \tag{3.5}$$

Where S(E) is the astrophysical S factor, and contains all of the nuclear physics dependence of the system. The factor of $-2\pi\eta$ is the Gamow factor and describes the probability of the particles overcoming the Coulomb barrier. It is useful to split the equation in to two terms in this manner, as the Gamow factor has a strong dependence on the energy of the system, where as the S factor has a weak dependence on this energy (the value of the S factor can change significantly at resonances however, see below). This separation of the strong and weak energy dependences allows for more reliable extrapolation to energies which are at too low an energy to be successfully investigated with current experimental facilities.

3.2.1 Thermonuclear Reaction Rates

Cross-sections determined in the laboratory are obtained using a fixed target and a beam of impinging nuclei at a specific energy. In a stellar environment both reactants will be plasmas, and will therefore be in relative motion. In order to resolve this problem, the density of particles N_1 and N_2 per unit volume are taken, along with the relative velocities of the two particles, v. σ, also a function of v, is chosen to give the reaction rate at this relative velocity:

$$r = \sigma(v) v N_1 N_2 \tag{3.6}$$

There will be a Maxwell-Boltzmann distribution of the velocities in the gasses if the following conditions are met:

1. The gasses are in thermal equilibrium

2. The gasses are non relativistic

3. The gasses are non degenerate

There is a distribution of the relative velocities when these conditions are met, defined here as ϕ. As ϕ is a probability distribution of the relative velocities, $\int_0^\infty \phi(v)dv = 1$. Using this it is possible to construct an expression for the reaction rate per particle pair (equation 3.10):

$$< \sigma v >= \int_0^\infty \phi(v) v \sigma(v) dv, \tag{3.7}$$

where ϕ is given by:

$$\phi \propto exp\left(-\frac{\mu v^2}{2kT}\right) = exp\left(-\frac{E}{kT}\right), \tag{3.8}$$

And therefore construct an expression for the reaction rate in the gas:

$$R = N_1 N_2 < \sigma v > \tag{3.9}$$

Finally, as the Coulomb barrier is high compared to the average kinetic energy of the particles, only those particles in the high-energy tail of the Maxwell-Boltzmann distribution will react - even taking into account tunnelling probability the particles with average energy will not be energetic enough to undergo reactions. The tunneling probability increases exponentially with energy, however the number of particles with that energy decreases. The expression 3.10 gives the reaction rate per particle pair:

$$< \sigma v >_{12}= \left(\frac{8}{\pi \mu_{12}}\right)^{\frac{1}{2}} \frac{1}{(kT)^{3/2}} \int_0^\infty S(E) exp\left[-\frac{E}{kT} - \frac{b}{E^{1/2}}\right] dE \tag{3.10}$$

the maximum of this function then gives the Gamow peak for a specific reaction.

The above equation describes the burning processes for many conditions however there are some stellar environments that can not be described with this approach. These include, for example, the electron

capture processes that occur in degenerate systems such as neutron stars. It is therefore always important to consider the conditions for a Maxwell-Boltztmann gas and apply the appropriate formalisms when these conditions are not met.

There are many other considerations when describing thermonuclear reaction rates, for instance screening effects in the stellar plasma [36]. This is beyond the scope of this thesis however and will not be discussed further.

Fowler et al [37] present a literature review of the thermonuclear reaction rates available. These and several other similar reviews, have been used to compile a reaction network for use with the ppn codes. The rates used in the post-processing codes are sourced from a variety of libraries - JINA REACLIB, KADONIS and NACRR are commonly used examples however other reaction libraries may be used.

3.2.2 Resonant Reactions

Resonance effects are of key importance in nuclear astrophysics, for example the Hoyle state is responsible for the production of ^{12}C in He burning. Without this resonance the rate of production of ^{12}C would be far lower, and nuclear burning would be substantially different. The presence of a resonance can dominate the reaction rate for a particular interaction, as shown in Figure 3.1 [7].

Resonant reaction rates depend strongly on the specific nuclear properties of an isotope. The increase of reaction rate is independent of temperature, however the resonances occur at specific temperatures depending on the nuclei involved in the reaction. This is because the resonance occurs when the incident particle has an energy which corresponds to an excited state in the compound nucleus. Because of this the S factor no longer varies smoothly with energy.

The full width at half maximum of the resonance is related to the half-life of the excited state through equation 3.11:

$$\Gamma = \hbar/\tau \tag{3.11}$$

and the width of the resonance in part determines it's strength:

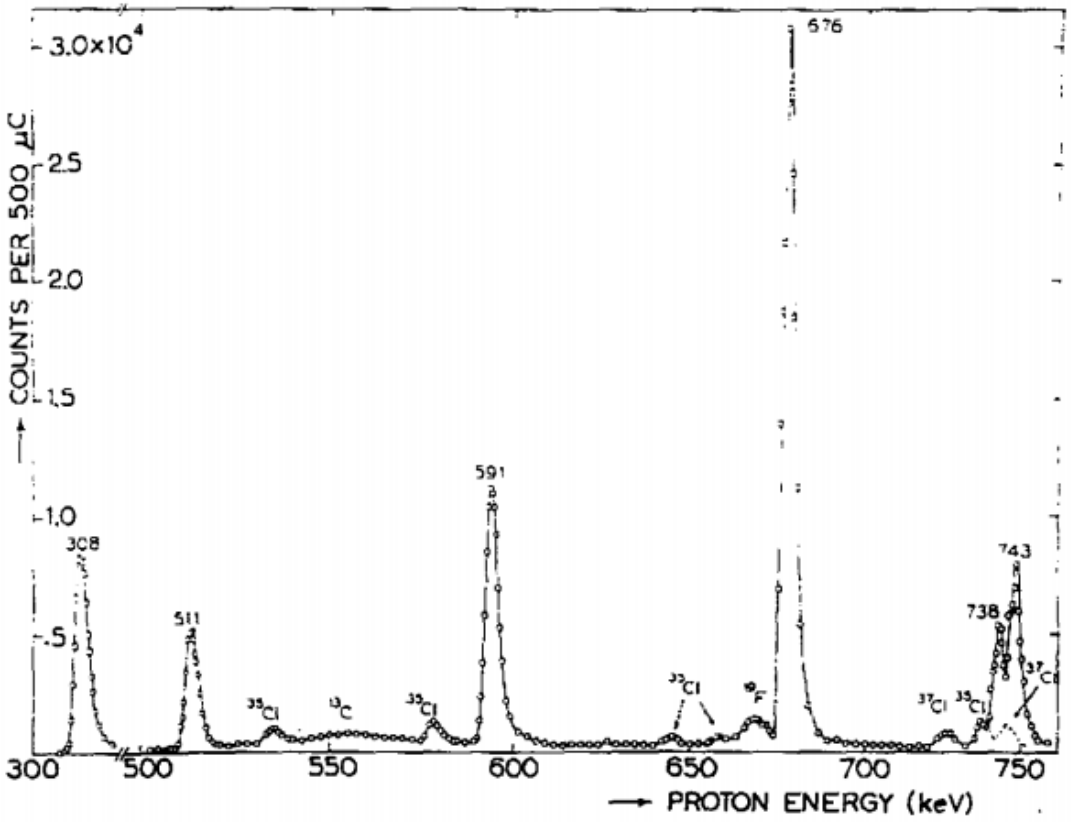

Figure 3.1: This figure shows the effects of narrow resonances on the observed counts in proton capture of ^{23}Na. It can be seen that a significant increase in the rate of reaction occurs at energies which correspond to excited states in the compound nucleus. Other peaks are evident, due to interactions with Cl atoms in the NaCl target. Reproduced from [7].

$$\omega\gamma = \frac{\omega\Gamma_a\Gamma_b}{\Gamma} \tag{3.12}$$

where Γ_a is the rate of formation of the compound nucleus and Γ_b is the rate of decay through the correct channel and ω is the spin factor, which accounts for the spin quantum numbers of the incident and compound nuclei. Combining this with work from section 3.2.1 it is possible to obtain an expression for the reaction rate of narrow resonances:

$$< \sigma\nu >= \left(\frac{2\pi}{\mu\kappa T}\right)^{3/2} \hbar^2 \left(\omega\gamma\right) exp\left(-E_R/kT\right) \tag{3.13}$$

This equation can be used to describe narrow resonances and their effects on reaction rates. There are both broad and narrow resonances however. In order to describe broad resonances the Maxwell-Boltzmann distribution of velocities in the burning material must be taken into account [38].

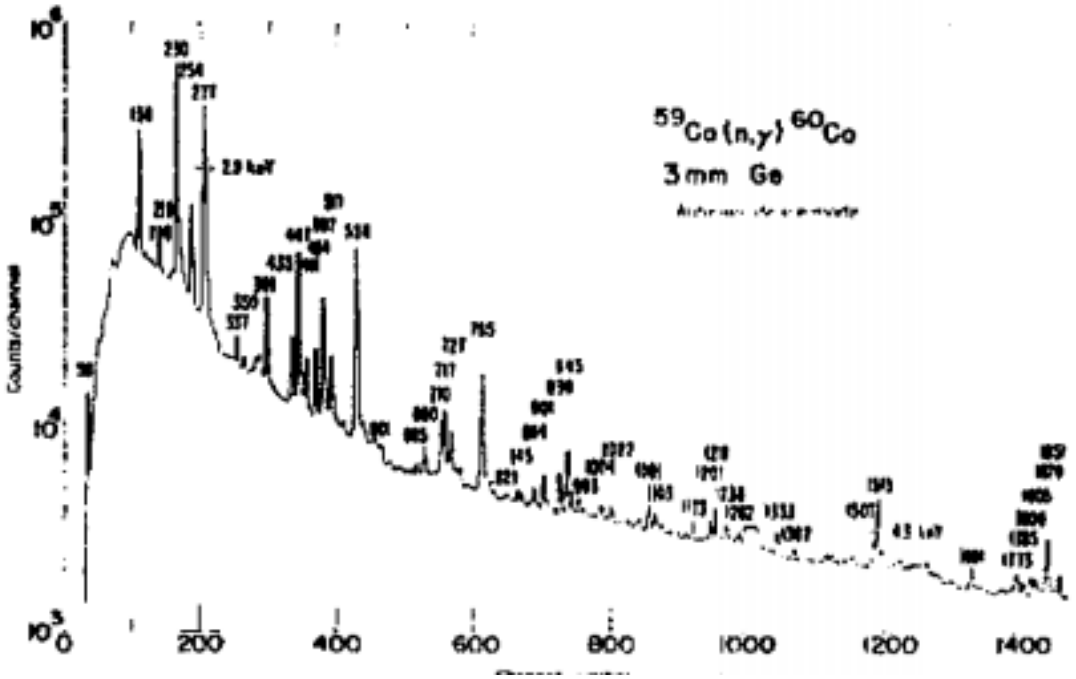

Figure 3.2: 1/v dependence of the neutron capture rate. reproduced from [7]. The general trend of decreasing reactions with increasing energy can be seen, with resonance features also present.

3.2.3 Neutron Induced Reactions

It is useful to briefly describe the nature of neutron induced reactions, as they are likely to be important in the burning processes in the CENS system. They are likely to affect the path of nucleosynthesis as a large neutrino flux is the foundation of the model investigated here and the mechanism by which material is allowed to accrete at super Eddington rates. Capture of these anti-neutrinos by protons can produce large abundances of free neutrons. These may then be captured, and so provide a mechanism for bypassing the waiting-point nuclei in the rp-process.

Neutron induced reactions have a $1/v$ dependence, the probability of a reaction decreases with increasing velocity - as the energy in the system increases (illustrated in Figure 3.2), neutron capture becomes less likely. In very high neutron fluxes however, capture reactions may still be significant. If this is the case, these reactions provide a rapid way to bypass waiting-point nuclei and extend the path of nucleosynthesis to larger masses.

3.3 Hydrostatic Burning

In this section I will discuss the main energy producing phases of a RSG star, as the nucleosynthesis occurring in these is relevant to the system as well as for burning in the accreted material. Hydrostatic burning suports a star during the majority of it's life. Enerrgy is produced by nuclear burning to stop collapse of the star, mostly from the fusing of hydrogen to helium. Once burnin passes these stages, therate of combustion of the fuel increases drastically, with Si burning taking less than 24 hours to completely exhaust it's fuel [39].

After this, a description of the main features of the rp-process is presented.

3.3.1 The pp chains

The pp chains are a series of reactions fusing hydrogen to helium. There are three pathways, as illustrated in Figure 3.3. They are the most favourable reactions burning H or He isotopes in stars.

All of the pp-chains begin with the fusing of 2 protons, followed by β^+ decay:

$$^1H + {}^1H \rightarrow {}^2H + e^+ + \nu \tag{3.14}$$

This step is dependent on the weak force, due to the β-decay of the intermediate nucleus, as well as the strong force and Coulomb barrier. This causes the reaction to have a small cross-section relative to many stellar reactions [8]. The release of neutrinoes in this reaction, and others, causes a loss of energy from the system as neutrinos are not usually trapped in the stellar environment.

The next reaction is also common to the pp-chains:

$$^2H + p \rightarrow {}^3He + \gamma \tag{3.15}$$

This reaction is more likely than the competing reaction $^2H + {}^2H \rightarrow {}^4He + \gamma$ due to the very low abundance of ^{2}H and it's short halflife compared to burning timescales. The pp1 chain then forms ^{4}He

through the reaction ^{3}He$(^3He, 2p)$ ^{4}He. The reaction is favourable as ^{3}He is stable and it's abundance is much larger in the stellar plasma as compared with deuterium.

Once the temperature and ^{4}He abundance are high enough, α-capture on ^{3}He becomes the preferred reaction, producing ^{7}Be which then β-decays. The ^{7}Li so produced then undergoes the reaction ^{7}Li(p, α) ^{4}He. At higher temperatures, proton capture on ^{7}Be may bypass the β-decay of the pp2 chain, giving rise to the pp3 chain. In the accreting material, the pp3 chain is the most likely, due to the presence of ^{4}He and the high temperature of the environment.

Illiadis [8] shows the relative action of the pp-chains at different temperatures. In the CENS system, for the majority of conditions investigated, the pp-chain is the only chain which will act 3.4

The range of temperatures at which the pp-chains contribute varies with the density of the system. Hydrogen fusion proceeds via the pp-chains in the core of H burning stars at temperatures between 8 and 55 MK, however the temperature at which fusion proceeds in the H burning layers of AGB stars is significantly higher, between 45 and 100 MK[8].

3.3.2 The CNO Cycles

The CNO cycles also convert H into He in stellar environments. Given the same conditions as for the pp-chains, if there is a significant fraction of CNO material in these reactions will be preferred.

Breakout from the CNO cycles is necessary in order to produce heavier nuclei. Although the exact breakout mechanism is not yet fully understood, it is believed that it mainly proceeds through the reaction ^{15}O$(\alpha, \gamma)^{19}$Ne reaction [8].

3.4 The rp-process

3.4.1 Introduction to the rp-Process

The rp-process is a series of rapid proton captures on radioactive or stable seed nuclei, producing proton rich nuclei, interspersed with β-decays. The seed nuclei may be present in the initial composition of

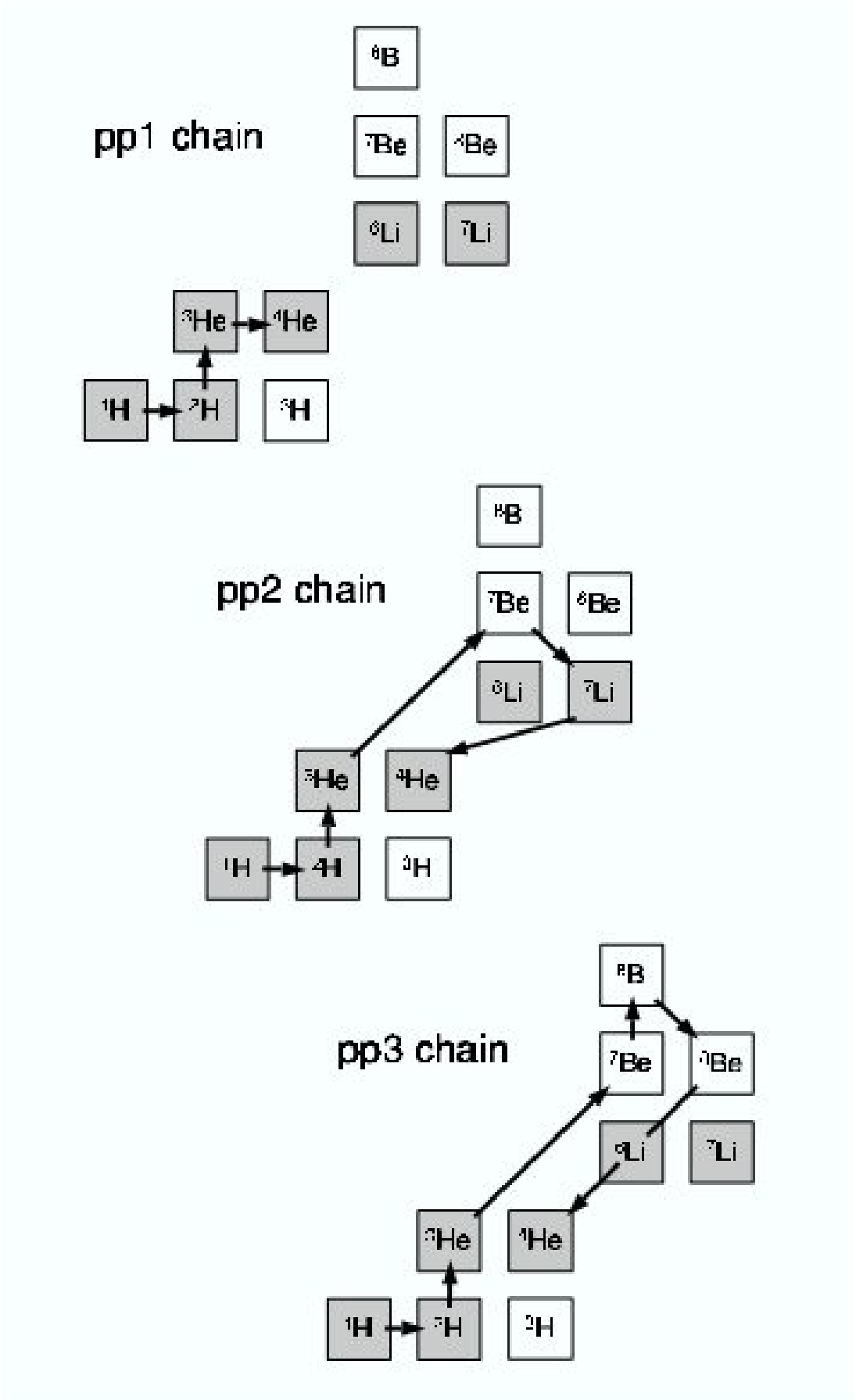

Figure 3.3: Representation of the pp-chains taken from [8].

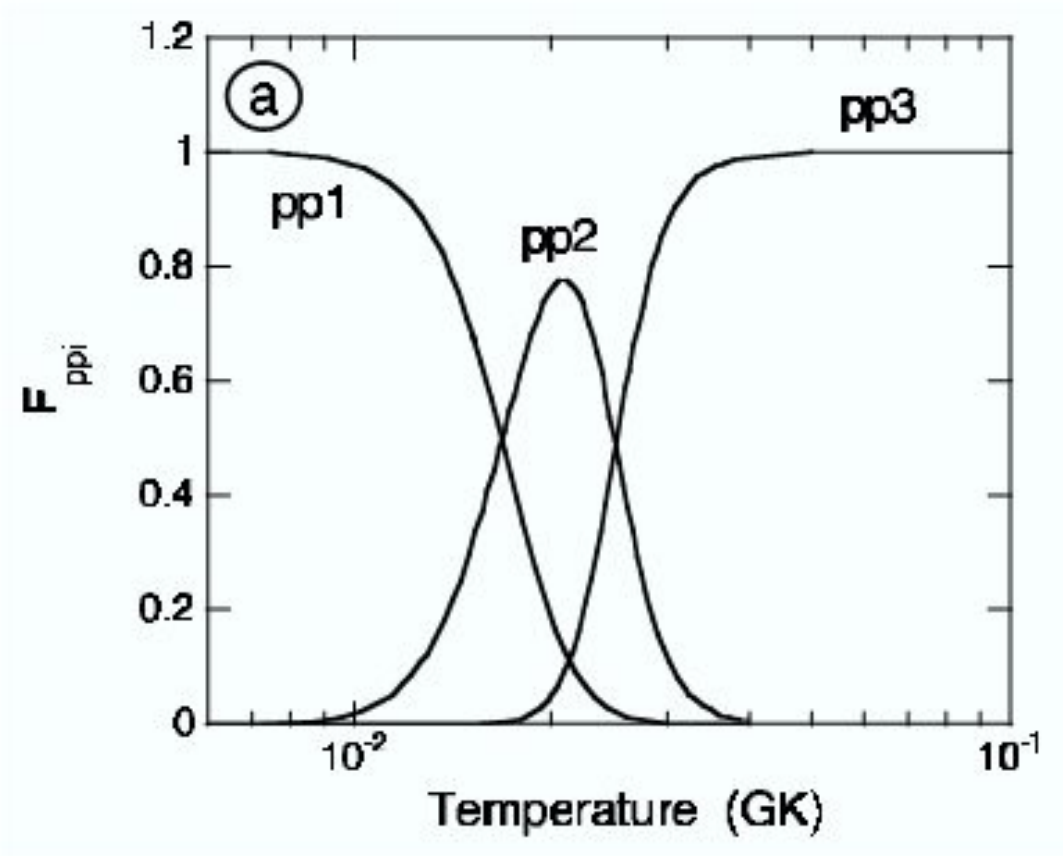

Figure 3.4: Relative contributions of the pp-chains. For the CENS system, due to the high temperatures, the pp3 chain is likley to make the largest contribution of these, however they may be out competed by CNO reactions and the 3α-process if the necessary seed nuclei are available. Taken from [8].

the gas, or in the case where a system forms with zero initial metalicity, they may be the products of α -burining in previous stages of the system's life [40].

As the path of nucleosynthesis approaches the proton dripline, further proton captures are inhibited by photodisintegration reactions due to protons being un- or lightly-bound (the isotopes have small or negative Q values). Schatz et al [41] identify a number of key parameters necessary for a successful description of the rp-process. These are:

1. Differences in nuclear masses - i.e the Q values of proton, α, and β^+ decay
2. Deformation of the nucleus
3. Reaction rates, including rates for:
    - Particle and inverse reactions

- two proton capture
- β-decays

Nuclear statistical equilibrium also can effect the burning in these environments, as temperatures can often exceed T_9 = 5 - see for example the results from this investigation in section 5. The effect of entering into full NSE is to remove dependence on initial metalicity and to homogenise results. If there is a large Y_e and a neutron rich NSE is achieved, more neutron rich isotopes are produced.

It is experimentally challenging to obtain data for these processes as the isotopes involved lie far from stability. Due to the difficulty of obtaining reaction rates and masses for nuclei close to the proton dripline, these parameters are often determined from statistical models, such as in Fisker et al [42] where the rates for a large number of nuclei are determined using a Hauser-Feshbach statistical model.

Proton capture rates in the rp-process are rapid, usually many orders of magnitude larger than the β^+ rates for the same isotopes [41]. Proton captures reach equilibrium with the reverse photodisintigration reactions as Q-values for the reactions decrease, and the forward reaction to higher mass products relies on a β-decay of the isotope, that isotope is known as a waiting-point. Examples of such waiting-points include ^{24}Si, ^{29}S and ^{41}Ti. Consequently, when the proton dripline is reached, nuclei must undergo beta decay before heavier nuclei can be synthesised. As such these nuclei, and their respective nuclear physics properties, are largely responsible for determining the path of nucleosynthesis. Schatz et al [41] state that the speed of nucleosynthesis in the rp-process is solely dependent on the lifetimes of the waiting-point isotopes, as is the final isotopic abundance. This is due to the fact that almost all of the material being processed in a rp-process site is stored in waiting-point isotopes, due to their necessarily long-lived nature.

The rp-process requires two conditions:

1. Hydrogen rich fuel
2. Temperatures exceeding T_9 = 0.1

Due to these considerations, the site of the rp-process is constrained to some of the most extreme environments in astrophysics, including the surface of accreting neutron stars and accretion disks around

black holes, neutrino driven winds and supernovae explosions (these are addresed in more detail in section 3.5. It is these requirements that make the CENS system a prime candidate for the site of the rp-process, as an abundance of H-rich material is accreted in a strong gravitational field, resulting in the efficient release of energy and subsequent heating of the material to very high temperatures.

Reaction rates for nuclei near the proton drip line may not be well constrained due to limited experimental data, and statistical models used to determine resonant rates may be inaccurate due to the low level densities of nuclei in this region [40]. At small low densities, contributions from individual resonances can dominate the rate and so statistical models of these rates are no longer valid. Because of this, van Wormer et al [43] estimate relevant resonant reactions from known nuclear physics data, obtained from reaction studies. This data includes spin states of the ground state, parities and other observables of the nucleus under investigation. Dependence of nucleosynthesis on these inputs will be discussed further in section 3.4.2.

3.4.2 Nuclear Physics Parameters

The products of the rp-process are determined, largely, by the masses and β decay rates of nuclei along the proton drip line [41]. In this section, the dependence of nucleosynthesis on these parameters will be discussed in detail.

The Effect of Nuclear Mass and Deformation on the rp-process

The masses of nuclei in the rp-process have an effect on many features of nucleosynthesis. They determine proton Q-vlaues, the proton drip line, the rates of β-decays and the rates for many other types of reaction [41].

Schatz et al identify the mass of nuclei in the rp-process being important for two reasons: [44]:

1. Clusters of nuclei in equilibrium form. Their relative abundances are determined by the proton separation energies, and so the mass differences between different isotopes.

2. As input for calculating the resonances and resonance strengths for reactions. These are difficult to determine experimentally and so accurate mass measurements for the relevant isotopes are critical for determining the correct nuclear properties.

With so much of the nucleosynthesis in the rp-process being dependent on the accurate masses of the nuclei along the proton drip line, the choice of mass model can have a significant effect on the rates of reactions and therefore the nucleosynthesis in the system.

Nuclear deformation is as important as many of the nuclei in the path of nucleosynthesis for the rp-process have deformed ground states. This changes the energy levels of the nuclei. In order for the masses calculated allong the proton dripline to be accurate, it is neccesary to account for this deformation in mass models [41]. Fisker et al [42] provide reaction rates for proton rich nuclei in the mass range A = 44-63. This and other such investigations provide key information for the accurate modelling of the rp-process and is achieved by applying the shell model. The largest errors in these rates are caused by predicted energy levels in the compound nuclei, corresponding to the resonant rates of the system. Because of this the experimental values of these states are hugely important or constraining the rates for these nuclei.

3.4.3 Reactions in the rp-process

This section addresses the reactions pertinent to the rp-process: proton capture, beta decays and two-proton captures. Photodisintegration reactions are also important and are caused by the action of high-energy photons on the lightly bound nulcei of the rp-process. These will be addressed here.

Proton Captures

It will be no surprise that proton capture processes are important in the rp-process. Proton captures in the rp-process are orders of magnitude faster than β decays, and so until a waiting-point nucleus is reached, the flow of material to higher masses is rapid. Material then builds up at the waiting point nucleus as β decays are necessary to pass the proton unbound nuclei past the proton dripline.

Proton capture reaction rates are clearly of importance in investigating the rp-process, and great experimental effort is expended in order to improve our understanding of these. (see, for example,[45]).

Calculations of the proton dripline [46] are necessary to fully understand the extent of nucleosynthesis however these nuclei are difficult to produce and study, and so much of the necessary data along the drip line nuclei is currently not available.

β-decays

A β^+ decay converts a proton to a neutron through the emission of a positron. These reactions are central in the rp-process as they move nuclei away from the unbound proton drip line and alow further proton captures to take place. β-decay rates for the elements Z $\leq$ 34 are available for ground states. In stellar conditions the decays from excited states are also required [41]. β decay rates become ever more important as the mass of the nucleus increases. Beyond A = 64 there is very little experimental data and therefore these must be calculated. β decays determine the time to pass waiting-points if other methods such as neutron capture or 2p reactions are not favourable.

β-decay rates in stellar environments can become weak functions of temperature, not just dependent on the weak force, if excited levels in the nucleus are thermally populated at elevated temperatures due to new reaction pathways being available to the excited nuclei. This however is not a concern in this investigation as the NuGrid codes do not include reaction rates for isomeric states at present. The rates may also become a function of density at high enough densities, due to electron capture from degenerate matter [41].

3.4.4 Waiting Points

For those nuclei which have small or negative Q values the reaction flow of the rp-process is inhibited. These are the waiting points of the rp-process. β-decays can move reactions forward, as the conversion of a proton to a neutron increases the Q value for proton capture in the new element. However β decays are slow compared to the (p, γ) reactions of the rp-process.

Waiting points in the rp-process occur at even-Z nuclei. This is because odd-Z nuclei will have a lower separation energy for the final proton in the shell. This also means that the Q value for proton captures is low, and so photodisintegration of the compound nucleus is easy. In the high temperature conditions necessary for the rp-process, these protons will be easily unbound from the nucleus. 2p captures may bridge gaps where protons are weakly bound. However, at temperatures over T_9 = 1, the Z and Z+2 nuclei are in equilibrium due to photodisintegration reactions.

The lifetimes of waiting-point nuclei depend only on the following factors: temperature and density of the material, the nuclear mass of the specific isotope, and the β-decay rates for that isotope. These parameters are therefore extremely important in determining the outcome of nuclear burning in any rp-process environment and a great deal of experimental effort has been directed towards determining them (for example [47] determining β-deccay rates, or [48] for mass measurements)

3.4.5 Endpoint of the rp-Process

The endpoint of the rp-process has been investigated on a number of occasions. Schatz et al [9] find that the rp process on an accreting neutron star terminates at a closed SnSbTe cycle (see Figure 3.5 below) due to the isotopes ^{106,107,108,109}Te being alpha-unbound. It is noted that a "pulsed" burst - in which unstable isotopes are allowed to decay to stable products - would allow matter to be processed to higher Z, as β-decays to stable nuclei would then be followed by an increase in temperature and further proton captures. In the case of the CENS system, this would correspond to material being carried to large radii and then convected back close to the surface of the neutron star. This is not predicted to occur for the majority of material, as any matter with a high enough velocity to begin escaping from the NS surface is unlikely to fall back into the system.

Koike et al [49] also investigated accretion onto a neutron star. The accretion rates in this scenario were low, ranging from $10^{-7} - 10^{-9}$ solar masses per year. They found that material up to A $\approx$ 100 was produced in the main burning regime, with ^{126}Xe being produced in the XRB flash. The increased range of the rp-process is attributed to the larger network used by Koike et al [49]. The Koike et al reaction

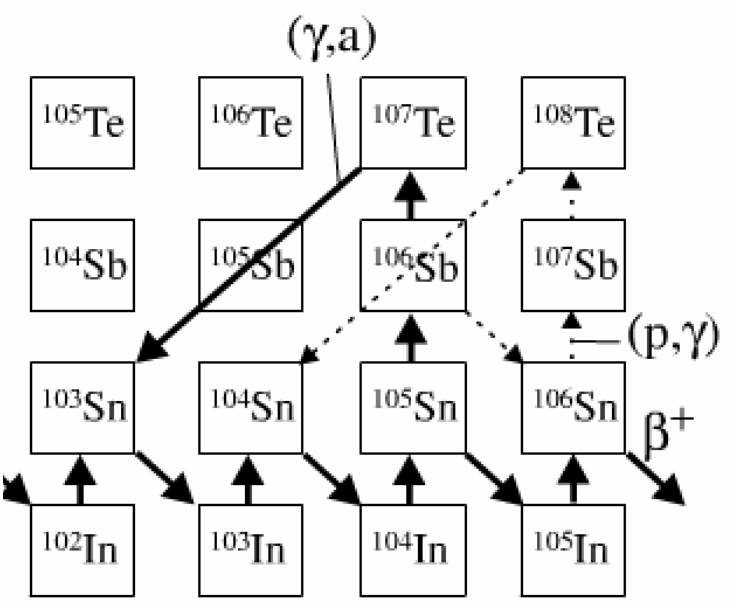

Figure 3.5: This shows the SnSbTe cycles which act during an XRB taken from [9]. This cycle is found to be similar for steady state burning in rapidly accreting neutron stars, and as such serves as a guide to the expected products in the CENS system.

network extends to Bi, where Schatz et al extend only as far as In [41]. Although Schatz et al also produce material in the A $\approx$ 100 region, this is achieved by allowing material to decay in pulses of burning. There may be some similarities between the 'pulsed' burning of Schatz et al and the 'flashes' of Koike et al however. The system investigated in this thesis differs from both of these in that there is no period in which the material can decay, which makes the presence of heavier material particularly interesting.

van Wormer et al [43] investigate the reaction pathways at temperatures between 1.5×10^8 and 2×10^9 K, which covers the majority of the range of temperatures in the present investigation. Firstly at these extreme conditions, the break out and merging of individual cycles is observed. Then, (α, p) reactions are found to contribute at higher temperatures.

3.5 Astrophysical Sites of the rp-Process

The particular burning conditions necessary for the rp-process to occur required highly energetic sites. A brief introduction to the sites theorised to be responsible for production of rp-process material will be presented here, and the relative merits of each discussed.

3.5.1 Classical Novae

Classical novae occur in binary systems where a white dwarf star is accreting material from a companion. The companion star fills it's Roche lobe (see Figure 3.6) and material overflows to fall onto the surface of the white dwarf. This releases energy as outlined in section 2.3 however it is much less efficient, as the WD has a much larger radius than a NS (of order 1000x larger) and hence the energy liberated through accretion is much lower. Most heating on the white dwarf is therefore caused by energy release from nuclear reactions.

The material is degenerate due to the high pressures on the surface of the WD and so the temperature increases with no commensurate expansion of the material [50]. The mass accretion rate is generally low [3] and so the increase in temperature is gradual, contributed to by increasing reaction rates in the degenerate material. The temperature increases gradually as nuclear reactions continue, untill temperatures increase above a threshold and thermonuclear runaway occurs. Degeneracy is then lifted, and the material expands and is ejected from the surface of the WD. Peak temperatures in novae outbursts are typically around 3×10^8K [51]. Novae are expected to re-occur, if the thermonuclear runaway is not so energetic that it disrupts the compact object. Due to the low accretion rates, the time for a recurring novae is too long for any to have been observed - of the order of 10,000 years [3].

From the work of José and Hernanz [51] the typical extent of nucleosynthesis in novae seems to be limited to around A $\approx$ 40. The abundances of some elements which are overproduced by the action of novae in these simulations can be explained solely by the action of novae. However, due to the relatively small extent of nucleosynthesis this environment is not suitable for explaining the origins of some of the heavier products of the rp-process. The advantage of the nova description of the production of the rp-process nuclei is that the material is easy to eject from the surface of the object, and most or all of the processed material will - this is not the case for all of the following scenarios.

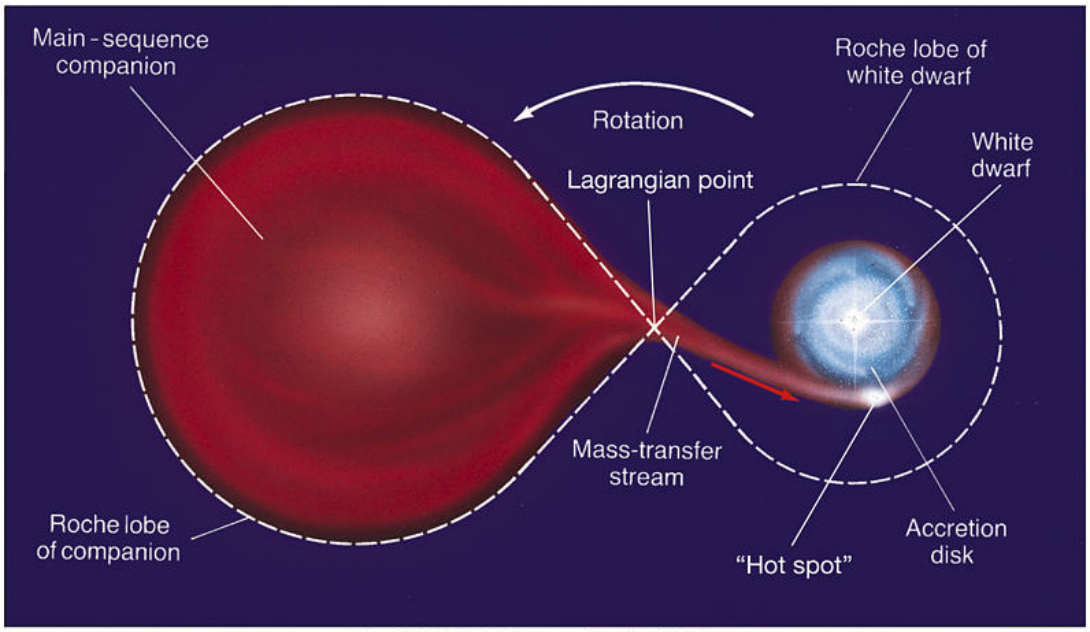

Figure 3.6: Representation of the accretion of material onto the surface of a white dwarf, as in a classical novae. The same mechanism is responsible for type I XRBs, with the white dwarf being replaced with a neutron star.

3.5.2 X-Ray Bursts

During a type-I XRB, matter is accreted onto the surface of a neutron star in a binary system, in much the same manner as with a classical nova (see Figure 3.6). 20-100 MeV per nucleon is released as the accreted material falls through the gravitational potential of the neutron star, depending on the mass of the compact object. This energy heats the surface of the neutron star, which is unable to expand as it is supported by degeneracy. As the temperature continues to increase, nuclear reactions on the surface of the neutron star proceed at faster rates until a thermonuclear runaway occurs. Enough energy is produced that degeneracy is lifted and the surface of the neutron star expands. During this expansion, rapid proton and α particle capture reactions occur, driving nuclei away from the line of stability and towards proton rich isotopes. The temperature during an XRB is of the order of T_9 = 1-2. Because of the high temperature, the reaction pathway may be hindered by photodisintegration reactions, reducing the flow of material to the heavier elements. Material up to A = 105 is however produced in these conditions [52].

The material synthesised on the surface of the neutron star is tightly gravitationally bound, and even with the high temperatures produced during the thermonuclear runaway, no material is predicted to have

the required energy to escape the surface of the star. As a potential site for the rp-process the X-ray burst therefore has significant problems explaining the abundances of rp-process material.

3.5.3 Black Hole Accretion Disks

Optically thick accretion disks around black holes provide the extreme temperature and hydrogen rich fuel needed to support the rp-process. Chakrabarti, Jin and Arnett [10] describe the processes governing energy generation in the accretion disk, and find that smaller mass black holes, and disks with low viscosity, allow the temperature to increase sufficiently to allow the rp-process to occur through α capture on ^{15}O (the rate becomes sufficient to compete with the CNO cycle burning of hydrogen at around T_9 = 0.5). Subsequent proton captures on ^{19}Ne allow the production of more massive nuclei. The 3α process also contributes to the burning processes in the accretion disk above T_9 = 0.1 and so produce more of the seed nuclei necessary to facilitate further burning to higher mass nuclei.

The extent of nucleosynthesis in this scenario may be very large, considering the prescence of α-capture processes [53]. Unfortunately the reaction network employed in these investigations is not extensive and it is unclear if the endpoint of the rp-process is determined.

The difficulty of this scenario lies in the condition that the viscosity in the accretion disk must be low in order to allow burning to occur [53]. Constraints on the viscosity of the accreting material need to be significantly improved before the possibility of nucleosynthesis in these systems can be properly assessed, as the viscosity of the accretion disk determines the efficiency with which gravitational potential energy can be converted into thermal energy. Release of material from these accretion disks would be from jets.

It is interesting to note that the combination of observation, simulation and experimental work for the accretion disk scenario affords the possibility of constraining a number of parameters, such as the viscosity of the accretion disk, due to the sensitivity of nucleosynthesis to these parameters, much as with galactic chemical evolution models.

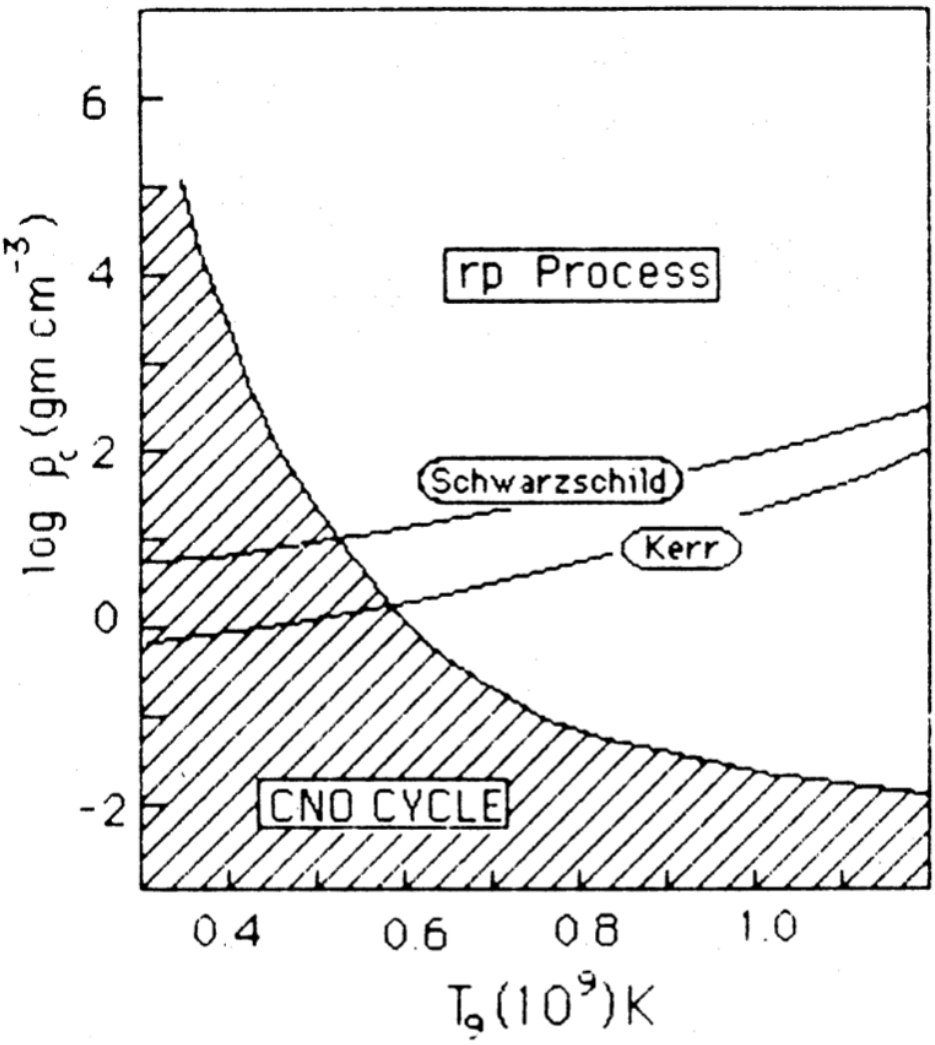

Figure 3.7: Graph showing the conditions necessary for pp-chain and rp-process burning in a thick disk around an accreting black hole. Schwarzchild and Kerr refer to the geometry addopted in the treatment of the system, and show that in both at high temperatures the rp-process is the most likely burning process. Taken from [10].

3.5.4 Neutrino-Driven Winds

rp-process nucleosynthesis during core collapse supernovae is possible thanks to the abundance of hydrogen and high temperatures in these environments. The time-scale of core collapse does not allow for the production of heavier material, due to the long β-decay half-lives of the waiting-point nuclei and the short durations of the explosions [54] [55]. A possible solution to this problem, as sugested by Fröhlich et al [56] is the production of free neutrons in the supernovae through neutrino interactions:

$$p(\bar{\nu_e}, e^+)n \tag{3.16}$$

And the subsequent capture of these by waiting-point nuclei, known as the νp-process. As most of the material in these high-energy environments will be stored as waiting-point nuclei at any one time [41] it is perhaps reasonable to assume that these interactions will be fairly common.

In nucleosynthesis studies, these environments have been shown to be able to produce p-nuclei in the mass range of A $\approx$130 [54] with some success in describing the origin of ^{92,94}Mo and ^{96,98}Ru and in others production of material up to A $\approx$ 170 has been achieved [57]. This has required the (possibly unphysical) artificial increase of entropy in the simulation, although some suggestions for the origin of this are given. In addition to this, much of the material so produced will be ejected and so this remains a strong candidate for the production of some of the p-nuclei. Figure 3.8 shows the large increase in abundance of a number of isotopes, and the waiting-points ^{64}Ge, ^{68}Se, ^{72}Kr and ^{76}Sr being bypassed by neutron captures, increasing the flow of material to higher masses.

This mechanism whereby waiting-points are bypassed may be of great importance in the CENS system. The neutrino flux will be high due to the method of cooling which allows the hyper accretion rates seen in the system, hydrogen and helium rich fuel is abundant, the density in the accreted material is high and the temperatures are also high, so resulting in rapid proton, neutron and α captures. There is some difficulty in modelling this, however, as currently the NuGrid codes do not accurately account for neutrino interactions, and weak reaction rates are not well accounted for for some of the necessary reaction within the NuGrid framework. This is a possible avenue for investigation in further projects, however, and may yield interesting results.

3.5.5 TŻ0's

A number of formation scenarios for TŻO's have been suggested. They may be formed through the merger of stars in close binary systems, supernovae kicks causing less closely bound systems to merge, or collisions of single stars in very dense globular systems [58] [59]. A difficulty comes in identifying these stars in observational data, as they are expected to have very similar properties to normal red supergiants, as mentioned above.

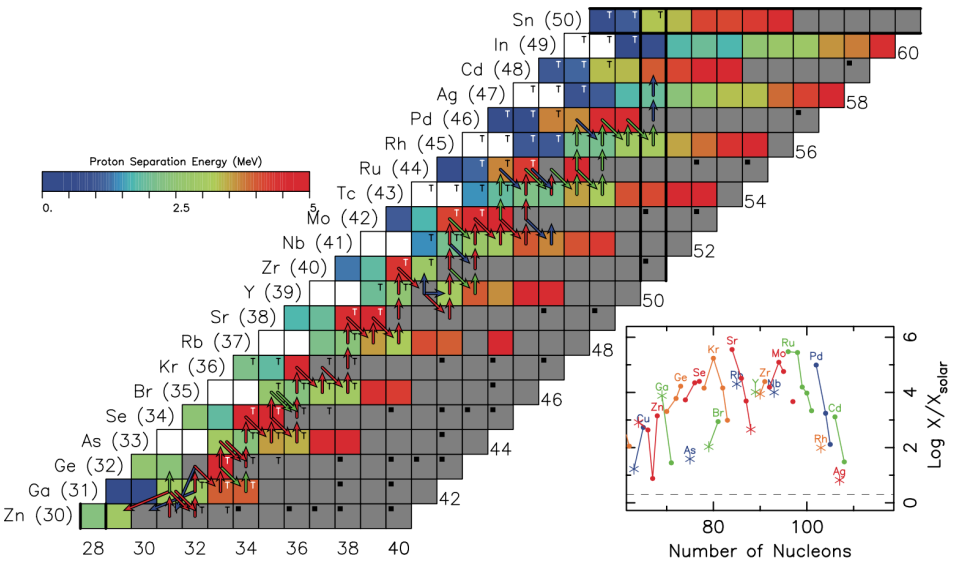

Figure 3.8: Figure showing the nuclear reaction flows for Z > 30 in neutrino driven winds. Arrows are colour coded to show the strength of flow, with the strongest in read and weakest in blue. Strong flows bypassing traditional waiting-point nuclei can be seen - for example ^{74}Se is completely avoided, as is ^{78}Kr. This behaviour may will be reproducible in the CENS environment, as neutrino cooling is responsible for the high accretion rates in the system. Reproduced from 3.8.

The nucleosynthesis in these objects has been investigated extensively as the potential site of the rp-process. It is an attractive option due to the potential high temperatures and hydrogen rich fuel. van Wormer et al [43] and Schatz et al [9] both conclude that α unbound nuclei halt the path of nucleosynthesis at A $\approx$ 70 and propose a "pulsed" burning in order to explain higher mass isotopes or the action of α captures. Due to the instabilities of the TŻO scenario, however, it is unclear whether or not this system would remain stable for long enough to produce the necessary ejecta. Accretion of a significant mass of material would disrupt the neutron star, causing collapse to a black hole, on timesales as short as 100 years [16].

Chapter 4

The Post Processing Codes

4.1 Introduction: The NuGrid Project

The NuGrid collaboration is an international reseach platform which aims to produce a comprehensive set of yields for a wide variety of stellar environments [11]. These include yields from explosive and steady state nucleosynthesis, for low-mass and massive stars, at a wide range of metalicities - although the tools developed by the collaboration are also applicable in a variety of other areas, such as sensitivity studies of reaction rates [60]. Through these investigations, and from comparisons with observations, more stringent constraints can be placed on reaction rates or factors affecting galactic chemical evolution.

Figure 4.1 shows the extent of the network used in the post processing codes. For each run, the adaptive network determines which nuclei will be required and selects these for processing, thereby reducing the time needed to run the simulation, sometimes significantly depending on the environment. There are over 5000 isotopes and 50,000 reactions included in the full reaction network. Selection of relevant reactions is done based on the conditions - the temperature and density - of the environment, as well as the minimum β -decay half-life - specified in the trajectory.input and ppn physics files respectively.

The post processing networks select reaction rates from a bank of reaction rate compilations [11] for each particular run. Because of this, it is possible to select individual reaction rates for specific isotopes, a feature which is increadibly useful in investigating the effects of individual rates on the nucleosynthetic

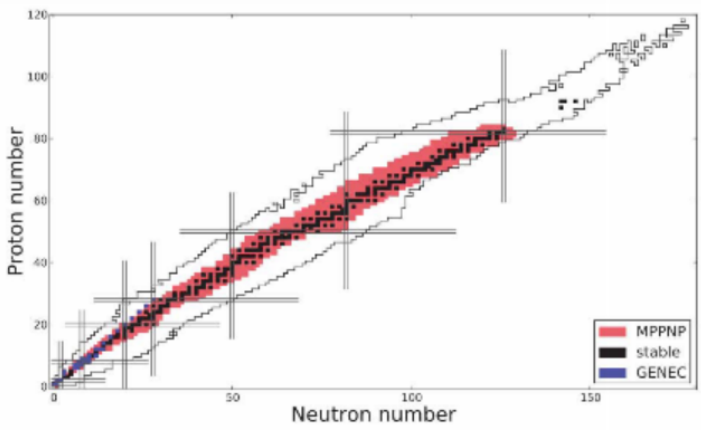

Figure 4.1: Graph showing the extent of the network used in the NuGrid post-processing codes. Blue shows the species followed in the GENEC stellar evolution codes, black are the stable isotopes. Reproduced from [11]

processes occurring in a particular environment - a investigative technique known as sensitivity studies and which has been invaluable in identifying key reaction rates in stellar environments - for example [61] [52]. The advantage over the networks used in these calculations is that the NuGrid reaction network contains an order of magnitude more processes and can therefore follow the nucleosynthesis pathways in a more flexible way and avoid possible errors by ensuring reaction networks are complete.

There are two versions of the post processing codes, ppn and mppnp, detailed in sections 4.2 and 4.3 below. The single-zone code ppn has been selected for this project however further work on this scenario would benefit from the inclusion of a multi-zone investigation. Currently a multi-zone model is not available, however see the appendices for a brief review of the work so far on developing a multi-zone simulation.

The application of the NuGrid codes is represented schematically in Figure 4.2. By taking hydrodynamics inputs and known nuclear physics parameters and applying the tools developed by the NuGrid team (outlined in [11]) conclusion can be drawn about many aspects of astronomy and physics.

4.2 ppn - The Single-Zone Post Processing Network

The single-zone post-processing network takes spherically symmetric stellar environments with no mixing between zones and simulates nucleosynthesis given the temperature and density in that zone. The

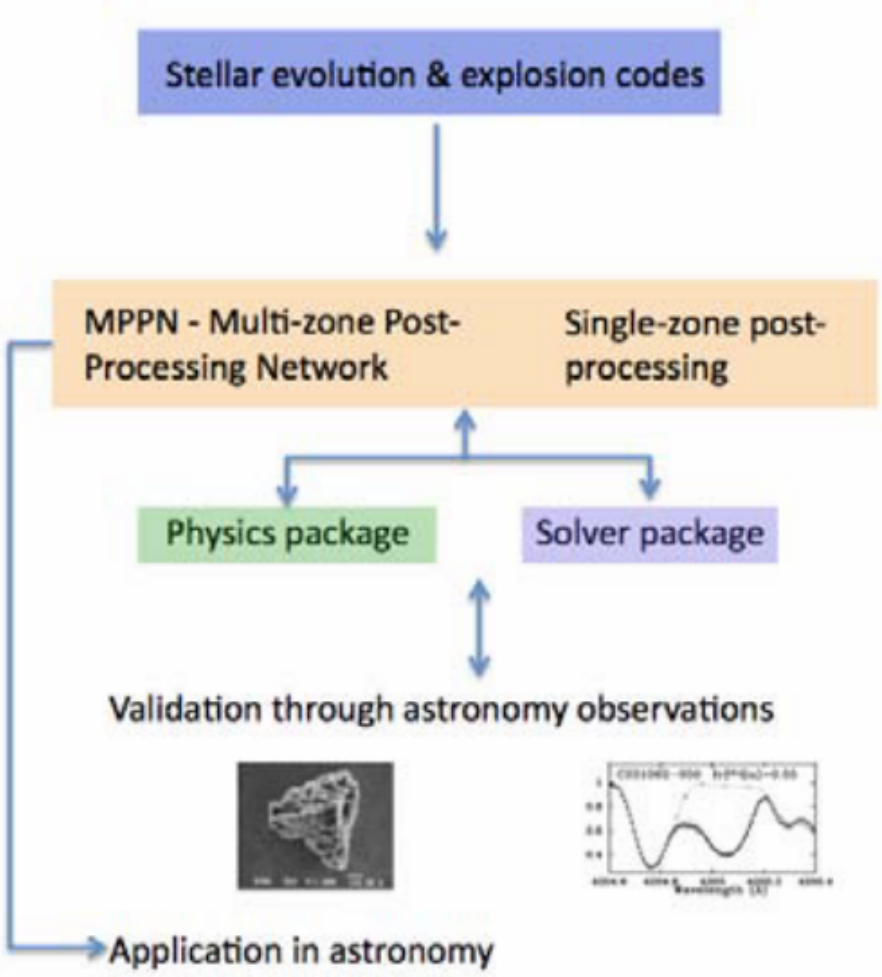

Figure 4.2: Representation of the work flow involved in simulating nucleosynthesis and it's application. reproduced from [11]

assumptions of zero mixing and spherical symmetry are good approximations to a number of different environments - for example X-ray bursts.

The primary advantage of using a post-processing network to follow nucleosynthesis in stellar environments is that the computational power required is much reduced from what would be needed to follow the same processes in a full hydrodynamics code as this would be computationally expensive.

The single-zone code takes as input a list of temperatures and densities, known as a trajectory, along with the reaction network described in section 4.1 (an example trajectory.input file is shown in Figure 4.4). The physics solver then reduces the reaction network according to which reactions will occur during each time-step. If the timestep does not conserve the number of particles to within a tolerance,

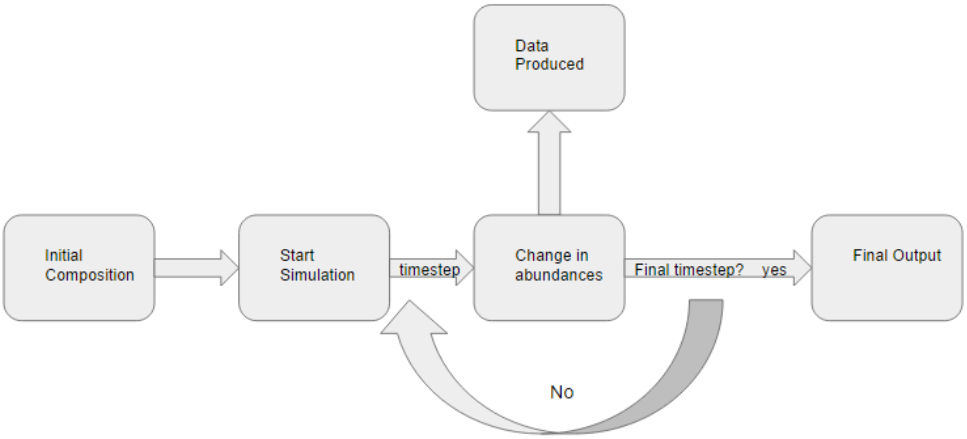

Figure 4.3: representation of the ppn process. The initial chemical composition of the burning material is specified, and through a series of timesteps data is produced. Subtimesteps do not produce data.

then a sub-timestep is introduced. The sub timestep runs the simulation over a shorter period of time to ensure that the divergence from the original number of particles is small. Each particle is not followed individually by the code as this would be computationally very expensive. However by ensuring that the number of particles is preserved through timesteps, to a tolerance, the obtained yields can be relied upon to be an accurate representation of the actual burning processes. Figure 4.3 shows the general flow of the ppn code. The initial isotopic composition is specified and is processed through a number of timesteps as outlined in the trajectory file. Data is produced at each timestep, as well as a final file which contains all of the data produced through the simulation, which is produced at the end. Subtimesteps do not produce output data.

In order to ensure that the ppn code was installed correctly and producing sensible data, a different scenario was tested and the output compared with XRB simulations undertaken previously. The results of these initial tests were found to be identical and so it was assumed that the installation was successful.

4.3 mppnp - The Multi-Zone Post processing Network

The multi-zone post processing code is able to simulate environments which have mixing between zones. This is more computationally expensive than the single-zone approach, however it is more widely applicable and allows a wider range of stellar environments to be modelled faithfully. The multi-zone

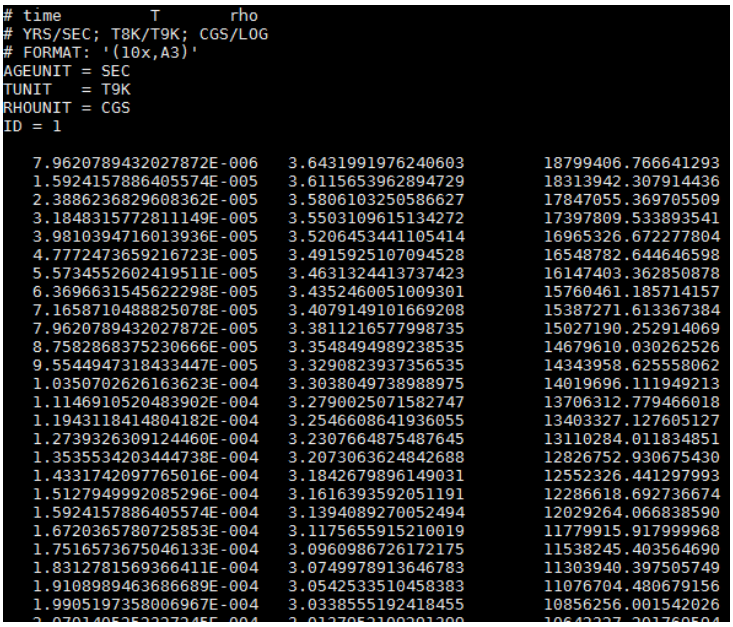

```
# time         T       rho
# YRS/SEC; T8K/T9K; CGS/LOG
# FORMAT: '(10x,A3)'
AGEUNIT = SEC
TUNIT   = T9K
RHOUNIT = CGS
ID = 1

   7.9620789432027872E-006   3.6431991976240603        18799406.766641293
   1.5924157886405574E-005   3.6115653962894729        18313942.307914436
   2.3886236829608362E-005   3.5806103250586627        17847055.369705509
   3.1848315772811149E-005   3.5503109615134272        17397809.533893541
   3.9810394716013936E-005   3.5206453441105414        16965326.672277804
   4.7772473659216723E-005   3.4915925107094528        16548782.644646598
   5.5734552602419511E-005   3.4631324413737423        16147403.362850878
   6.3696631545622298E-005   3.4352460051009301        15760461.185714157
   7.1658710488825078E-005   3.4079149101669208        15387271.613367384
   7.9620789432027872E-005   3.3811216577998735        15027190.252914069
   8.7582868375230666E-005   3.3548494989238535        14679610.030262526
   9.5544947318433447E-005   3.3290823937356535        14343958.625558062
   1.0350702626163623E-004   3.3038049738988975        14019696.111949213
   1.1146910520483902E-004   3.2790025071582747        13706312.779466018
   1.1943118414804182E-004   3.2546608641936055        13403327.127605127
   1.2739326309124460E-004   3.2307664875487645        13110284.011834851
   1.3535534203444738E-004   3.2073063624842688        12826752.930675430
   1.4331742097765016E-004   3.1842679896149031        12552326.441297993
   1.5127949992085296E-004   3.1616393592051191        12286618.692736674
   1.5924157886405574E-004   3.1394089270052494        12029264.066838590
   1.6720365780725853E-004   3.1175655915210019        11779915.917999968
   1.7516573675046133E-004   3.0960986726172175        11538245.403564690
   1.8312781569366411E-004   3.0749978913646783        11303940.397505749
   1.9108989463686689E-004   3.0542533510458383        11076704.480679156
   1.9905197358006967E-004   3.0338555192418455        10856256.001542026
```

Figure 4.4: An example of a trajectory file. Units are specified in the header of the file. The columns represent, from left to right: time, temperature and density. Each row represents a timestep in the simulation.

approach is necessary in environments such as massive stars with convective regions, where mixing plays a significant role in the nucleosynthesis of material.

The multi-zone code works in a conceptually similar way to the single-zone model. Trajectories containing information on the temperature and density for a particular section of material, as well as its initial abundances, are used to solve the partial differential equations which make up the reaction network. However, rather than there being only one trajectory there are hundreds or thousands, each with their own particular profile and initial abundances. Each of these reaction networks is solved by an individual processor, and then a master node receives the information from each processor and adjusts the isotopic abundances in each zone to account for mixing in the system.

The multi-zone code was not selected for this investigation for a number of key reasons. Firstly, the tracer particles which provide the necessary trajectories in the different sections of the stellar environment were not available at the time of completion (see appendices for more information on the production of the multi-zone hydrodynamics data). Secondly, it is not clear that in this scenario mixing would occur between the different burning regions (private communication, C. Fryer, July 2016). This would therefore make it unnecessary to use the multi zone model as, if greater resolution is needed it is sufficient to simply

increase the granularity of the radial and accretion steps taken in the one zone calculations and asses the change in nucleosynthesis products. Finally, the theory developed by Chevalier [5] presenting the results of accretion onto a compact object provide an excellent description of the conditions in such a system, being only a few percent different from full hydrodynamical simulations. This means that the increased accuracy from the full simulation may not influence the results of the investigation to any significant degree and may, in fact, be a smaller contribution than the choice of many different parameters such as the mass of the compact object and the reaction rate libraries used.

4.4 The Reaction Network

The reaction network consists of over 50,000 individual rates, detailing the production and destruction of each isotope in the network through all known channels for that species. This is achieved through solving a series of partial differential equations:

$$\dot{Y}_i = \sum_j \alpha_i^j Y_j + \sum_{j,k} \alpha_{jk}^i Y_j Y_k + \sum_{i,k,l} \alpha_{jkl}^i Y_j Y_k Y_l \tag{4.1}$$

Equation 4.1 gives the form of the differential equation. $\dot{\mathrm{Y}}_i$ is the rate of change of species i. The first, second and third terms are concerned with photo disintegration and β-decays, two body and three body interactions respectively. All of these terms are therefore temperature dependent, however the β-decay component is not, due in part to a lack of reactions in the NuGrid reaction network for isomeric states (see section 3.4.3).

The solver takes the input from the reaction network, applies the necessary sub-timesteps and adapts the network to contain the relevant reactions for the conditions specified [11]. Each isotope which is chosen (depending on the burning conditions) is solved for at each time step, meaning that up to 5,800 of equation 4.1 will be solved at each step. This is done through the use of a newton raphson linear algebra solver.

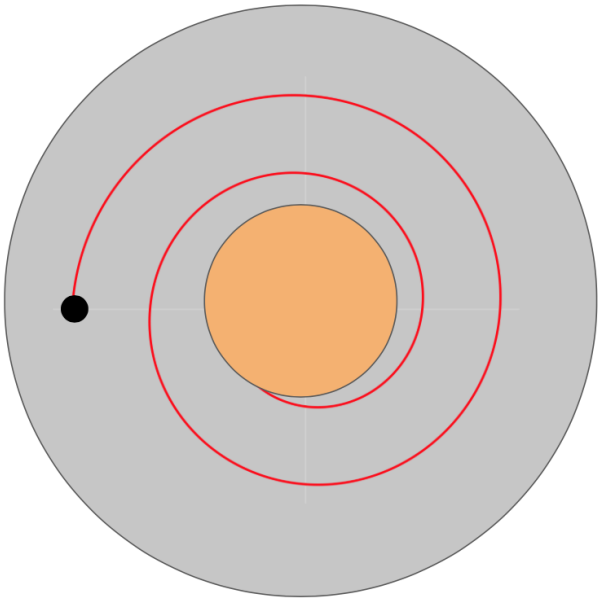

Figure 4.5: Schematic example of the motion of the neutron star through the envelope of the RSG. As the NS moves closer to the core of the companion, the accretion rate increases due to the increase in density. A maximum accretion rate of approximately $\dot{M} = 10^5 M_\odot/yr$ can be expected at the interface of the core (Fryer, private communication: July, 2016), as such this was chosen to be the upper limit for the investigation.

4.5 Generating The Trajectories

A simple Fortran code was written to produce the trajectories for the CENS system, applying the work of Chevalier. The code is included in the Appendix C and was written by Fryer, with small changes made by the author. These changes were translating to Fortran95, changing how timesteps were handled in the code such that any granularity of timestep could be selected through the parameter no_of_timesteps, as well as adjusting the movement of material in the simulations.

Motion of the neutron star in the envelope of the companion proceeds, in principal, as in Figure 4.5 although the actual path taken will of course vary. As the neutron star proceeds from the outer layers of the RSG, it passes through steadily denser material, thus increasing the accretion rate. This continues until roughly the point where the NS and RSG core touch, at which point an accretion rate of approximately $\dot{M} = 10^5 M_\odot/yr$ is expected (Fryer, private communication: July, 2016).

The motion of the material accreted onto the NS has been modelled as a buoyant bubble of gas

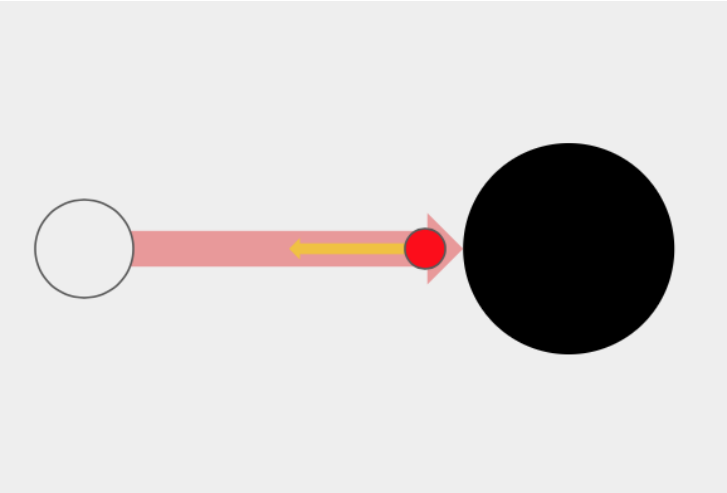

Figure 4.6: Schematic example of the motion of material falling to a radius r above the surface of the neutron star. The large grey circle is the unprocessed material falling in, whilst the smaller red circle is the $\approx 15\%$ of material predicted to escape the NS.

using the Brunt-Väisälä formula to describe the motion of the material. This gas falls onto the NS at near free-fall speeds, reduced by a factor of $0.1\times$ free-fall due to the presence of material providing an unknown frictional force until it rebounds and moves directly out from the surface again as shown in Figure 4.6. This is only the case for r > 40 km as below this the code gives unphysical results for this motion. Results from r < 40 km follow only the motion outwards to avoid collision with the surface of the neutron star. As the change in radius during the motion of the bubble is dependant on the current radius, it was concluded that this would be the simplest way to ensure that unphysical conditions were not met. Results at these radii therefore follow a different burning regime which is discussed in the results section.

The effects of neutrino cooling on the system were also investigated however, on the short time scales of the simulations run here the change in temperature due to deleptonisation of the material is small.

Chapter 5

Results

The results are presented here from highest accretion rate to lowest. Sections omit accretion depths if the results are very similar between depths. Figures 5.1 and 5.2 show the initial abundances of the elements identified in Levesque et al [1] for comparison with the processed material. Solar metalicity was chosen as the initial composition for the material being accreted onto the neutron star. The enhancements identified in Levesque et al [1] are relative to solar and so a direct comparison with their results can be achieved. Also, given the very short burning time scales involved (each run lasts only $4x10^{-4}$s, and the first time step is of the order $5x10^{-6}$s), it was decided that the precise composition of the accreted material would have a small effect on the burning products - certainly smaller than the currently unknown parameters such as the motion of the bubble, which would require a full hydrodynamical model to describe. The effect of varying initial composition in the less extreme conditions of lower accretion rates and larger radii may be more pronounced, however investigating this was beyond the scope of this project. Additional abundance charts have been included in Appendix C to illustrate the short burning timescales in most models - it can be seen from these that the specific initial composition is very quickly washed away. This may not be the case for material with very low metalicities, for example pop III stars, as it may be found that the 5-8 mass gap cannot be bridged in these short burning times but, as above, investigation into these effects is beyond the scope of this project.

In models between 50 and 100 km, the bubble of material being accreted onto the neutron star

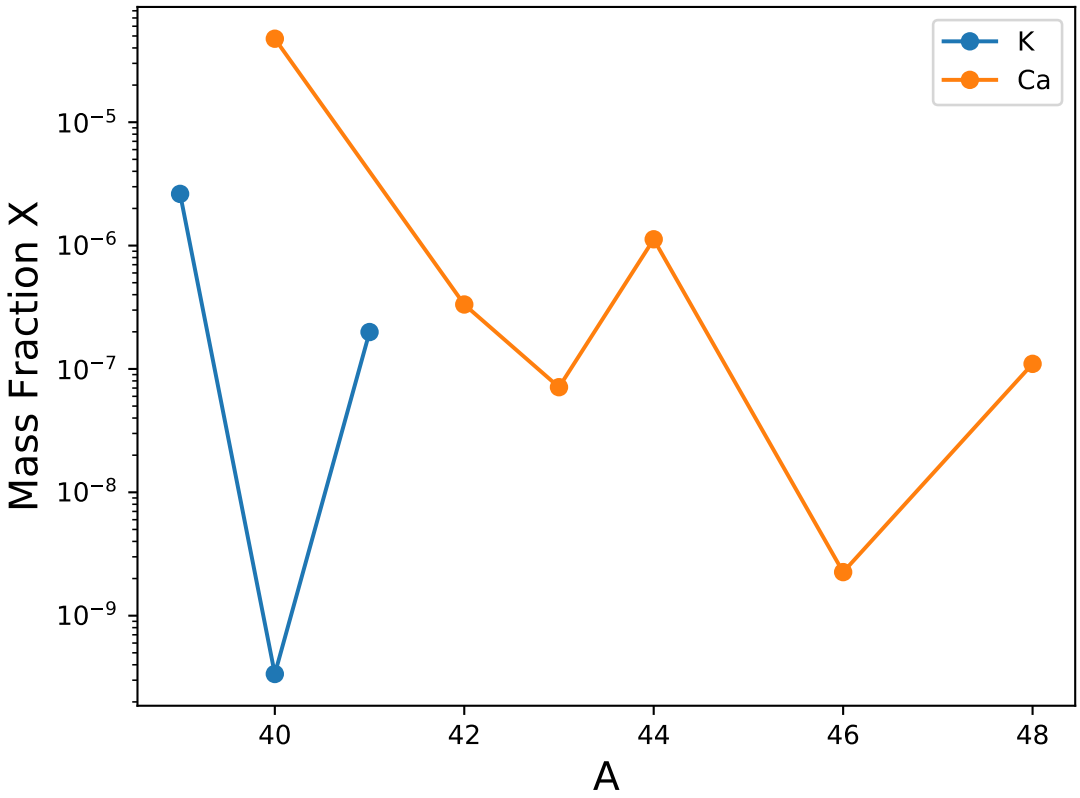

Figure 5.1: Initial abundances of K and Ca, identified in Levesque et al. [1] as being enhanced in the spectrum of the star HV2112 . ^{40}Ca and ^{39}K comprise a significant mass fraction of the unprocessed material. These abundances are chosen to be the same as solar, to aid comparison with observations. It was decided that the error introduced by assuming solar metalicity accreted material would be small as the initial stages of burning in most regions investigated are so extreme.

undergoes one oscillation around its equilibrium position, moving directly in towards the surface of the neutron star and rebounding after a number of timesteps - 50 in the case of these models. This was chosen to show the results of continued burning in the material with small changes in radius, of the order of 12 km. This allows a first principals investigation of the system, however any quantitative conclusions would require a full hydrodynamical model to fully describe the motion of material being accreted onto the neutron star and the true conditions experienced by the accreted material.

For material which began at radii smaller than 50 km, it was necessary to change the mixing regime as free-fall from these heights sometimes caused the bubble to travel through the surface of the neutron star, giving unphysical temperatures and densities. A small number of models in those zones where nucleosynthesis extends the furthest would benefit from further exploration with alternative motions of

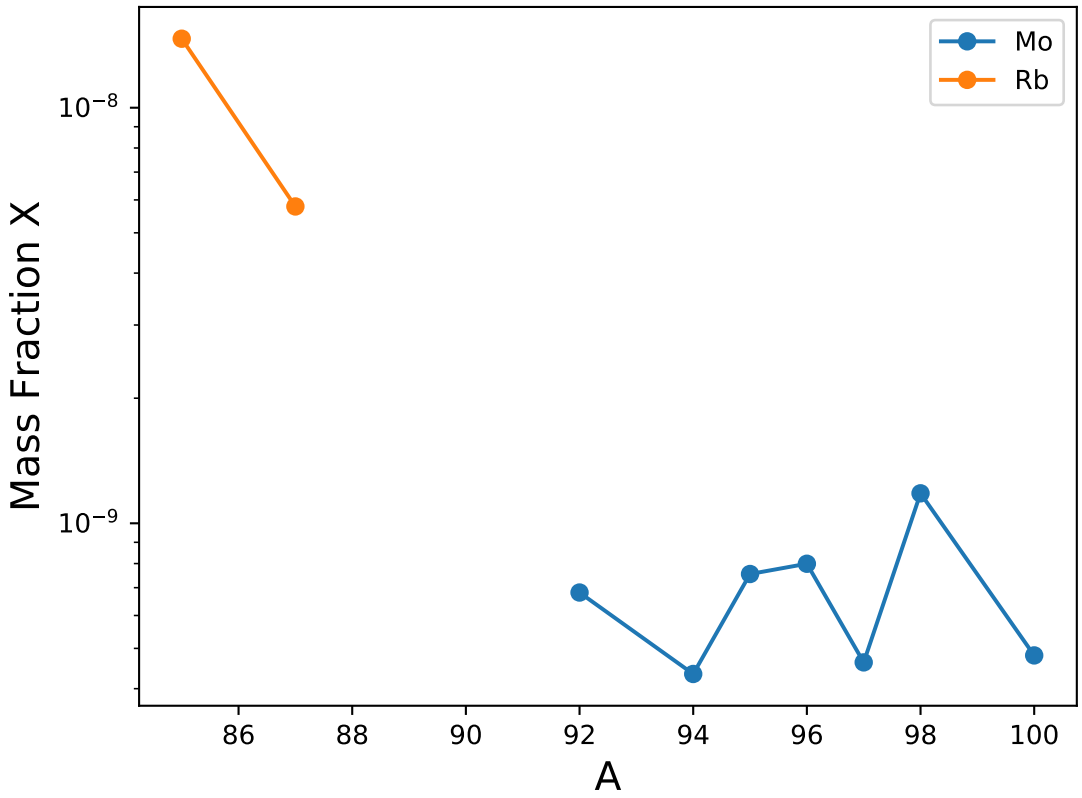

Figure 5.2: Initial abundances of Mo and Rb, identified in Levesque et al. [1] as being enhanced in the spectrum of the star HV2112.

the material. This would make a useful investigation for future work and serve as motivation to encourage the full modeling of the system.

5.1 $\dot{M} = 10^5 M_\odot/yr$

This regime represents the highest temperatures achieved in the model. Temperatures were artificially limited to T_9 = 10 as the reaction network used by the NuGrid codes is not suited to temperatures exceeding this. It can be seen from the Abundance chart 5.3 (100 km) that production of proton rich material occurs, however this only extends as far as Z≈35. The temperature at this accretion rate varies between T_9 = 5.8-6.2, as shown in Figure 5.4.

The mass fractions of isotopes of K and Ca are shown in Figure 5.5. Although the abundances of a number of isotopes of Ca and K have increased in these conditions, the most abundant isotopes have

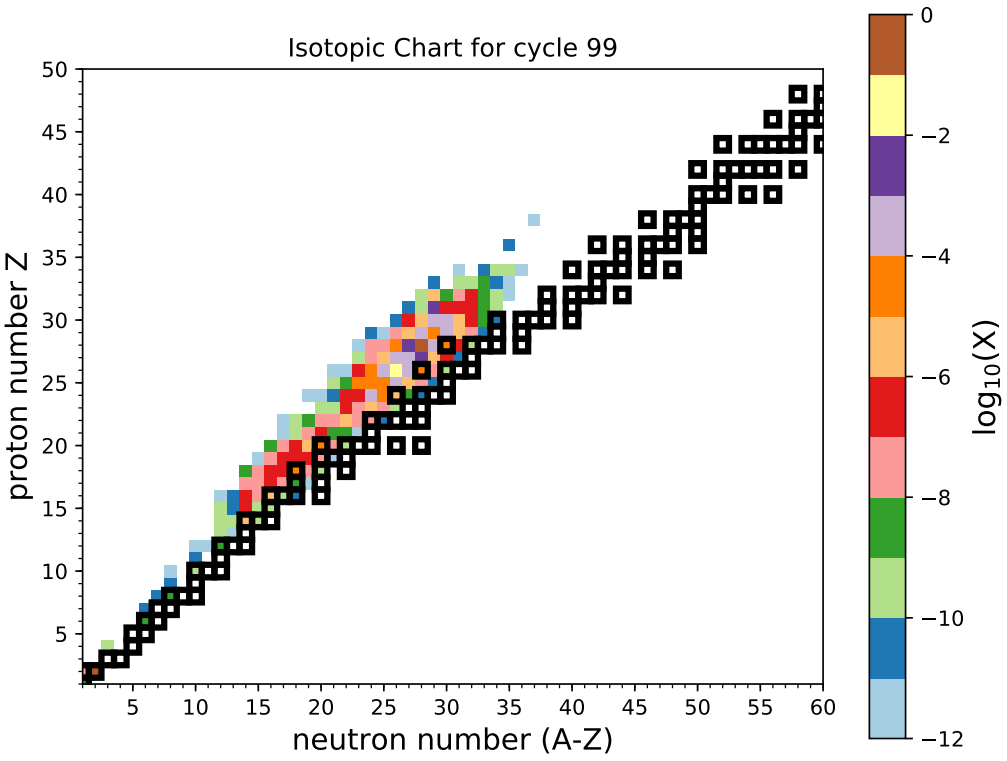

Figure 5.3: Abundance chart for accretion rate of $\dot{M} = 10^5 M_{\odot}/yr$ at 100 km. Nucleosynthesis extends to A $\approx$ 70. A large abundance of proton rich material has been produced however it remains close to the line of stability, probably due to the high probability of photodisintigration reactions at these temperatures.

also been depleted. The effect of these nuclei being processed to higher mass material means that only a modest increase in Ca is observed (see Fig 5.6). Both Mo and Rb have been depleted by more than 5 orders of magnitude, indicating that this burning regime cannot be the main production site in this system if it is to reproduce the results of Levesque et al.

At 70 km, the burning in the system moves closer towards the line of stability. Figure 5.7 shows that, although the maximum mass of nuclei formed is very similar to the r = 100 km case, the nuclei are not as proton rich. This is due to the decreasing Q-values of reactions, and therefore the lower binding energy of protons. It is easier to break up these nuclei and as the temperature increases, more photons will have high enough energy to achieve this.

For r = 70 km, there is a significant increase in the abundances of K and Ca, more hydrogen is burned in the higher temperatures experienced at this accretion depth, producing more of this material. The

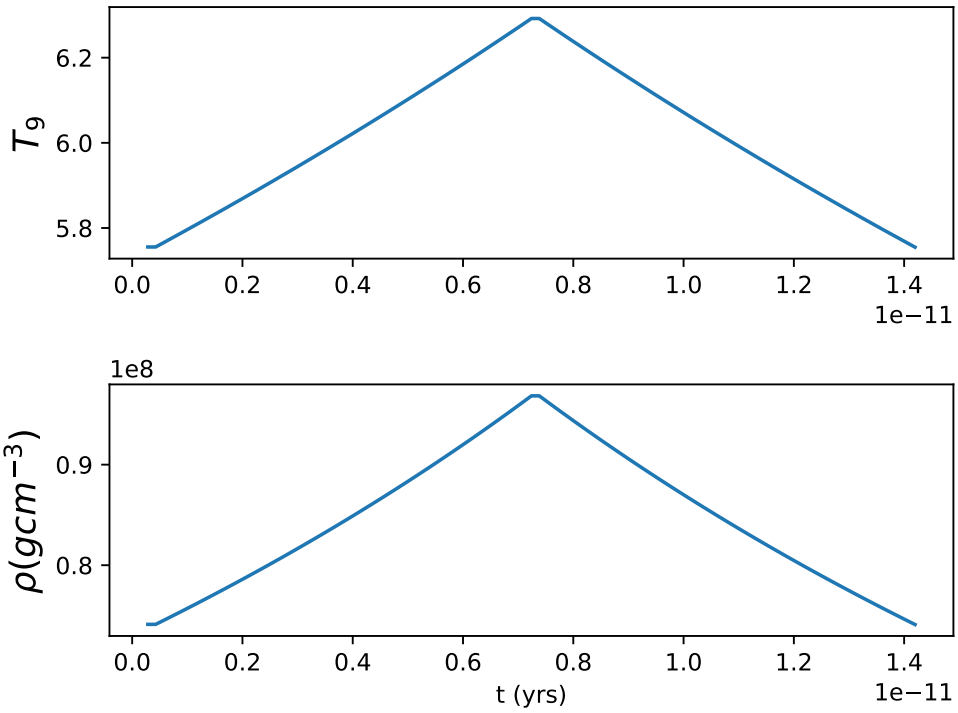

Figure 5.4: T_9 and ρ for accretion rate $10^5 M_\odot/yr$ at radius 100 km. These are the conditions experienced by the bubble of material who's products are shown in Figures 5.3,

maximum temperature achieved under these conditions is $\approx T_9 = 9.6$ (Figure 5.10). Again, Mo abundance is everly reduced, the destruction of Rb is less dramatic in this regime, with a decrease in abundance of around 10^{-3}.

At smaller radii, temperatures converge to $T_9 = 10$, due to the artificial capping of the maximum temperature. This capping is necessary as reaction rates in these conditions are not well known, and are not supported by the NuGrid codes. The results of post-processing in these conditions are very interesting, although questions about their physical significance in light of these factors remain. Figure 5.11 shows the final abundance of material processed in these conditions. Many intermediate mass isotopes are produced with significant mass fractions. Figures 5.12 and 5.13 show the enhancement for the nuclei observed in the spectrum of HV2112 and the p nuclei respectively. It can be seen that there is a significant increase in the abundance of all of the elements observed in HV2112, K is increase by a factor of around 100, Ca around 50, Mo around 5 and Rb of almost 1000. Considering the simplicity of the model, this is certainly

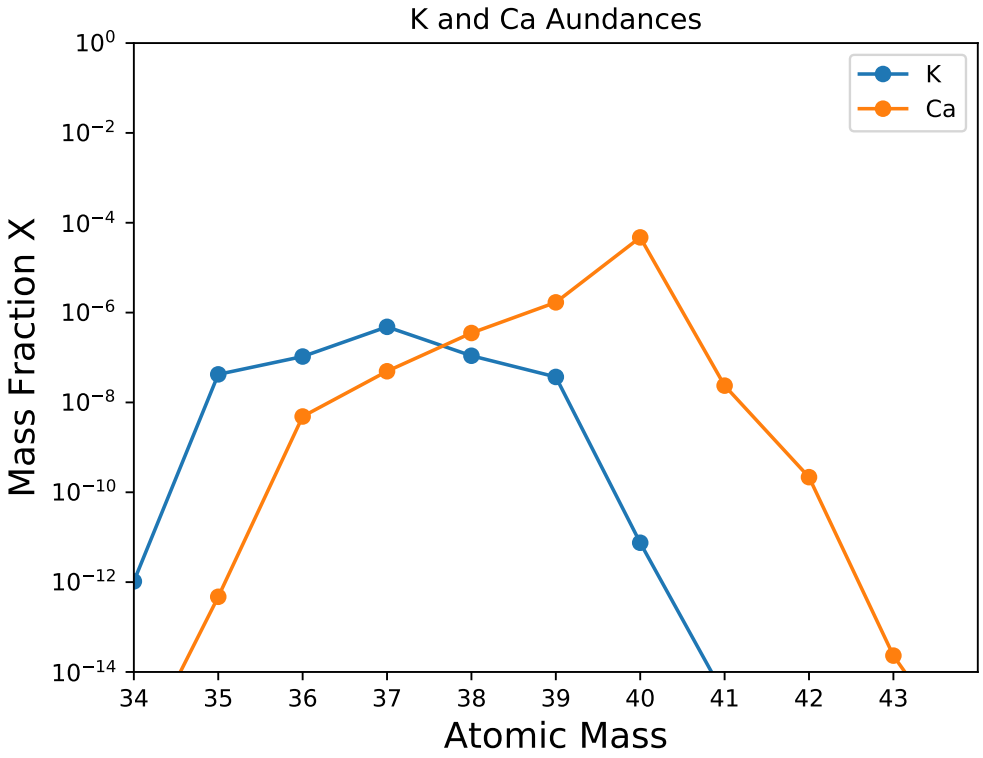

Figure 5.5: Final K and Ca abundances for accretion rate $10^5 M_\odot/yr$ at radius 100 km. A wider range of isotopes has been produced than was present in the initial composition of material. However, as is more clearly shown in Figure 5.6, there is in fact a decrease in the overall abundance of K in these conditions, and only a moderate enhancement of Ca.

a striking result.

These are the first set of conditions in which there is also an increase in the abundance of p nuclei - ^{74}Se, ^{78}Kr and ^{84}Sr are each increased by around 10-100x their initial abundances in these conditions, and provide the possiblility of an observational constraint if the abundances of these elements can be observed to be enhanced in further study of the spectrum of HV2112. Given that $\approx$ 15% of material burnt in these conditions has the potential to be ejected from the neutron star into the envelope of the companion, this could provide a viable mechanism for the enhancement of K, Ca, Mo and Rb in the atmosphere of the companion star, along with these isotopes identified here.

The results of burning at smaller radii are largely consistent with the results for r = 50km, despite the change in mixing required at this radius. There is a decrease in the abundance of Mo, leading to abundances across all isotopes roughly the same as in the unburned material, and the p nuclei shown to be

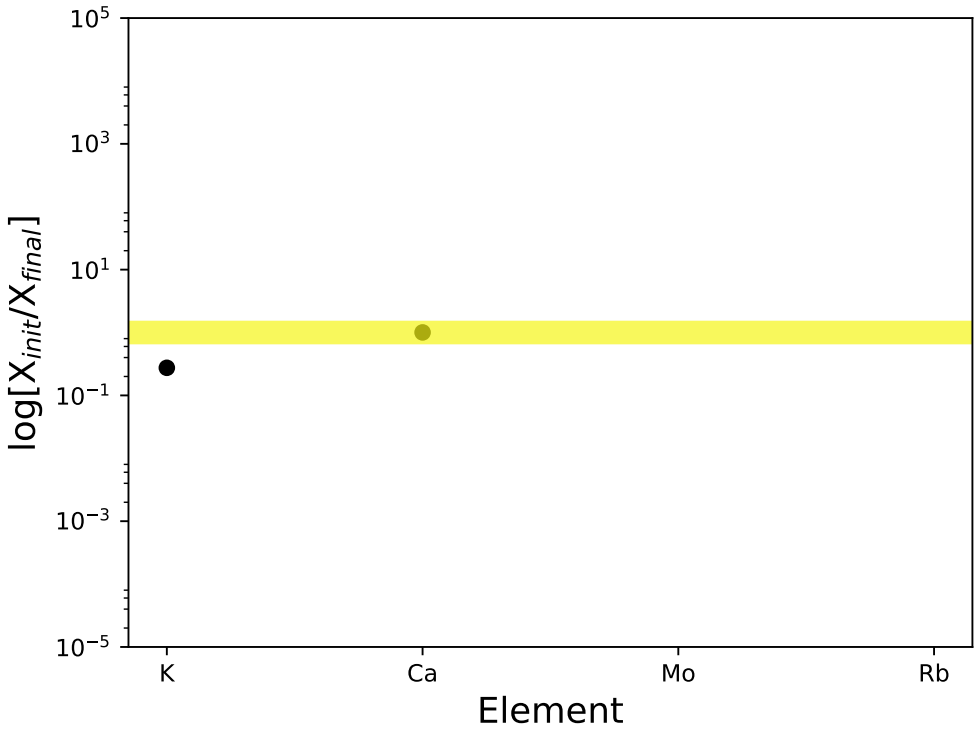

Figure 5.6: Enhancements in K, Ca, Mo and Rb relative to solar values. It can be seen from this chart that, although there is a modest increase in the abundance of Ca, the other elements detected as being enhanced in the spectrum of HV2112 have in fact been depleted in these conditions - Mo and Rb by more than 5 orders of magnitude.

enhanced in the 50 km run are only enhanced by a factor of 10 under these conditions. Burning products at r = 10 km are almost identical to those observed at 50 km, with a similar enhancement in all isotopes and elements investigated. this is likely due to the fact that both of these runs spend the full time at T_9 = 10.

5.2 $\dot{M}$ = $10^4 M_\odot/yr$

The burning products at $\dot{M}$ = $10^4 M_\odot/yr$ and r = 100 km are very interesting. The path of nucleosynthesis continues to A≈110. This means that the burning in this system has reached the extent of that expected from the rp-process, as a cluster of α unbound nuclei in this region gives rise to the SnSbTe cycle, where further burning is only possible through the capture of α particles in order to bridge this gap (Figure 5.14).

Looking next at the elements identified in Levesque et al (Fig 5.15 and 5.16) A significant odd-even

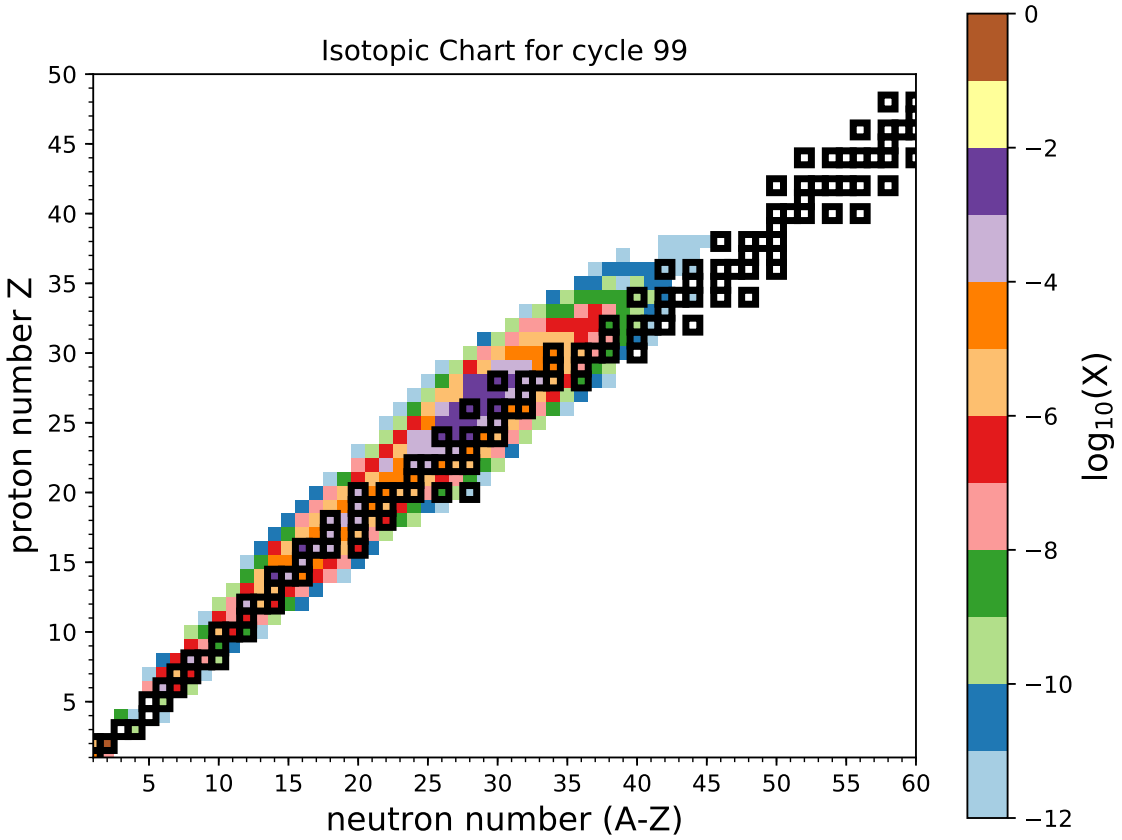

Figure 5.7: Abundance Chart for $\dot{M} = 10^5 M_\odot/yr$ and r = 70 km. This chart shows the production of slightly heavier nuclei, with production of material with A > 70. The temperatures at this radius are consistently in excess of T_9 = 7 which results in photodisintigration of proton rich nuclei. see Figures 5.8 and 5.9 for the effects on specific isotopes.

effect is evident in the abundances of Ca and K. This is due to pairing in these nuclei increasing the stability of the nuclei with even numbers of protons or neutrons, this is also the reason that Ca isotopes are generally more abundant than K in these results, as K has an odd number of protons, making it inherently less stable and favourable to produce. Ca is enhanced in these burning conditions, along with Mo, however K and Rb are both significantly depleted.

The p-nuclei are all depleted by at least 10 orders of magnitude in these conditions, indicating that they are processed either to higher mass nuclei or else destroyed through photodisintegration reactions (Figure 5.18). Temperatures range from 3.1 to T_9 = 3.8 (Figure 5.19).

At r = 70km, the temperature increases to between 6 T_9 = 4.8 and 6. Nucleosynthesis does not extend

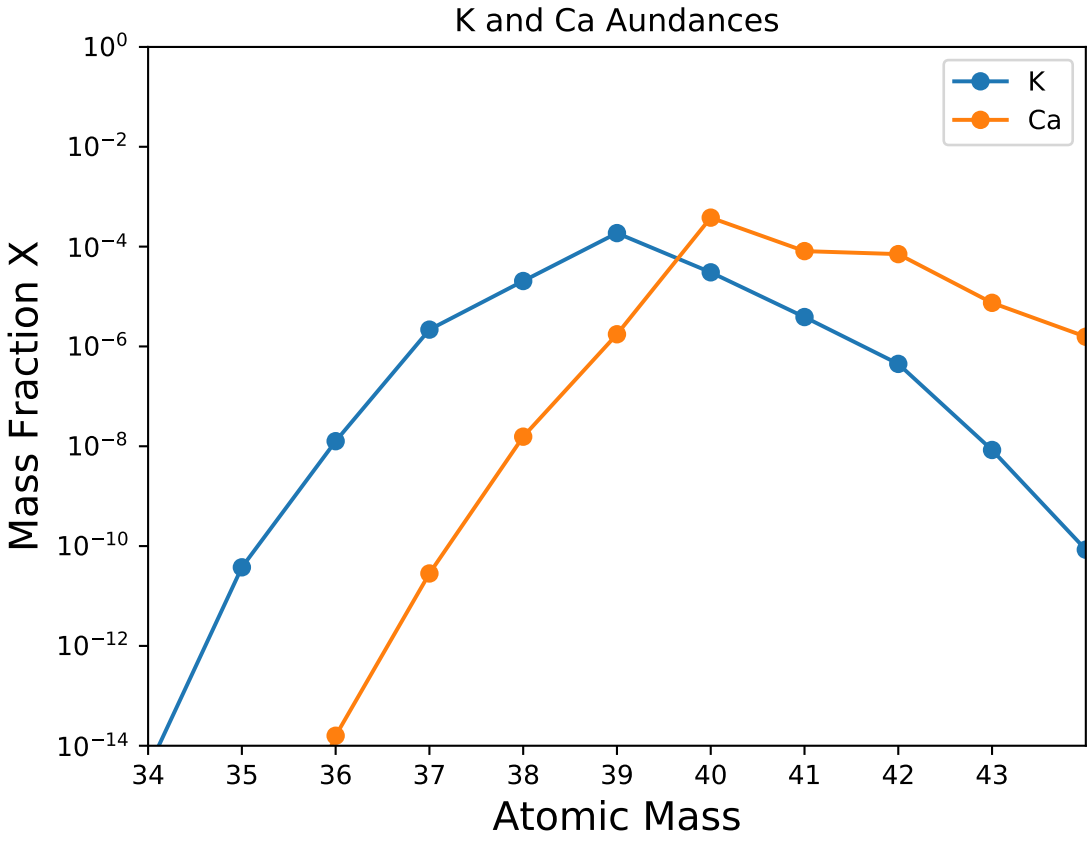

Figure 5.8: Abundances of K and Ca isotopes for $\dot{M} = 10^5 M_\odot/yr$ and r = 70 km. Higher mass isotopes are produced as compared to the r = 100 km case. See 5.9 for the enhancement factors for the elements enhanced in the spectrum of HV2112.

as far in these conditions although the nuclei produced are still fairly far from stability (Fig 5.20). At these higher temperatures nuclei near the proton dripline do not survive long enough for further capture reactions to produce heavier material.

The abundances of waiting-point nuclei decreases at higher temperatures here also. There is a general increase in the abundances of these isotopes as the material moves outwards however, their abundances decrease again towards the end of the simulation (Figure 5.21). In order to fully describe the effect on abundances in the environment, material would have to be followed as it is ejected to large radii and further reactions are no longer occurring. In this model however, it is clear that the abundances of all p nuclei, under these conditions, is decreased significantly from their starting values, as are those detected in the spectrum of HV2112.

All Levesque elements are all significantly depleted in this material, with Rb being only 10^{-3} of its

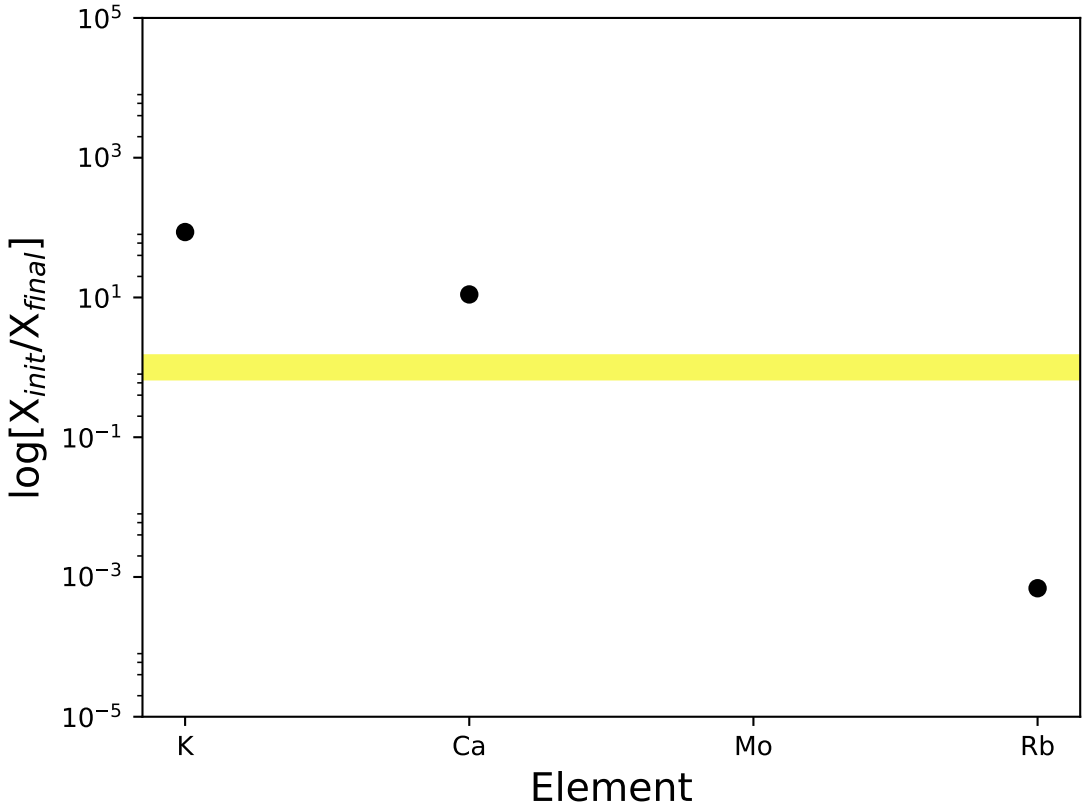

Figure 5.9: Enhancements of K and Ca isotopes for $\dot{M} = 10^5 M_\odot/yr$ and r = 70 km. A significant increase in the abundances of K and Ca can be seen - approximately 50x for K and 10x for Ca. Again, Mo is severly depleted, and rubidium is also destroyed.

original mass (Figure 5.22). These conditions are clearly not suited to the production of the material observed in the spectrum of HV2112, or of the p nuclei. Even if these isotopes were produced in CENS system, it is unclear whether or not they would survive their ejection into the companion star.

As the radius decreases to 50 km, the nuclei produced cluster around the Z≈35, this seems to be a trend in the burning regimes as larger and less tightly bound nuclei undergo photodisintegration reactions, hindering the flow to heavier nuclei (Figure 5.23) There are a larger number of reactions in equilibrium in this regime than at larger radii, including (α, p) reactions. There is an enhancement of the elements K and Ca under these conditions, however their production is reduced from previous simulations at this radius (Figure 5.24) to only 10-30x their initial abundances. The abundances of the p-nuclei are severely depleted, by more than 4 orders of magnitude for each isotope (Figure 5.25)

At r = 30 km the total Ca abundance is reduced compared with the initial abundances, although some

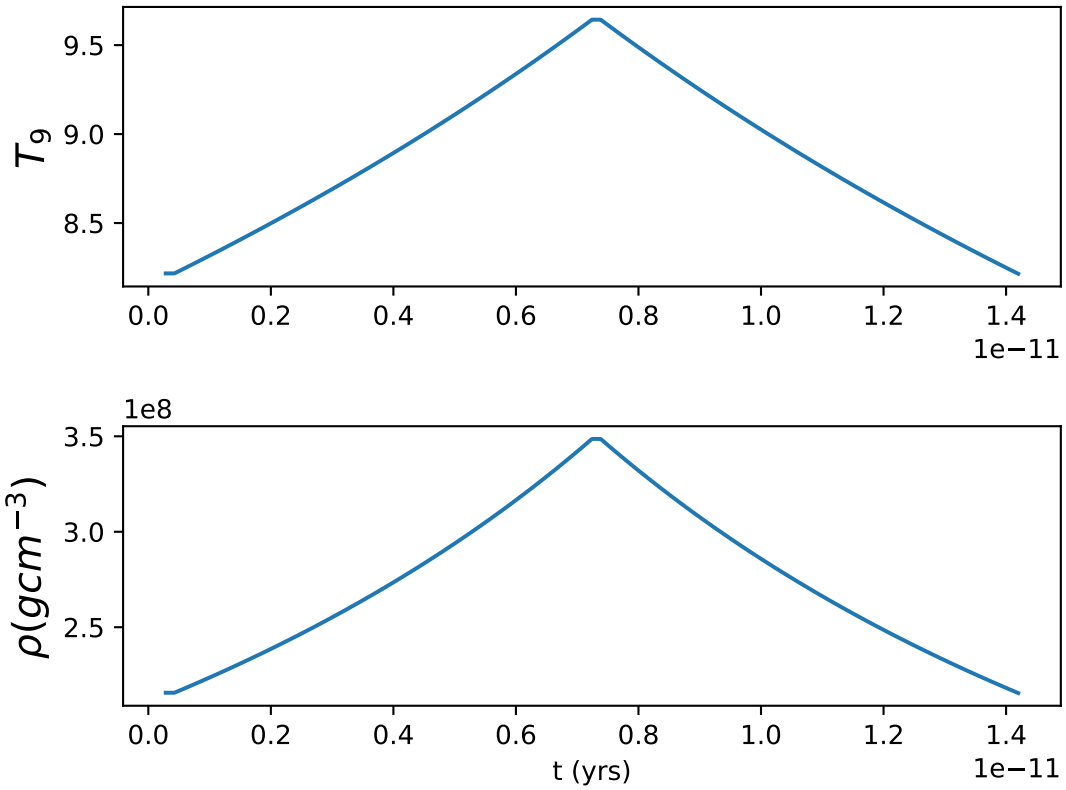

Figure 5.10: T_9 and profiles for $\dot{M}$ = $10^5 M_\odot/yr$ and r = 70 km.

of the isotopes are increased in abundance the reduction in the ^{40}Ca abundance is not compensated for (Figure 5.26). The abundances of the p nuclei and all of the elements enhanced in HV2112 have been decresed dramatically at this accretion rate and distance, in line with the abundances for $10^4 M_\odot/yr$ and r = 50 km. Due to the similarities between this run and the r = 50 km case, the graphs will not be reproduced here.

At 10 km, the path of nucleosynthesis no longer favours proton rich nuclei (Figure 5.27). The temperature in this model starts at T_9 = 10 and declines to T_9 = 7 over the duration of the simulation (Figure 5.28). The difference the shape of the temperature and density profile is due to the different mixing regime employed at these radii. The abundance chart shows an even distribution of products around the line of stability. This is because only the most strongly bound nuclei will not lose nucleons to photodisintegration reactions. There is an increase in the abundance of Rb in these conditions, however the abundances of other elements observed in the spectrum of HV2112 are depleted. ^{74}Se, ^{78}Kr and ^{84}Sr

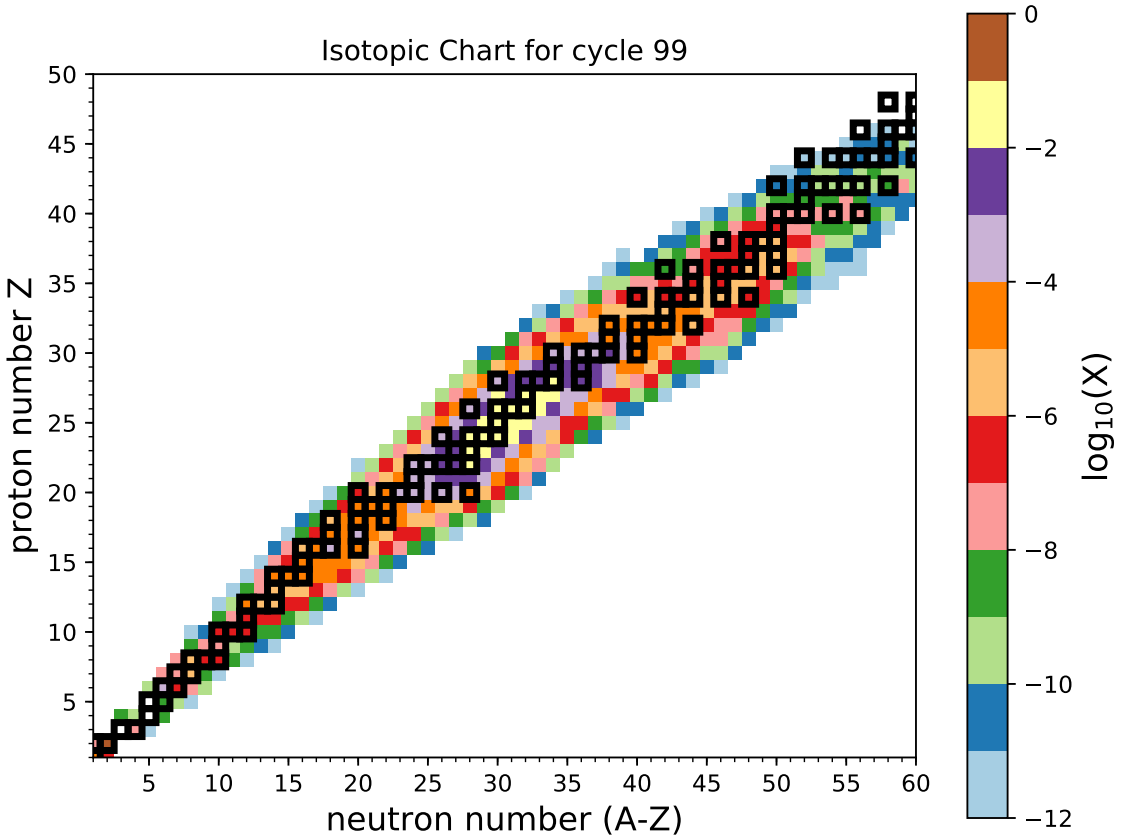

Figure 5.11: Abundance chart for $\dot{M}$ = $10^5 M_\odot/yr$ and r = 50 km. Intermediate mass elements are significantly enhanced in these conditions and nucleosynthesis continues to nuclei with masses well in excess of A = 100.

are significantly enhanced in these conditions (Figure 5.30) however, without K, Ca and Mo enhancement, this environment cannot account for the spectrum of HV2112.

5.3 $\dot{M}$ = $10^3 M_\odot/yr$

The nucleosynthesis occurring at this accretion rate appears to be the most extensive, especially between 100 and 60 km. It extends to A≈170 for r = 100 km (Figure 5.31). These conditions therefore must incorporate α capture processes due to the α unbound SnSbTe cycle, or captures on heavier isotopes already present in the accreted material. There is also a very large increase in the proportion of calcium produced, along with and enhancement in Mo (Figure 5.33) - 1000x and 50x the initial abundances

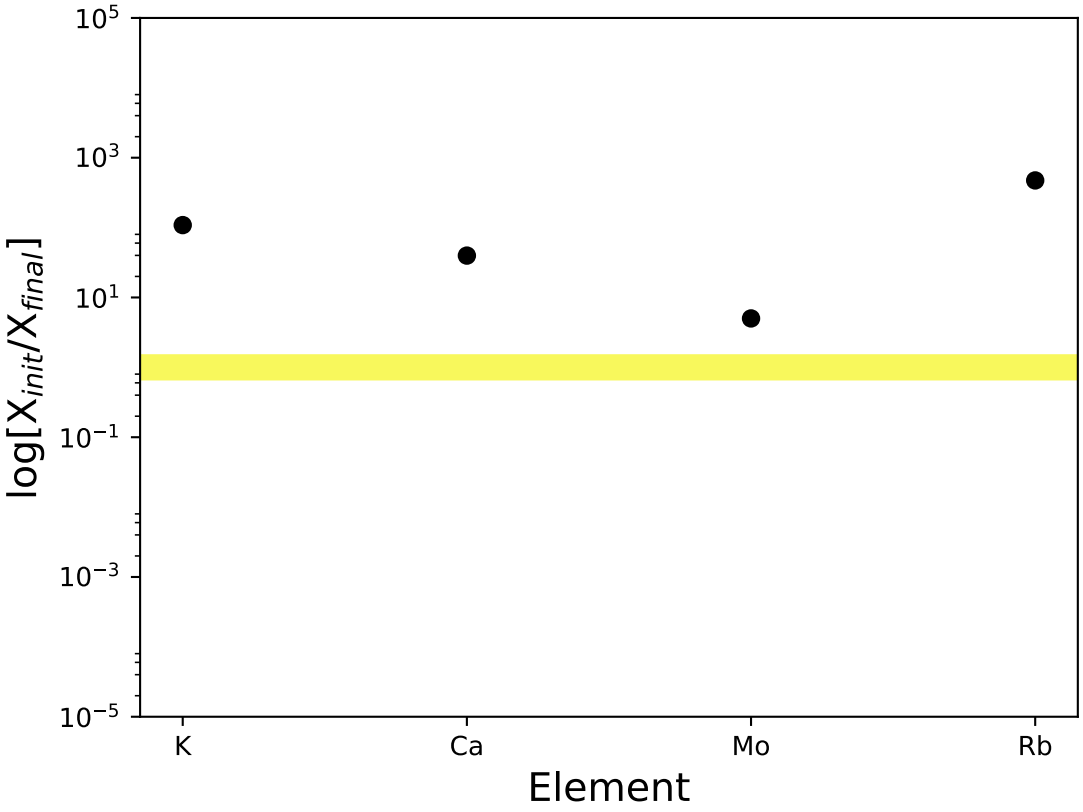

Figure 5.12: Enhancement of K, Ca, Mo and Rb for $\dot{M}$ = $10^5 M_{\odot}/yr$ and r = 50 km. All elements are significantly enhanced from their initial abundances.

respectively. As with many other burning regions investigated, this is an encouraging result however without an increase in K and Rb this burning regime is excluded.

The temperature under these conditions ($\dot{M}$ = $10^3 M_{\odot}/yr$ and r = 100 km) reaches a peak of $T_9 \approx 2.2$ (5.34)- much milder conditions than have been previously investigated, therefore it is not unreasonable to assume that the initial isotopic abundances of the accreted material will have a larger impact on the final abundances than in previous conditions.

The path of nucleosynthesis extends to A≈190 at r = 80 km (Figure 5.35) however the production of K, Ca, Mo and Rb remain very similar to the r = 100 km case, with only Ca and Mo overproduced. The overproduction of Ca is also reduced from the r = 100 km case to only around 50x the initial abundance, however as the results are otherwise similar the graph for this radius has been omitted. The r = 60 km run continues this trend, with Mo being destroyed and Ca enhanced by a factor of 2-3 only.

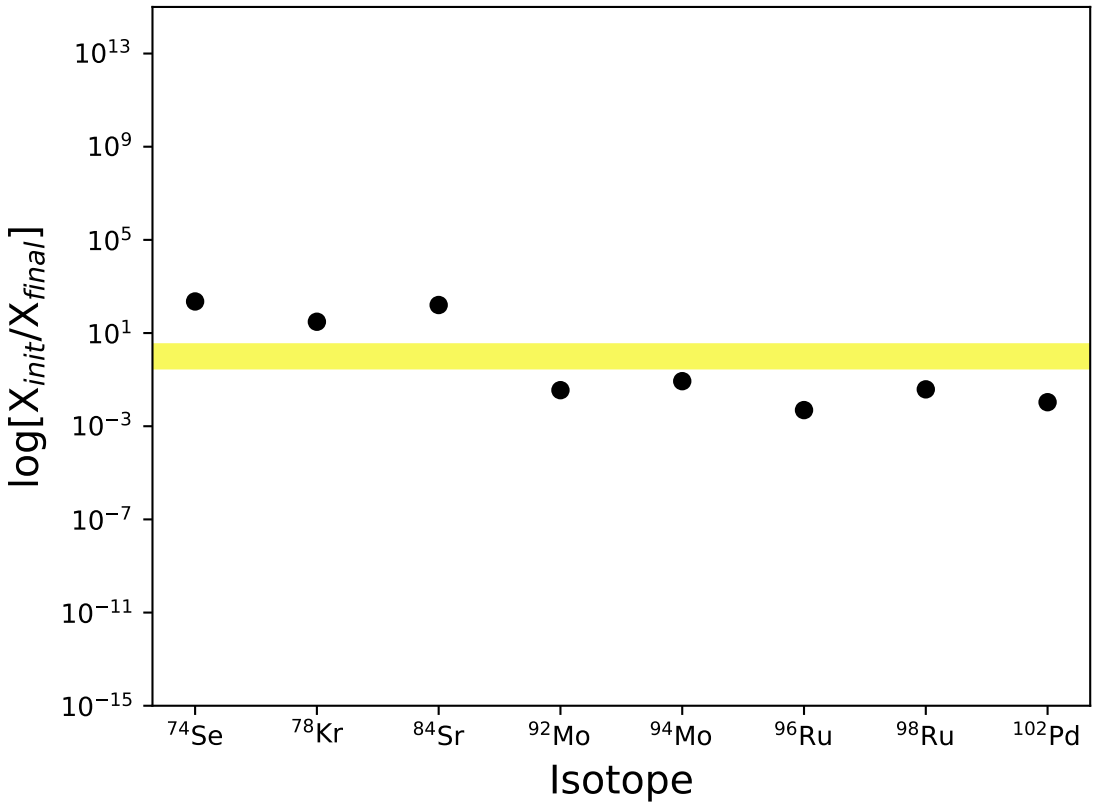

Figure 5.13: Enhancement of P nuclei $\dot{M}$ = $10^5 M_\odot/yr$ and r = 50 km. This is the first set of conditions for which there is a significant increase in abundance of any of the p nuclei.

Conditions at 40 km lead to interesting products. Although K and Ca abundances are reduced by factors of ≈100 each, Rb is enhanced by a factor of 10^4 and Mo by 10^5 (Figure 5.36). Also under these conditions, the abundance of the p nuclei ^{74}Se, ^{78}Kr, ^{84}Sr, ^{92}Mo, ^{94}Mo, ^{96}Rb and ^{98}Rb are all increased by factors of 10^5 - 10^2 (Figure 5.37). It should be noted that motion of the bubble of accreted material for this run was consistent with the motion of the bubble as in the 60, 80 and 100 km runs. Comparison with models with alternative motion should be made to assess the impact of this.

The run $\dot{M}$ = $10^3 M_\odot/yr$ and r = 20 km showed no significant increase in the abundance of any of the elements identified in HV2112. Plots have been omitted for brevity.

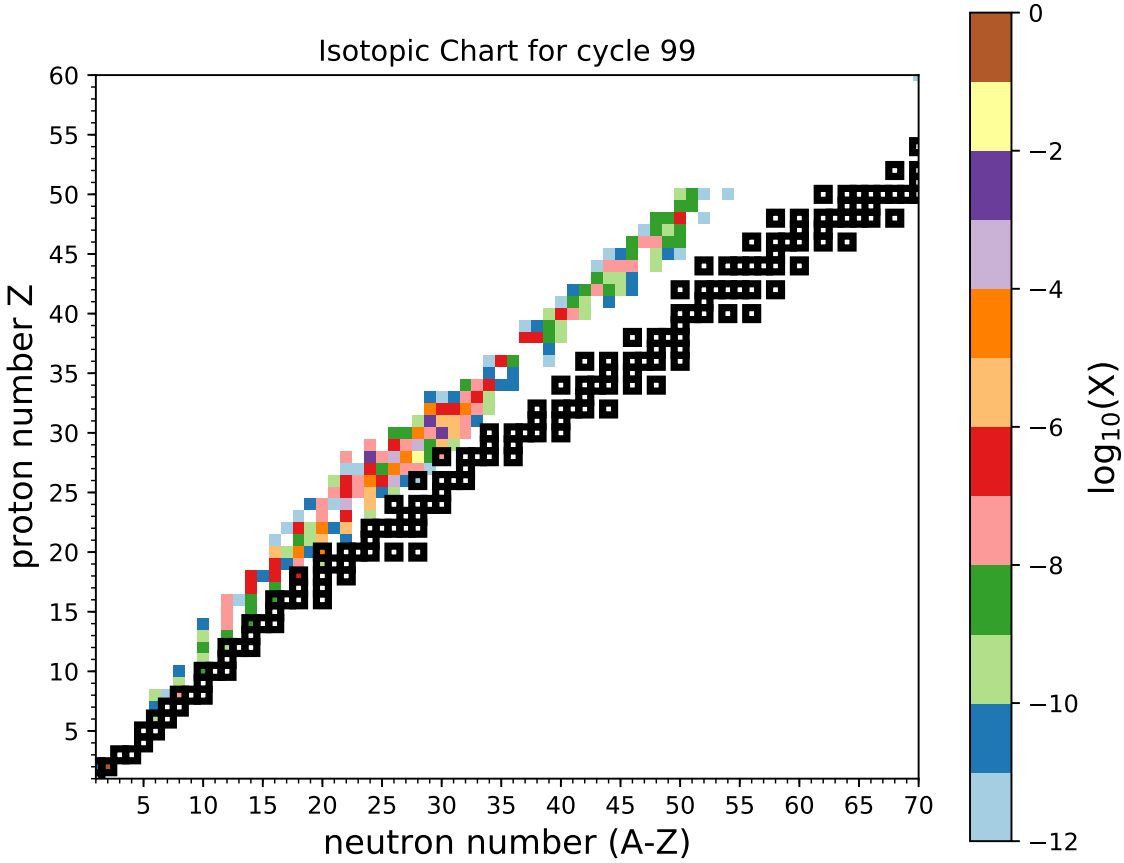

Figure 5.14: Flux chart for $\dot{M}$ = $10^4 M_\odot/yr$ and r = 100 km. Nucleosynthesis extends well beyond any of the burning zones in the $\dot{M}$ = $10^5 M_\odot/yr$ accretion rate. The maximum masses in this burning regime lie around A $\approx$ 110 where the closed SnSbTe cycle prevents further burning due to these isotopes being α unbound. This is interesting as it then encompasses the whole of the rp-process. The majority of burning processes occurring at this time are equilibrium proton capture and photodisintegration reactions.

5.4 $\dot{M}$ = $10^2 M_\odot/yr$

Lower temperatures at r = 100 km for this mass accretion rate reduce the extent of nucleosynthesis compared to the results for $\dot{M}$ = $10^3 M_\odot/yr$. Nuclei up to A$\approx$100 are produced, some of which are fairly proton rich (Figure 5.38). ^{92}Mo shows an increase in abundance of an order of magnitude, and the abundance fraction of K is larger than that of Ca for the first time in these simulations. K and Mo are enhanced under these conditions by a factor of $\approx$30 (Figure 5.39).

At r = 80 km the temperature has increased again to T_9 = 1.3 - 1.8. The maximum mass of nuclei

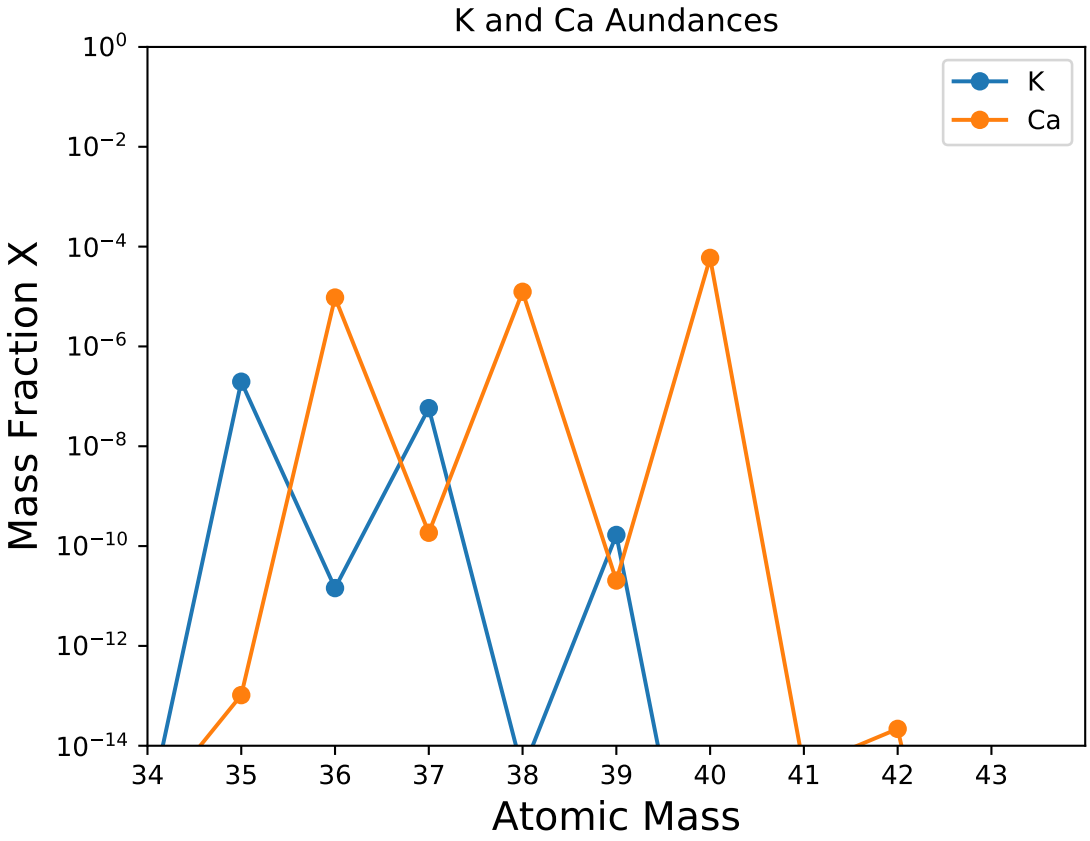

Figure 5.15: K and Ca for $\dot{M}$ = $10^4 M_{\odot}/yr$and r = 100 km. There is a strong odd-even effect visible in the production of Ca and K, and significant enhancement of a number of isotopes however there is overall only a small increase in the abundance of Ca, whilst the mass fraction of K decreases to approximately 0.1x it's original value (see Fig 5.17 for enhancement relative to solar composition.

)

produced extends to A≈130 (Figure 5.40). A significant enhancement of Ca and Mo can be observed in these conditions of around 20-30x initial abundances, and a more modest enhancement of K (Figure 5.41)

At r = 50 km, the temperature is peaks at $T_9 \approx 6$. With this movement to higher temperatures we see, as with the other accretion rates, isotopes cluster more towards low masses and closer to the line of stability. ^{36,38}Ca each comprise approximately 10^{-4} of the mass fraction under these conditions however K, Mo and Rb abundances are severely reduced by factors of more than 10^{-2}. The results are very similar to the other environments at temperatures around T_9 = 6 and so will not be reproduced here.

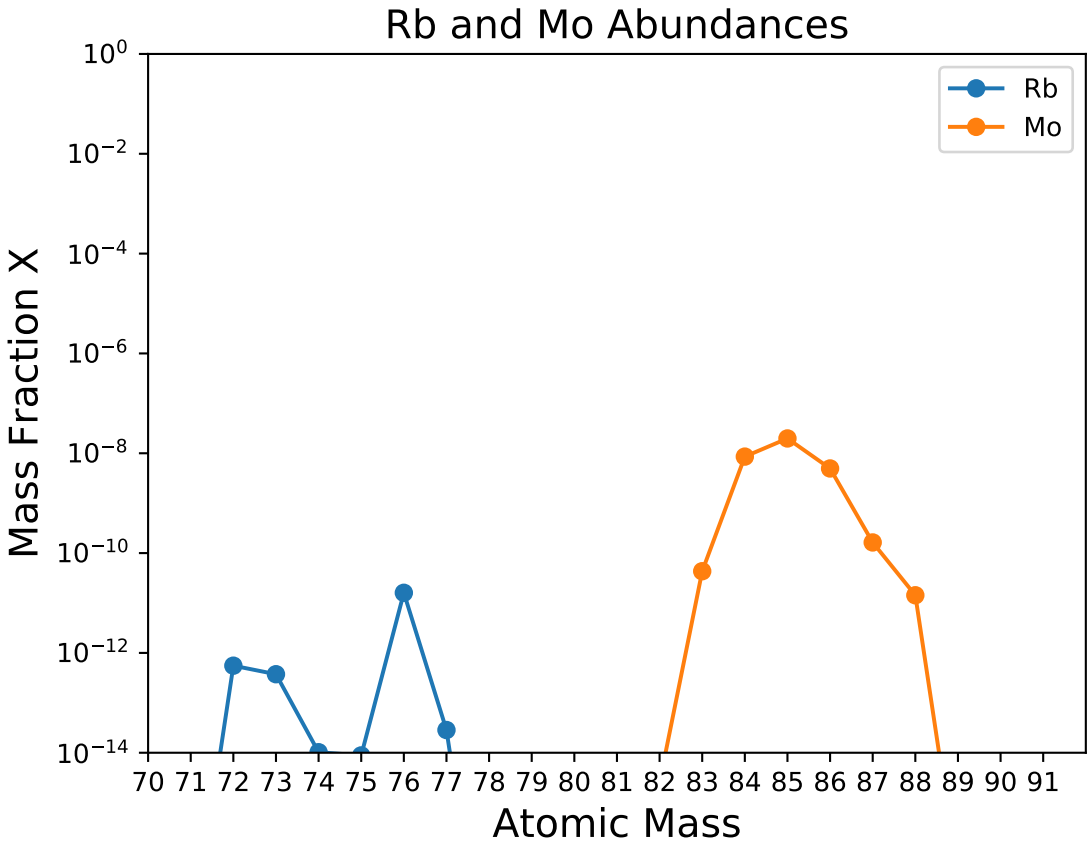

Figure 5.16: Mo and Rb abundances for $\dot{M} = 10^4 M_\odot/yr$ and r = 100 km. A wide range of Rb isotopes are produced however this comes at the expense of destruction of the more abundant isotopes, therefore the overall mass fraction of Rb decreases significantly.

5.5 $\dot{M} = 10 M_\odot/yr$

At these accretion rates, reactions are too slow to produce heavier isotopes at large radii. At r = 100 km, there is an increase in the abundance of K by a factor of 20-30. Ca is depleted, having $\approx$ 0.1x it's initial abundance at the end of the simulation, the abundances of Mo and Rb remain almost unchanged however (Figure 5.42).

At r = 80 km, K , Mo and Rb are enhanced by factors of $\approx$ 30, 2 and 20 respectively. Ca is depleted in these conditions again as was the case in the 100 km run. (Figure 5.43). These results are promising as they allow for the possibility of at least some of the material required to be produced at relatively low accretion rates as the neutron star first enters the envelope of the companion. If the envelope of the companion star is later enriched by material escaping when the accretion rate is higher, those regions

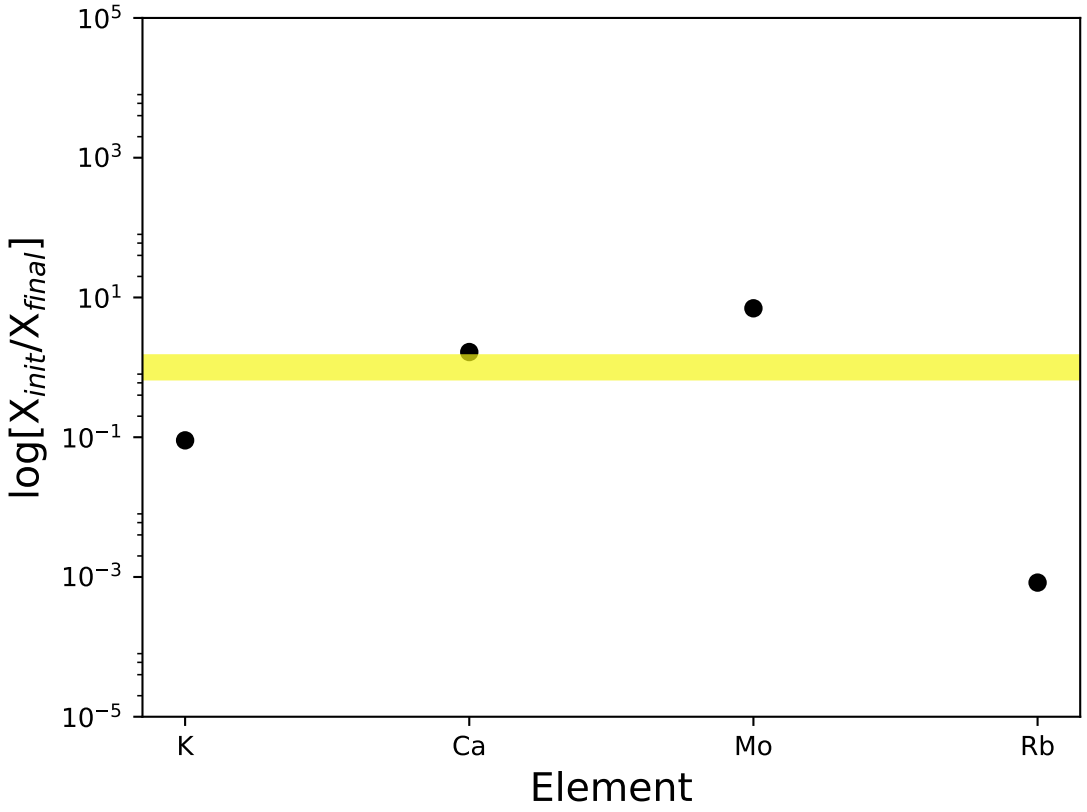

Figure 5.17: Enhancement factors for the elements identified in Levesque et al for $\dot{M} = 10^4 M_\odot/yr$ and r = 100 km. There is an increase in the abundance of Ca (2-3x initial) and Mo ($\approx$ 10x initial) however both K and Rb are significantly depleted.

may then supply the Ca needed to reproduce the observations of HV2112. The temperature under these conditions peaks at $T_9 \approx 1.2$.

At r = 60 km, Ca and Mo are overproduced while K and Rb are destroyed (Figure 5.44). Again this is encouraging as, if material is ejected from different accretion heights above the surface of the neutron star, only one accretion rate may be necessary to explain the observed over-abundances of K, Ca, Mo and Rb. It highlights the need for a full hydrodynamical model of the system however, as it is not possible to identify which of these scenarios are likely to occur and where material will be ejected from in the simple model studied here. The extent of nucleosynthesis in these conditions is again large, with material being produced up to A > 170, although with low mass fractions of the order of 10^{-10}-10^{-12} at the higher end of this mass range (Figure 5.45). This seems to be typical of regions with peak burning temperatures of the order of $T_9 \approx 3$, as is the case for this accretion rate and height.

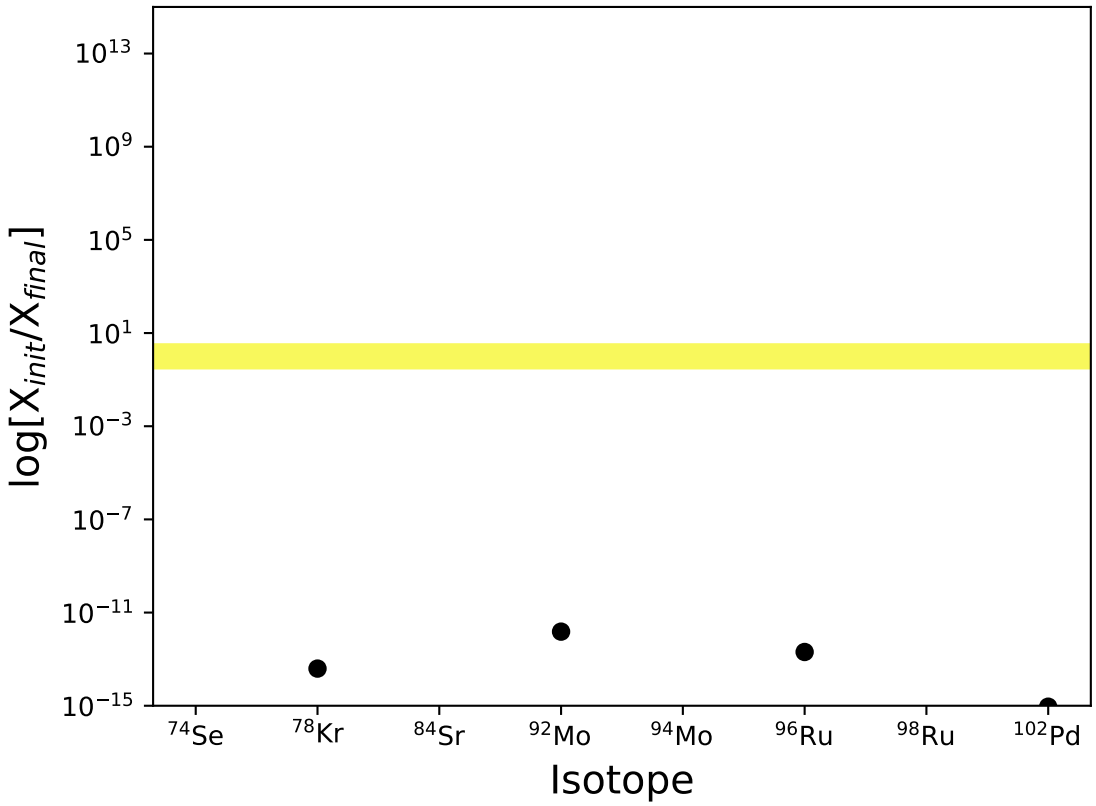

Figure 5.18: p nuclei ar $\dot{M}$ = $10^4 M_\odot/yr$and r = 100 km. All are completely destroyed, through cycling of material to higher masses or photodisintegration of these isotopes

As the radius is decreased further to r = 40 km, we again see that the material produced is concentrated around the A $\approx$ 50 region (Figure 5.46) The maximum temperature reached is T_9 = 1.4 for a significant fraction of the simulation (Figure 5.47). This results in enhancements in the abundances of K, Mo and Rb, as well as the p nucleus ^{92}Mo (Figures **??** and 5.49 respectively). It seems that some combination of accretion depths at an accretion rate $\dot{M}$ = $10 M_\odot/yr$ may be able to explain the observed over-abundances of material in the spectrum of HV2112 although Ca is destroyed at radii of 40, 80 and 100 km which may not be compensated for by contributions from the r = 60 km case. The increase in the abundance of the p nuclei mentioned above may provide further constraints on the burning conditions present in HV2112, although further work would be necessary to confirm that these isotopes are in fact produced in a full hydrodynamical model containing mixing and investigating the effects of initial abundance, dynamical instabilities of the system and possibly other unknown sources of error.

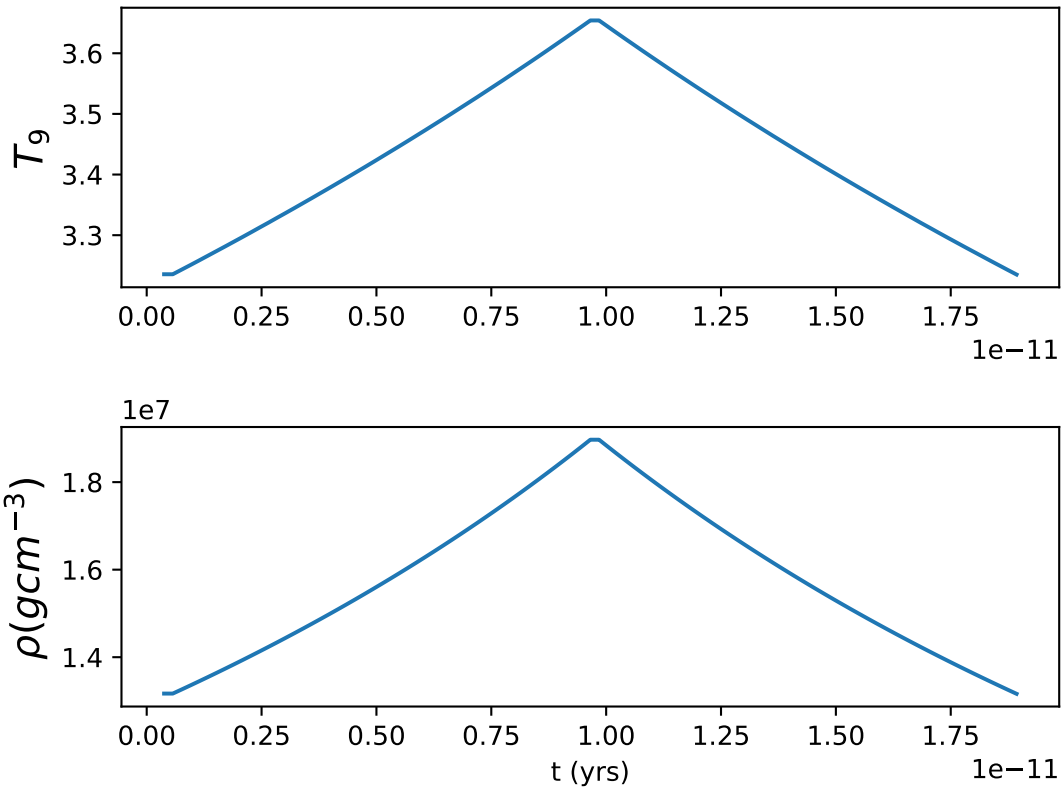

Figure 5.19: T and ρ conditions for $\dot{M}$ = $10^4 M_\odot/yr$and r = 100 km. Maximum temperature lies around T_9 = 3.8

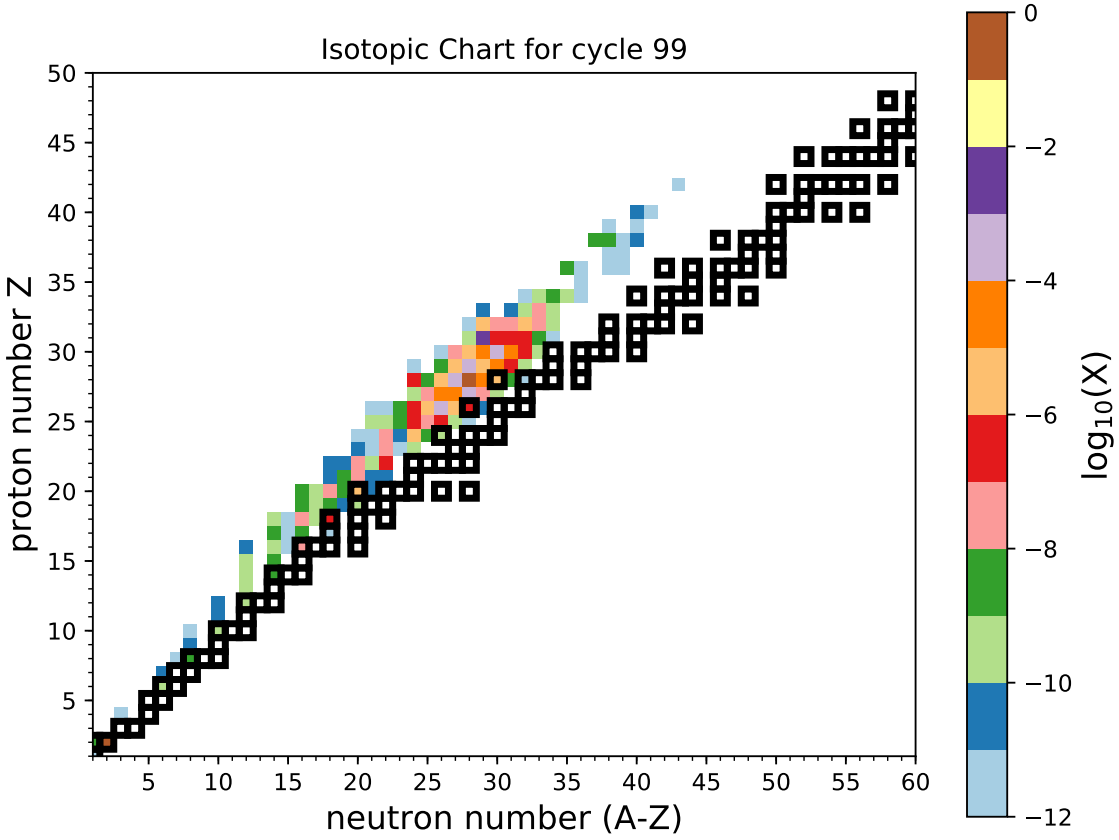

Figure 5.20: Abundance chart at $\dot{M} = 10^4 M_\odot/yr$ and r = 70. Similar reaction pathways operate in these conditions as with r = 100 km however the extent of nucleosynthesis is not as great. As can be seen in Fig 5.22 the four elements identified as being enhanced in HV2112 are also under-produced.

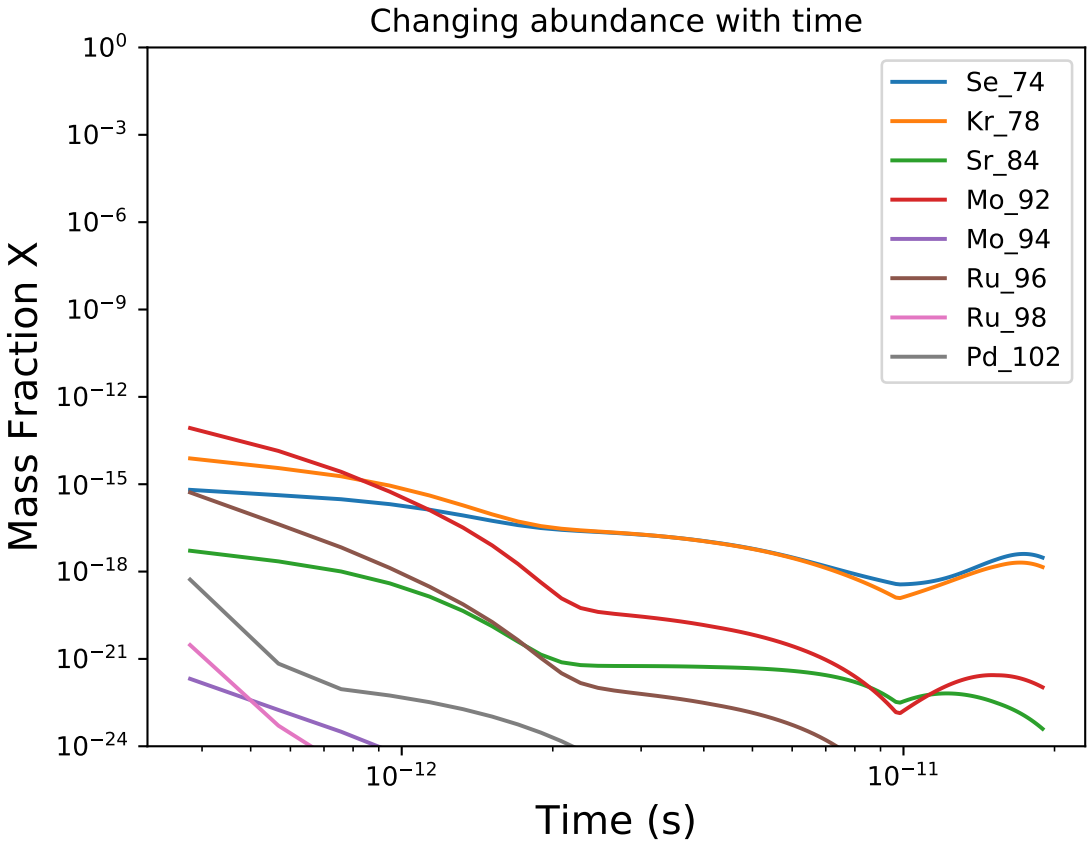

Figure 5.21: waiting-point nuclei abundances for $\dot{M} = 10^4 M_{\odot}/yr$ and r = 70 km. There is a clear increase in their abundances as the buble begins to move away from the surface of the neutron star however, towards the end of this motion the abundances of the p nuclei again begin to trail off. In order to find the final impact on abundances of these isotopes it would be necessary to follow fully the motion of the bubble of material as it is ejected to much lower temperature conditions, so that further nuclear reactions do not take place.

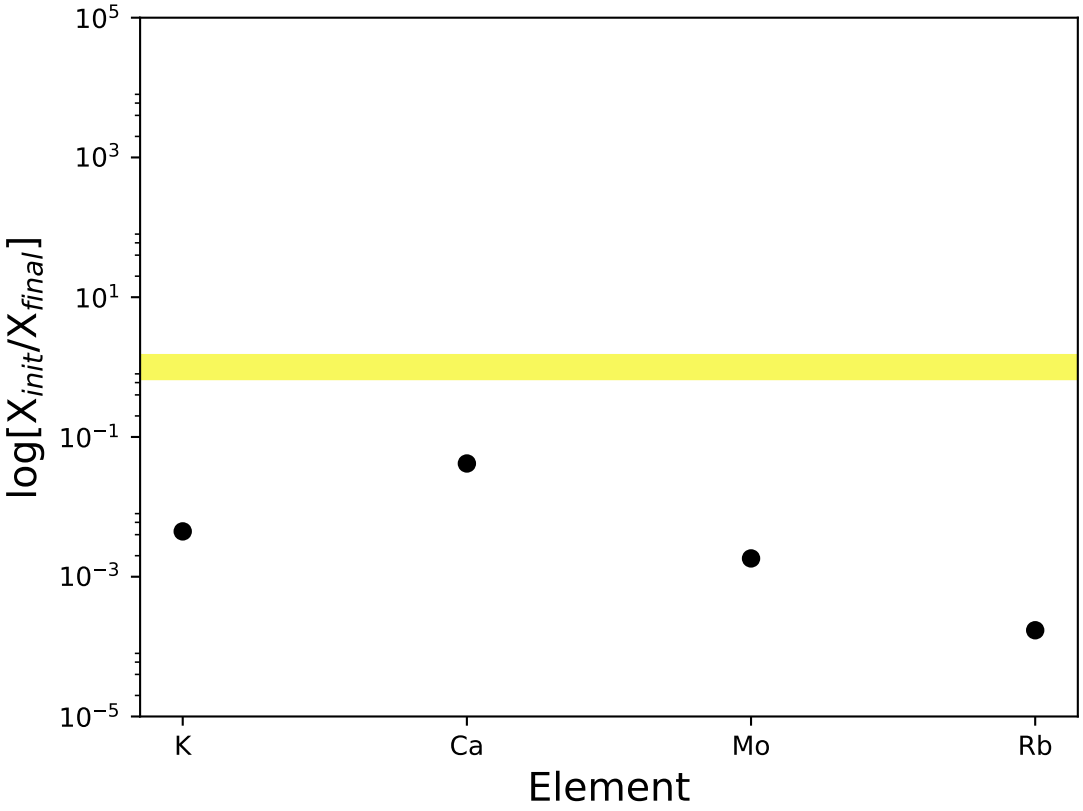

Figure 5.22: Levesque elements for $\dot{M}$ = $10^4 M_{\odot}/yr$ and r = 70 km. All of the anomalous elements have been significantly depleted under these conditions, ruling this particular set of parameters out as a production site.

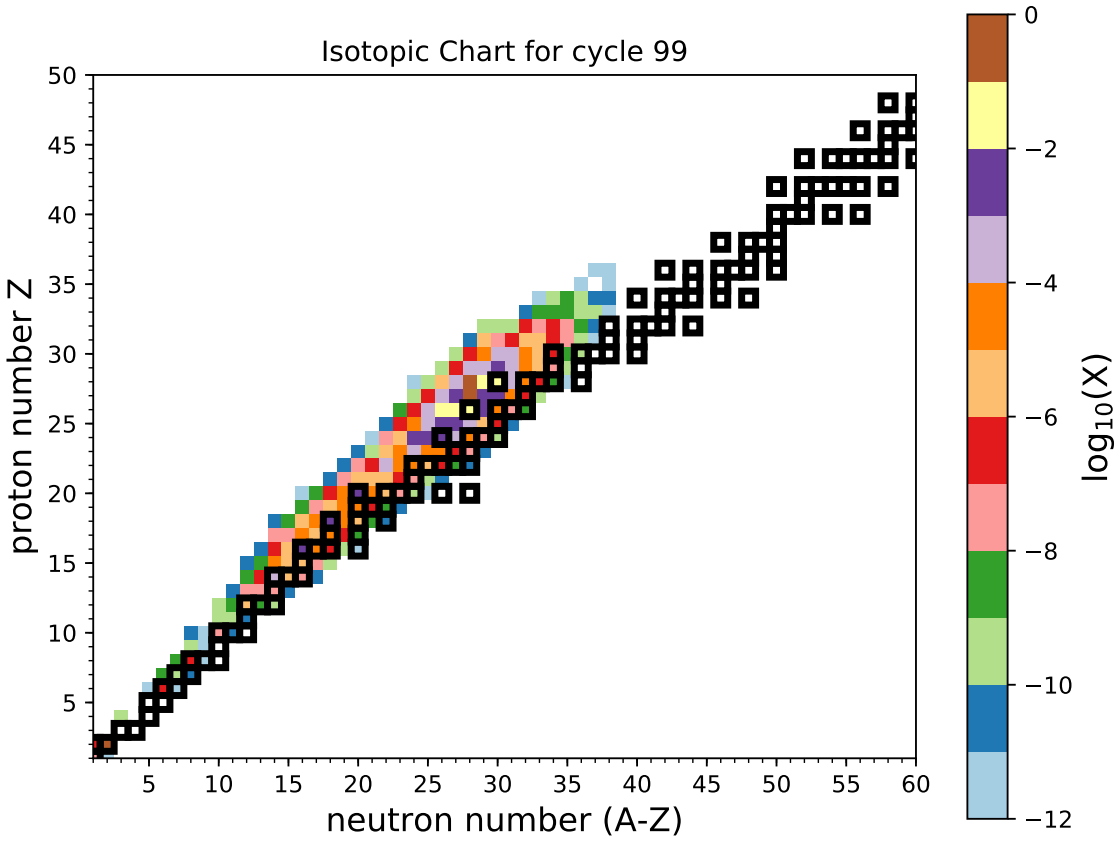

Figure 5.23: Flux at $\dot{M}$ = $10^4 M_{\odot}/yr$ and r = 50 km. Again nucleosynthesis is not as extensive, and seems to be more 'peaked' around the lower mass nuclei (Z≈35 and less).

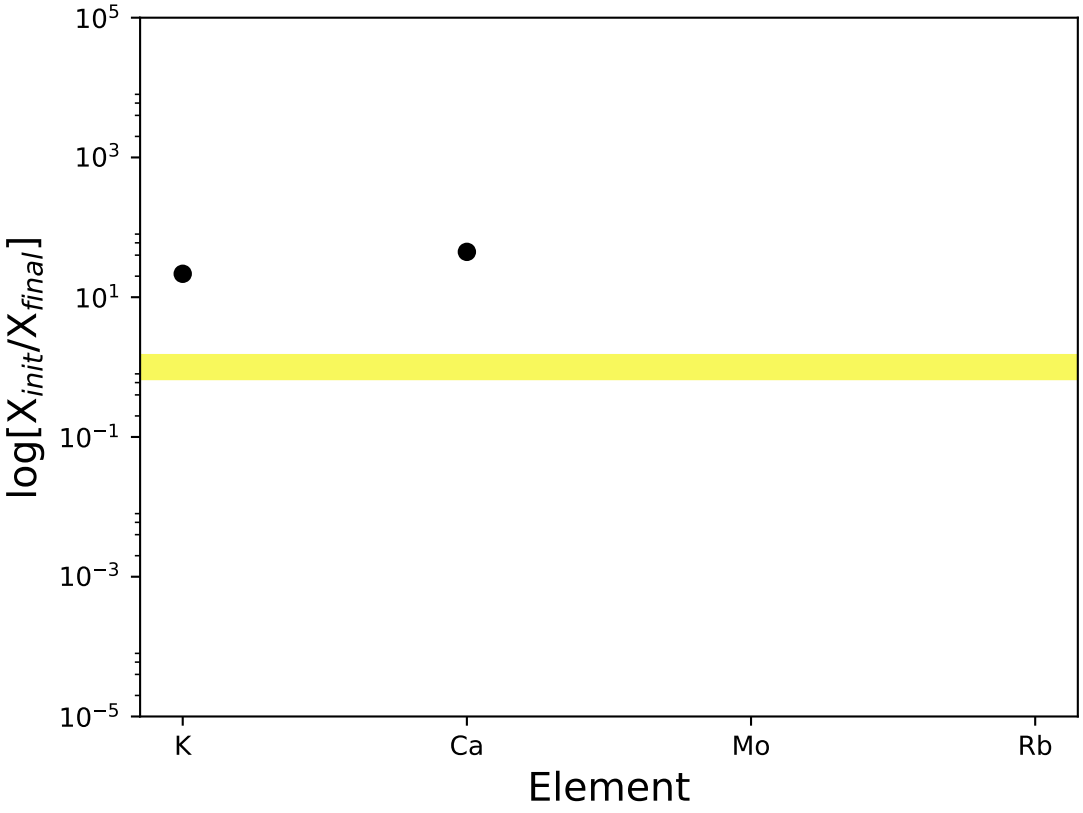

Figure 5.24: Enhancement of K, Ca, Mo and Rb at $\dot{M} = 10^4 M_\odot/yr$ and r = 50 km. K and Ca are enhanced, however Mo and Rb are not, indicating that the higher accretion rate model is more favourable to the production of these elements at r = 50 km.

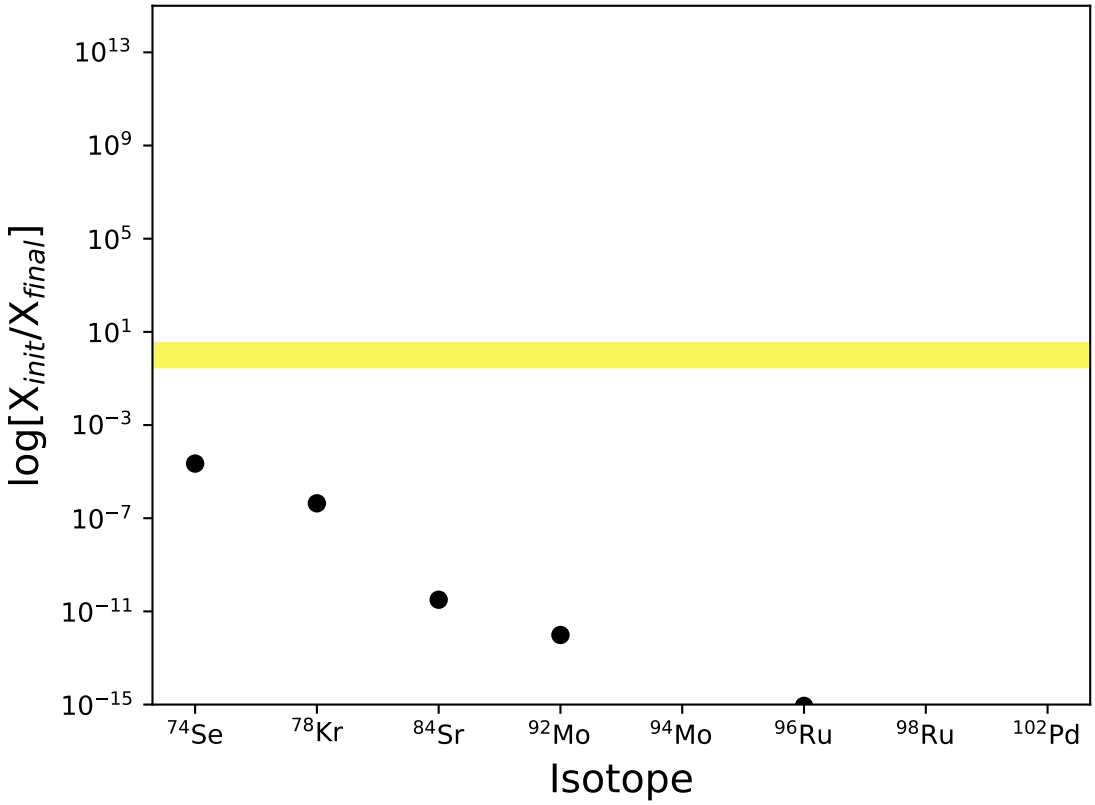

Figure 5.25: Enhancement p nuclei at $\dot{M}$ = $10^4 M_\odot/yr$ and r = 50 km. All of these are severely depleted under these conditions.

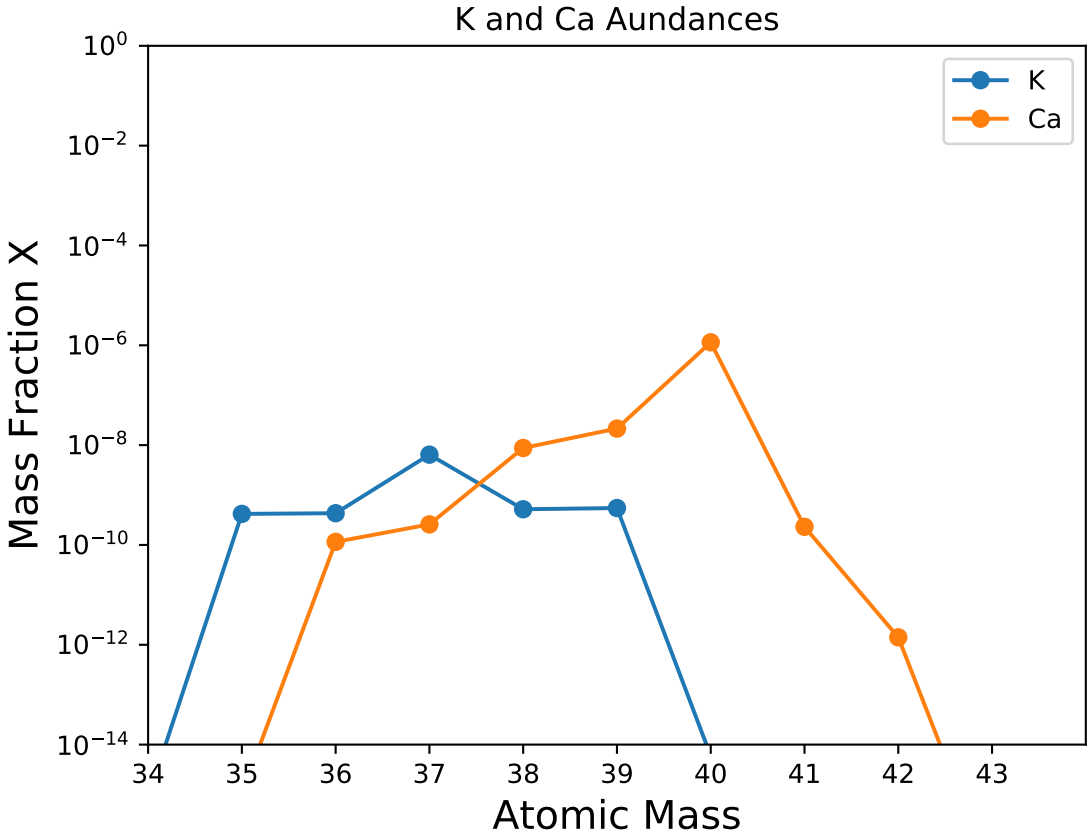

Figure 5.26: K and Ca elements at $\dot{M} = 10^4 M_\odot/yr$ and r = 30 km. The calcium abundance is reduced overall in this scenario, as for the 50 km case.

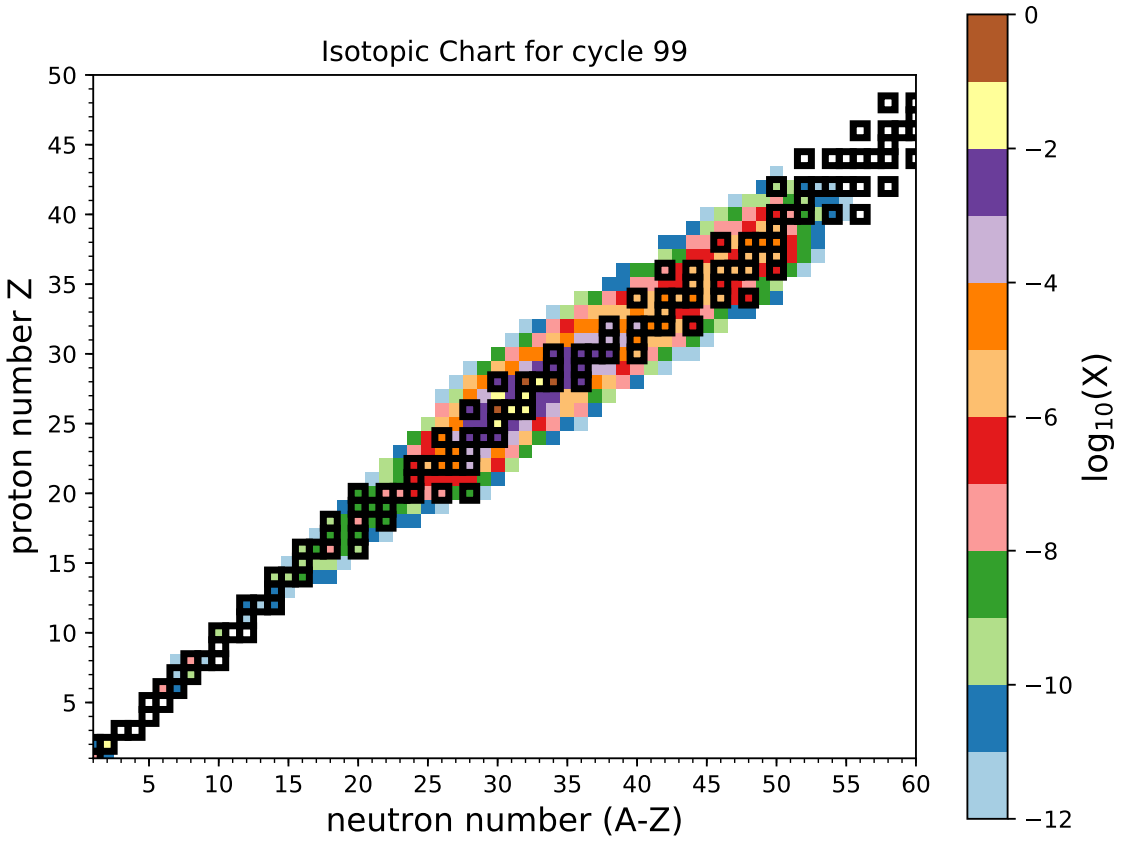

Figure 5.27: Abundance chart at $\dot{M} = 10^4 M_\odot/yr$ and r = 10 km. The distribution of nuclei is roughly symmetric around the line of stability.

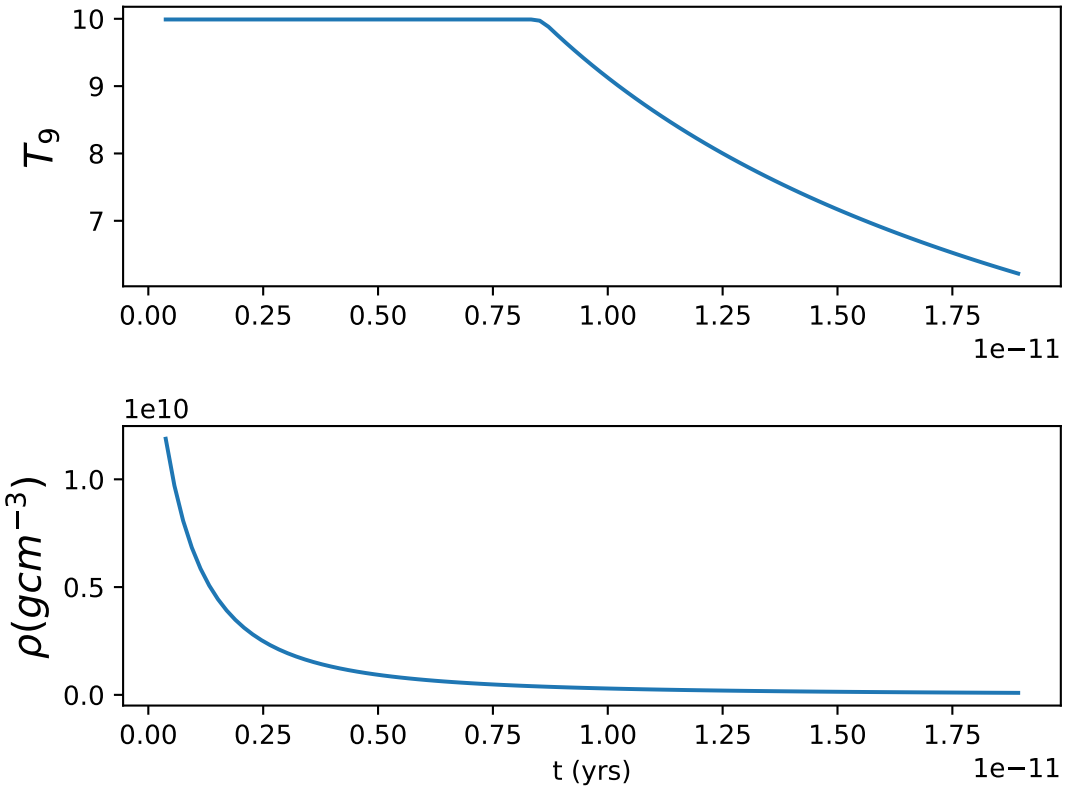

Figure 5.28: Temperature and density profiles at $\dot{M} = 10^4 M_\odot/yr$ and r = 10 km. The difference in these profiles as compared with previous ones shown comes from the different mixing employed at these radii.

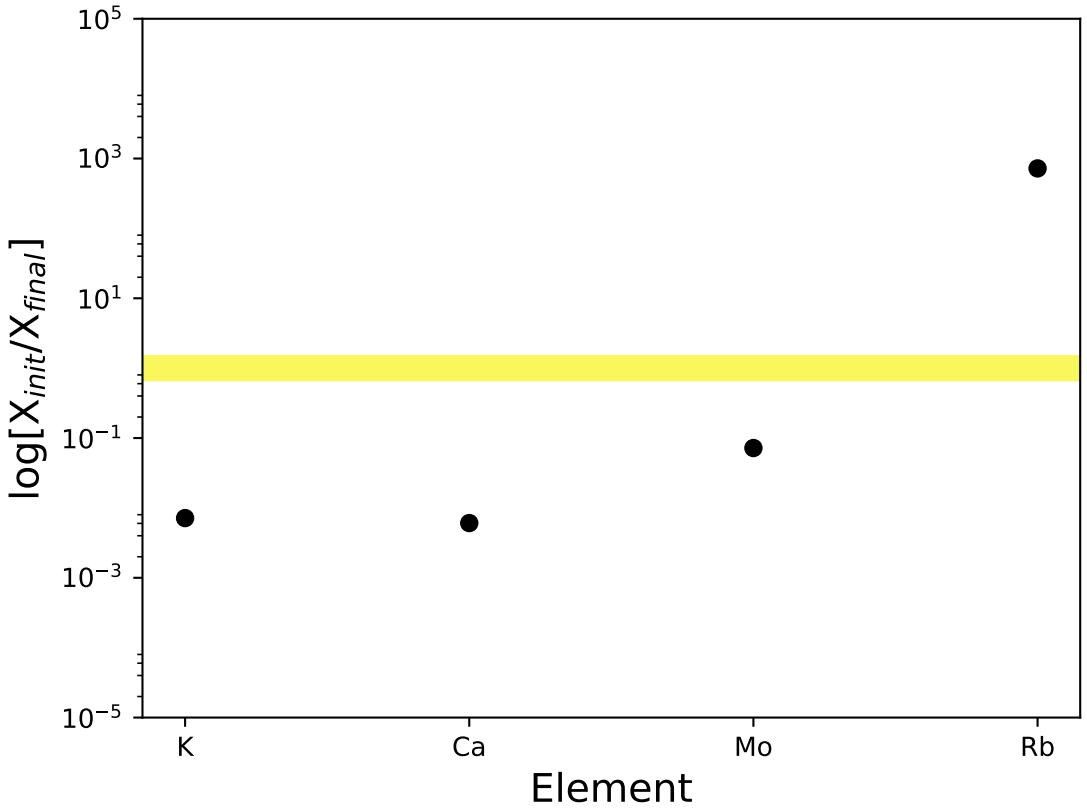

Figure 5.29: Levesque element abundances at $\dot{M} = 10^4 M_\odot/yr$ and r = 10 km. There is an increase in the abundance of Rb, other elements are dramatically depleted however.

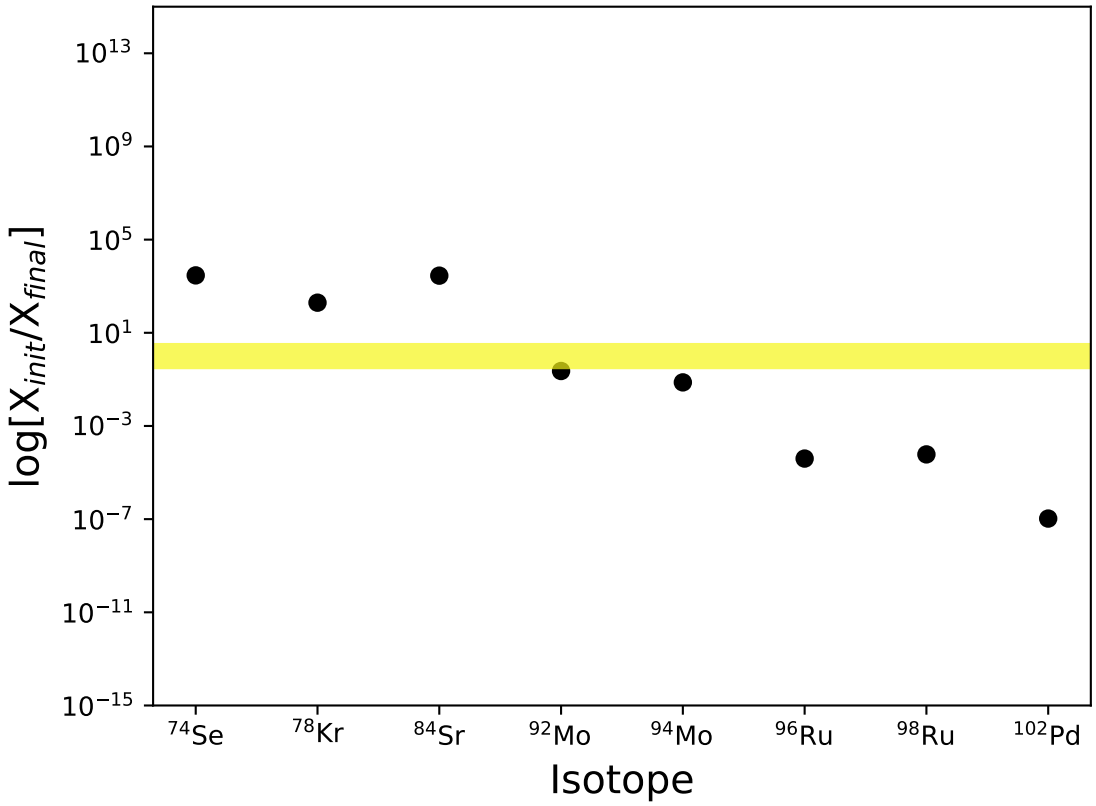

Figure 5.30: p nuclei element abundances at $\dot{M}$ = $10^4 M_\odot/yr$ and r = 10 km. It is interesting to note the increased abundances of ^{74}Se, ^{78}Kr and ^{84}Sr under these conditions however, considering the abundances of K, Ca and Mo, this cannot be responsible for the observed enhancements in the spectrum of HV2112.

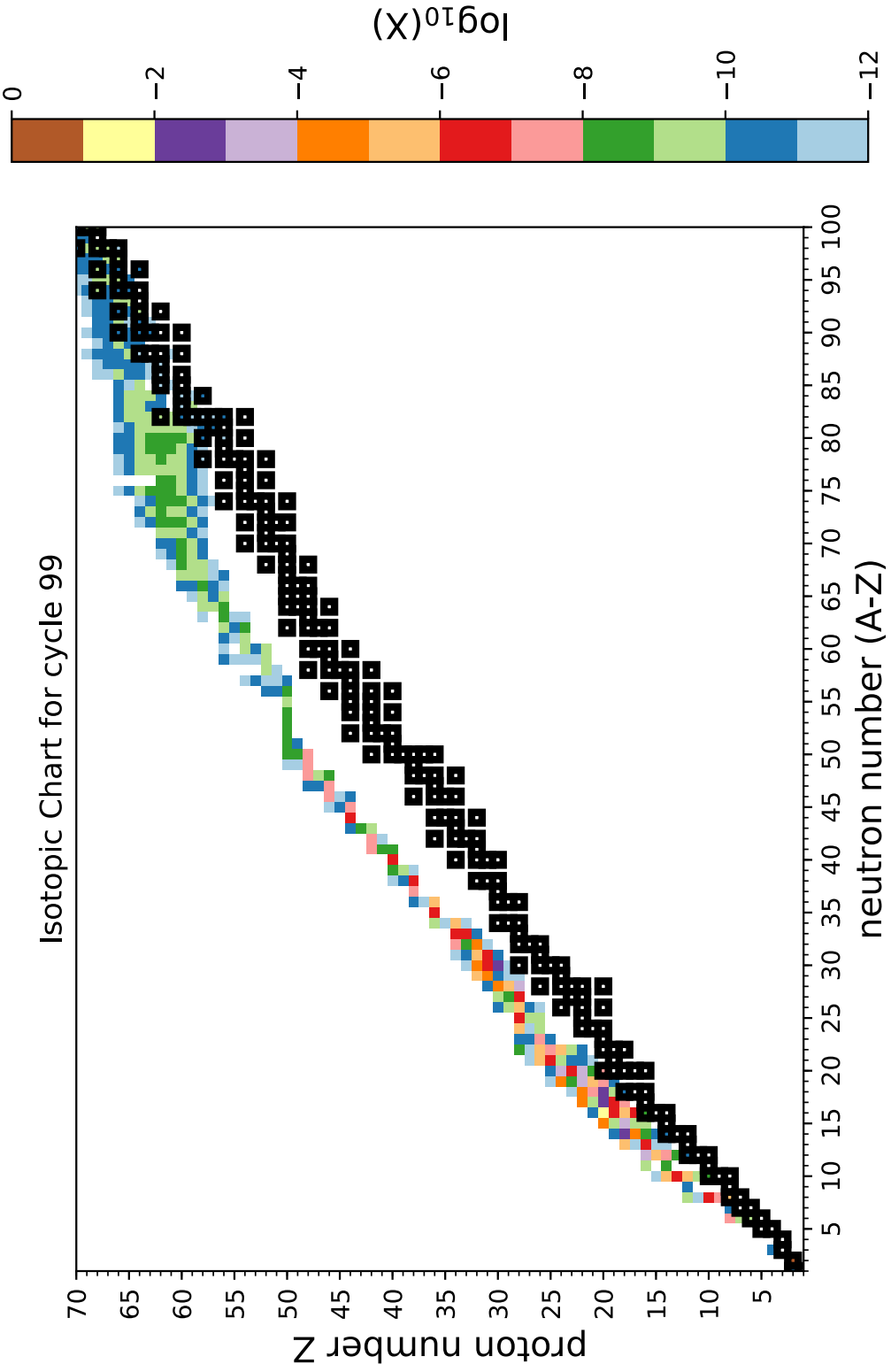

Figure 5.31: Chart showing extent of nucleosynthesis for $\dot{M}$ = $10^3 M_\odot/yr$ and r = 100 km. The extent of nucleosynthesis at this radius goes beyond the limits of the rp-process, likely due to α captures on higher mass isotopes or the presence of high mass seed nuclei in the accreted material which at higher temperatures was destroyed.

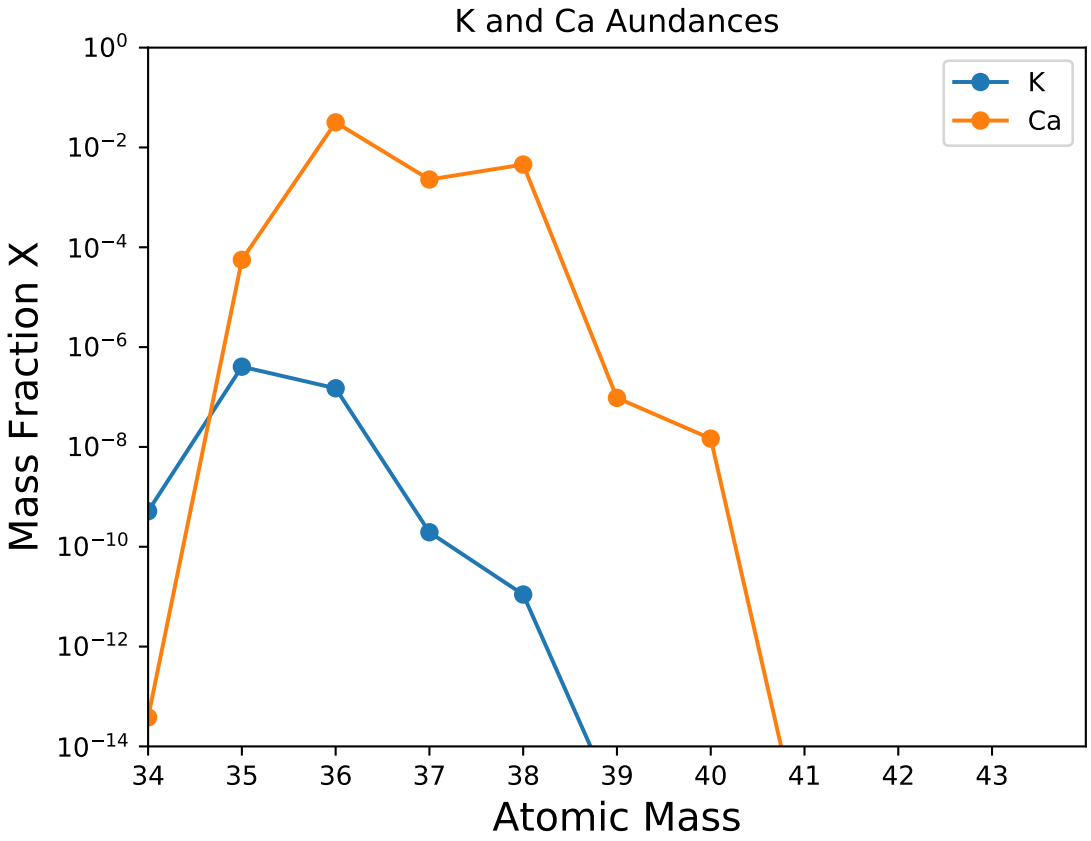

Figure 5.32: Chart showing isotopic abundances of K and Ca for $\dot{M}$ = $10^3 M_{\odot}/yr$ and r = 100 km. A significant increase in the amount of ^{36,38}Ca under these conditions can be observed, this results in an increase in the abundance of Ca in the procesed material of arounnd 10^3 times the initial abundance (see Figure 5.33).

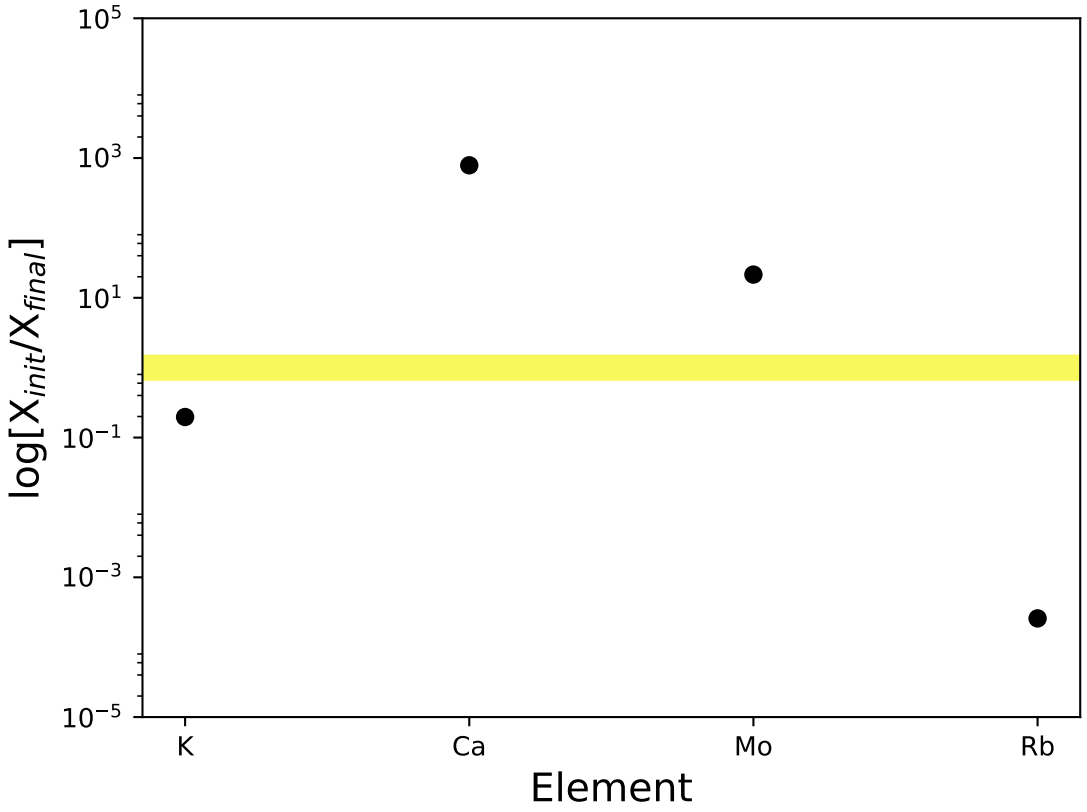

Figure 5.33: Enhancement of isotopic abundances of elements identified in Levesque et al for $\dot{M}$ = $10^3 M_\odot/yr$ and r = 100 km. Ca and Mo are enhanced by a factor of $\approx$ 1000 and 50 respectively.

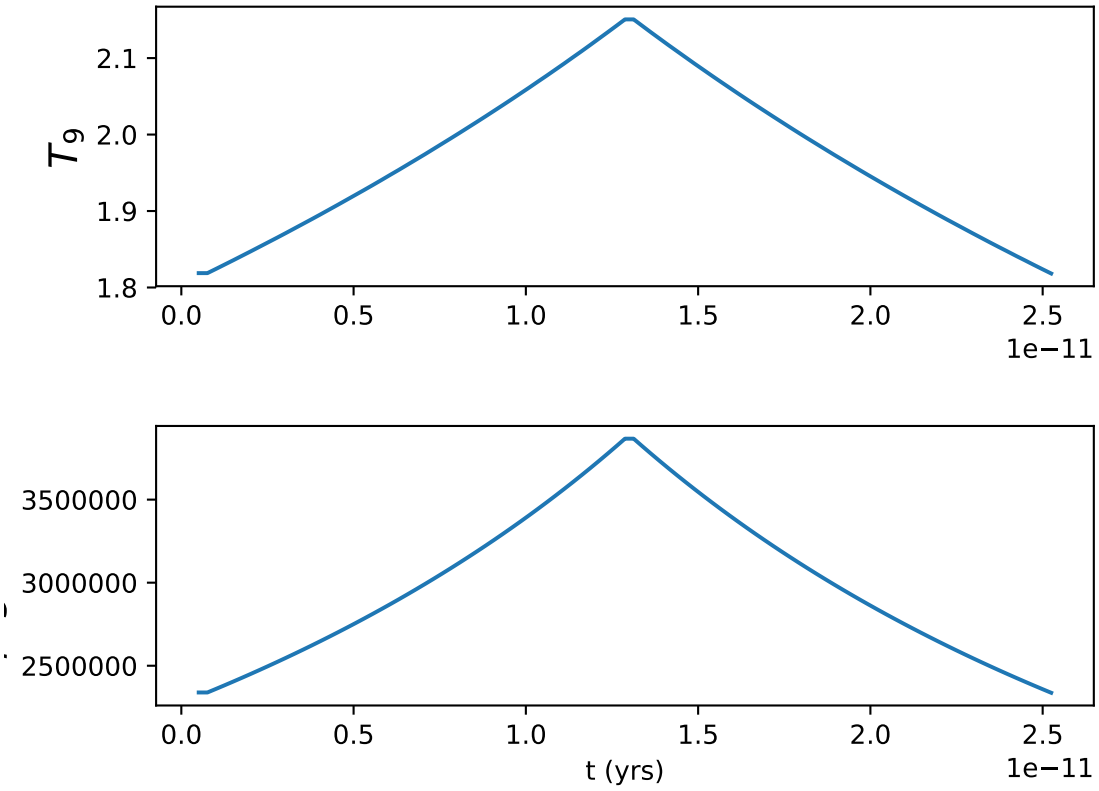

Figure 5.34: Temperature and density profiles for $\dot{M} = 10^3 M_\odot/yr$ and r = 60 km. The less extreme burning conditions at this accretion rate and distance allows heavier material to survive and be processed to still heavier isotopes.

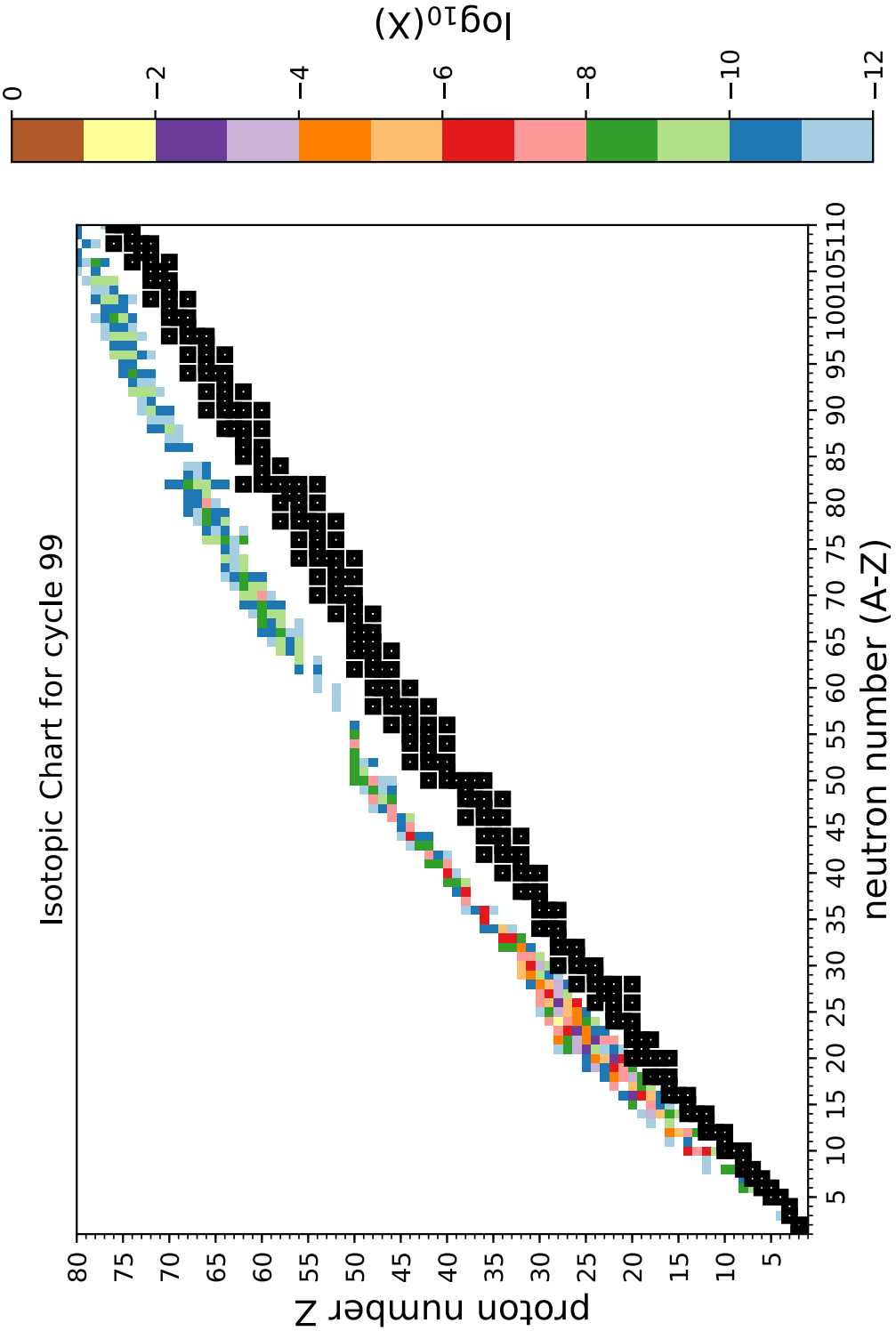

Figure 5.35: Abundance chart showing extent of nucleosynthesis for $\dot{M}$ = $10^3 M_{\odot}/yr$ and r = 80 km. The extent of nucleosynthesis in this plot is the largest of any of the conditions investigated, with material being processed to A ≈190. This is not predicted to occur in the pure rp-process and indicates the action of the αp-process in this system, or proton captures on seed nuclei present above this gap in the initial accreted material.

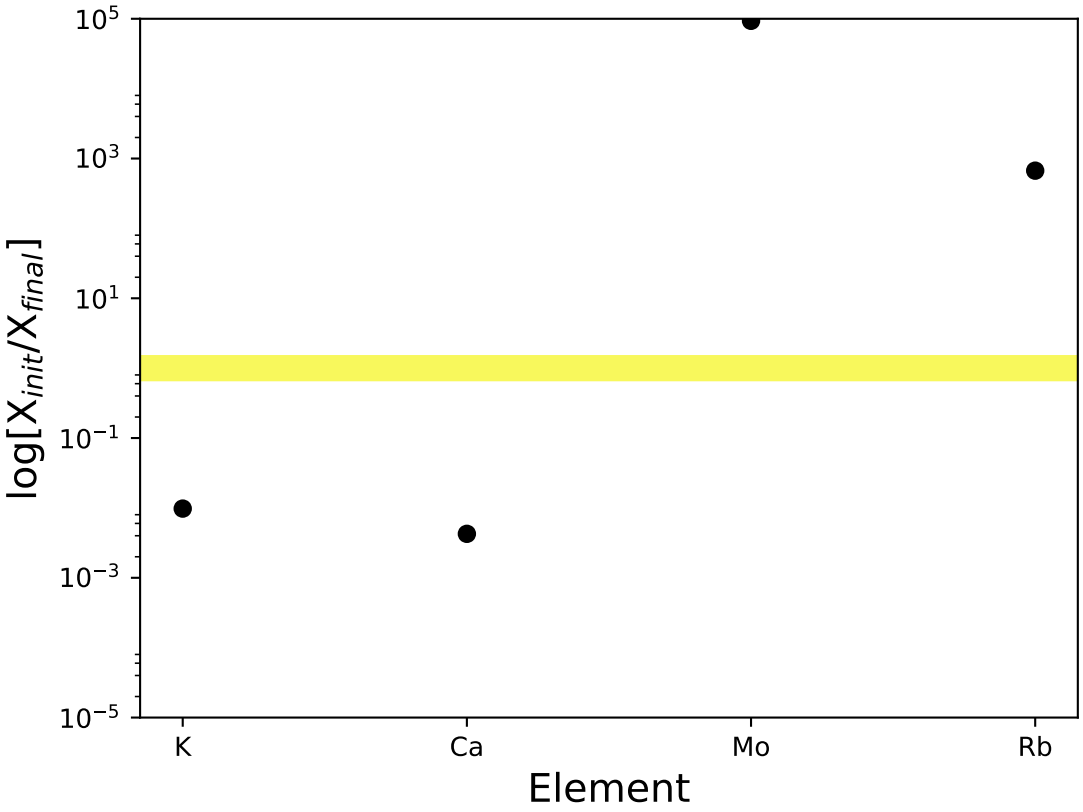

Figure 5.36: Enhancement of K, Ca, Mo and Rb for $\dot{M}$ = $10^3 M_{\odot}/yr$ and r = 40 km. The large overproduction of Mo and Rb is very promising.

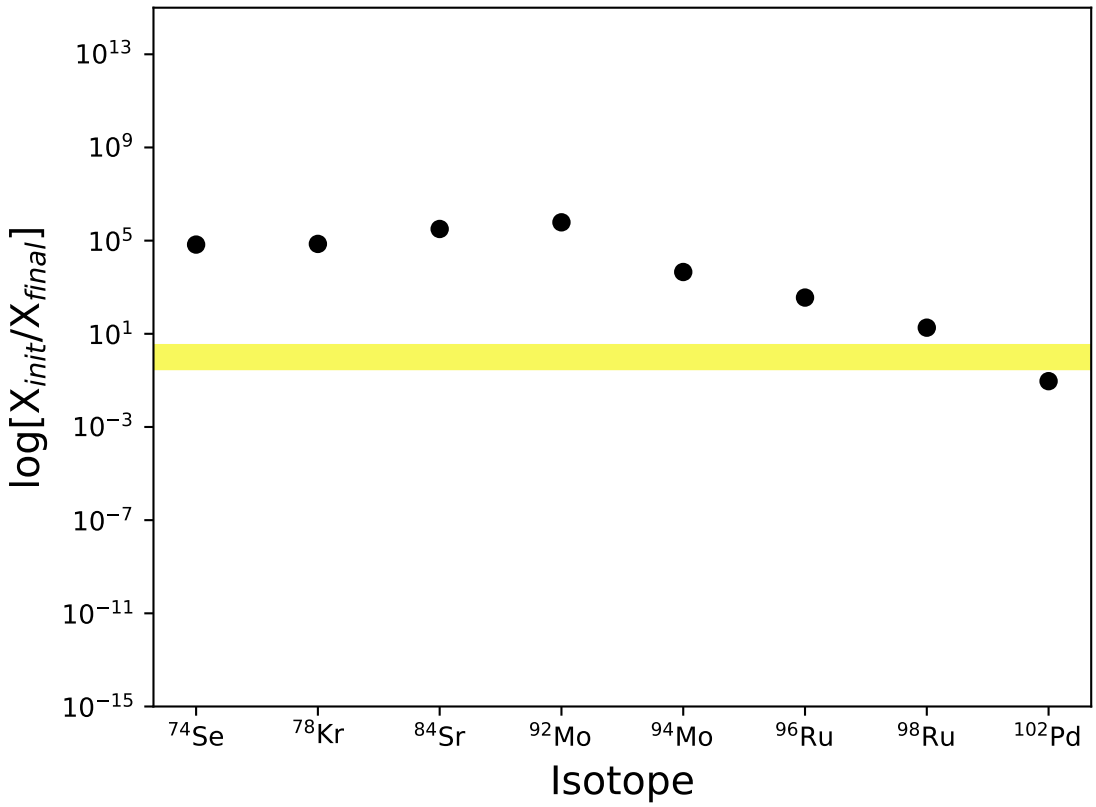

Figure 5.37: Enhancement of p nuclei for $\dot{M}$ = $10^3 M_\odot/yr$ and r = 40 km. ^{74}Se, ^{78}Kr, ^{84}Sr, ^{92}Mo, ^{94}Mo, ^{96}Rb and ^{98}Rb are all significantly enhanced in this regime, and may present possible observational candidates for future work with HV2112.

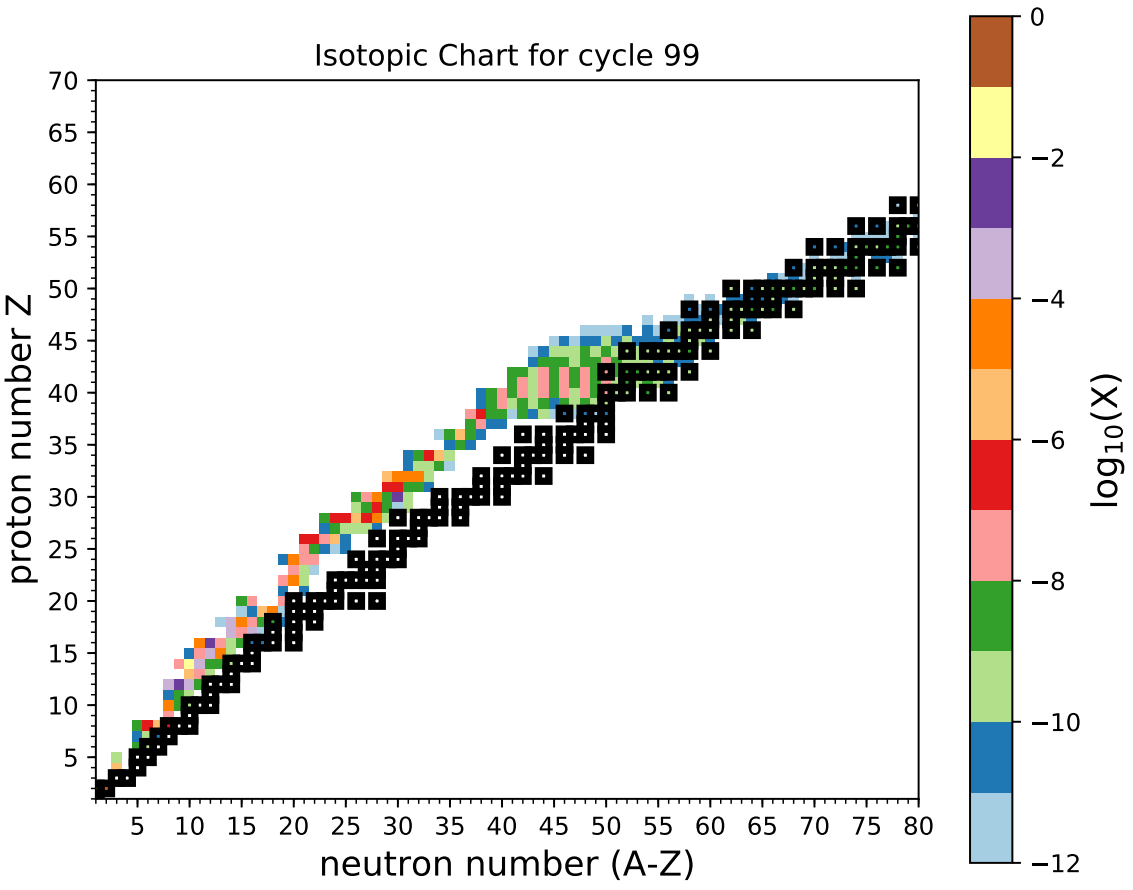

Figure 5.38: Abundance chart for $\dot{M} = 10^2 M_{\odot}/yr$ and r = 100 km. Nuclear reactions do not drive the flow significantly to higher masses at these temperatures, but act to push the material towards more proton rich isotopes.

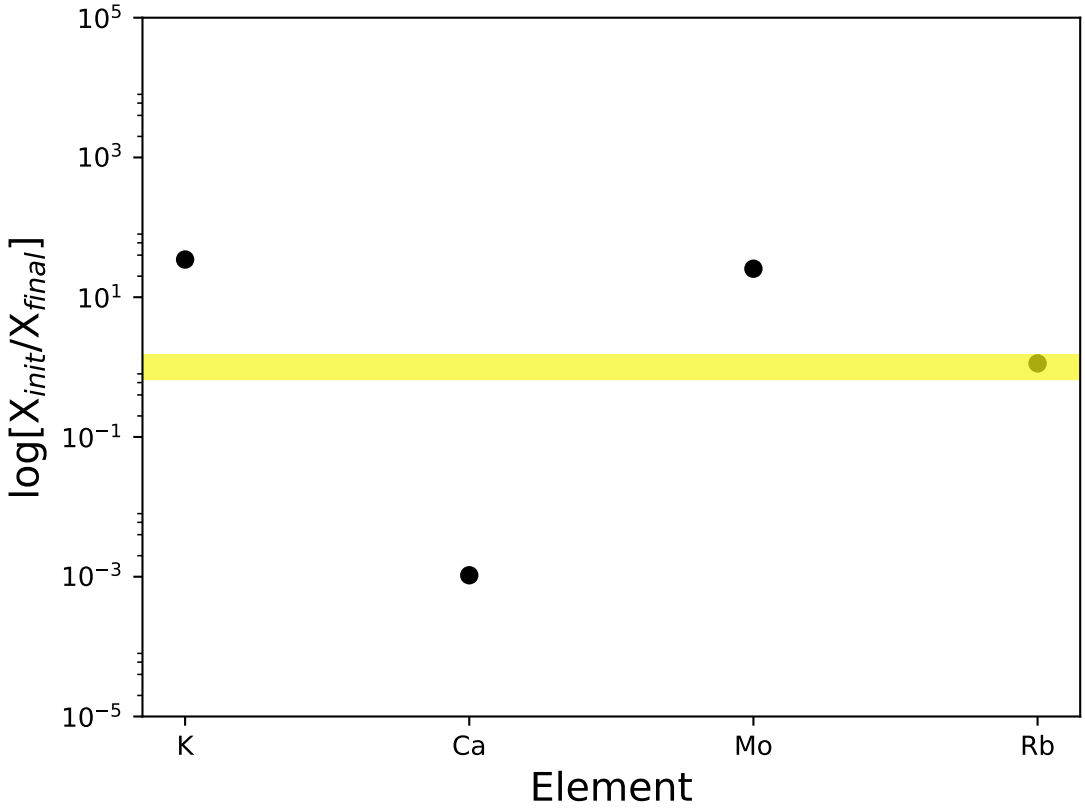

Figure 5.39: Levesque element enhancements for $\dot{M}$ = $10^2 M_{\odot}/yr$ and r = 100 km. K and Mo are significantly enhanced in these conditions, both are enriched in the material by around 30x their initial abundance.

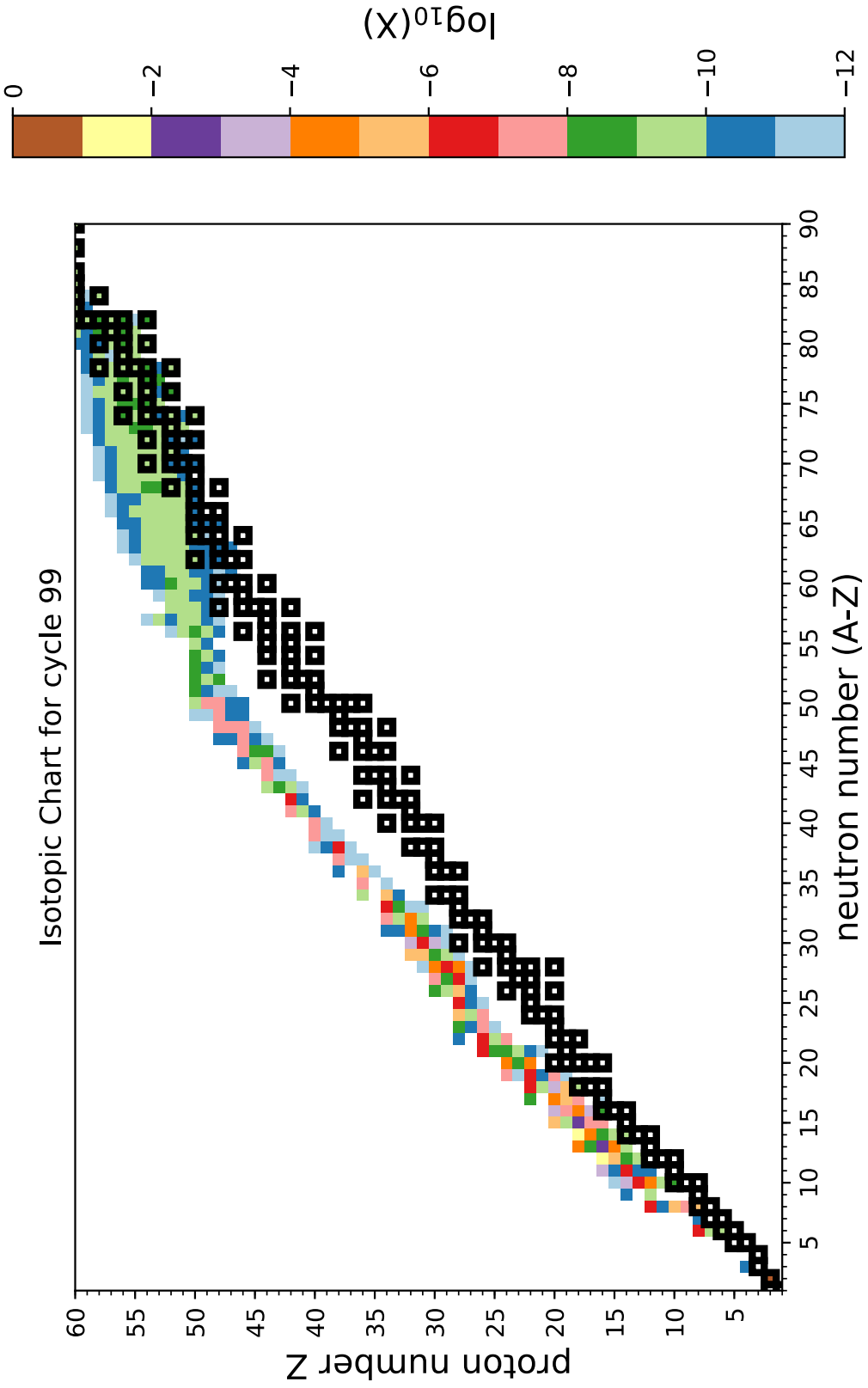

Figure 5.40: Abundance chart for Ṁ = $10^2 M_\odot/yr$ and r = 80 km. Nuclei are produced up to A≈130.

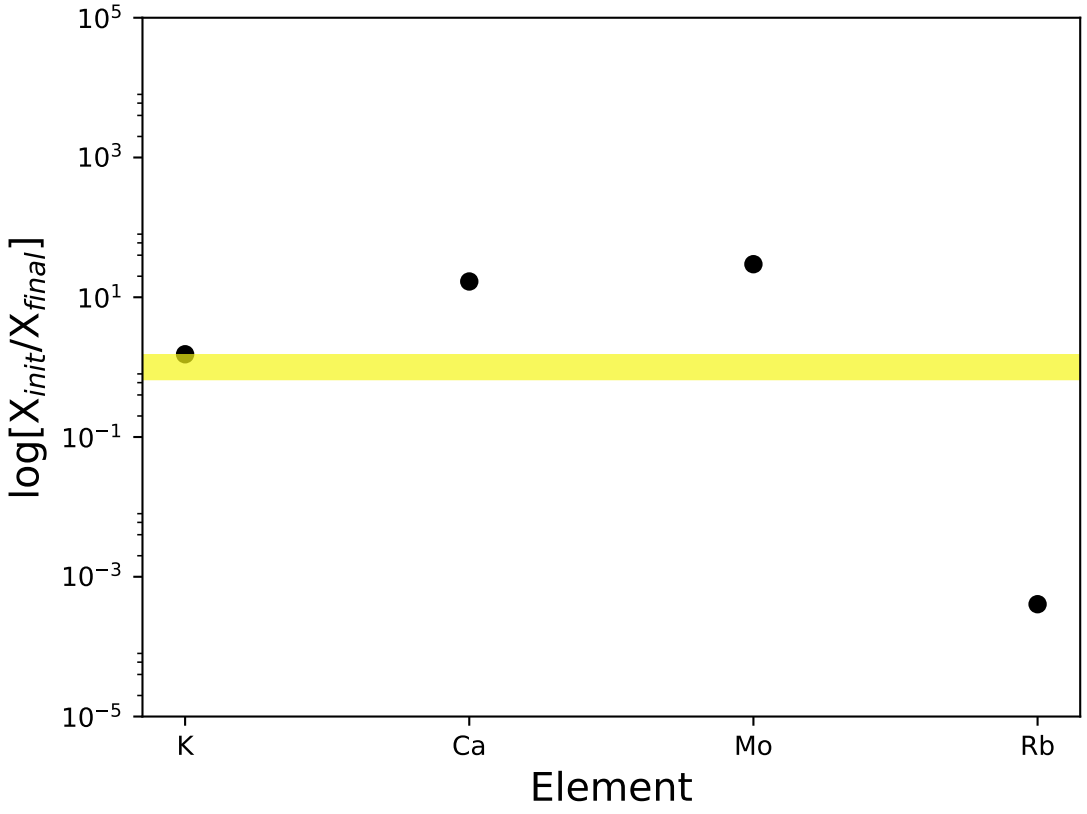

Figure 5.41: Enhancements in abundances of K, Ca, Mo and Rb for $\dot{M} = 10^2 M_{\odot}/yr$ and r = 80 km. Only Rb is depleted under these conditions, with significant enhancements of the Ca and Mo of around 30x their initial abundances, and an increase in K of 2-3x it's initial abundance.

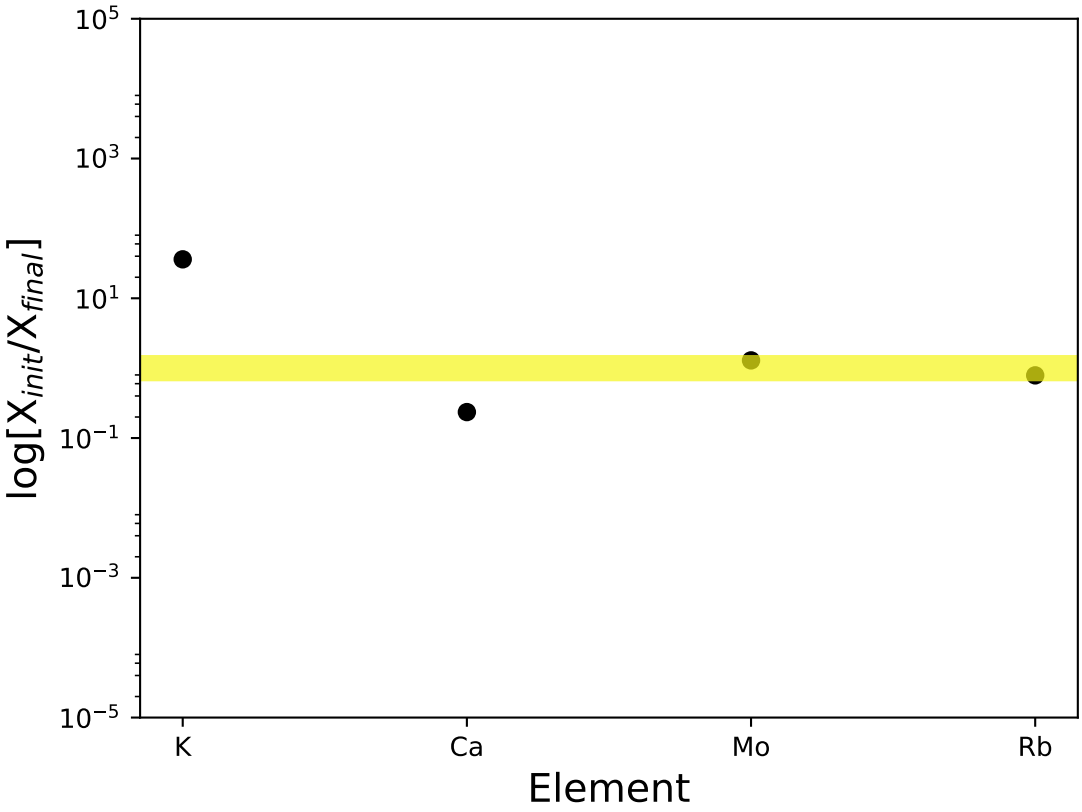

Figure 5.42: Enhancements in abundances of K, Ca, Mo and Rb for $\dot{M}$ = $10 M_{\odot}/yr$ and r = 100 km. K is enhanced under these conditions whilst Ca is depleted.

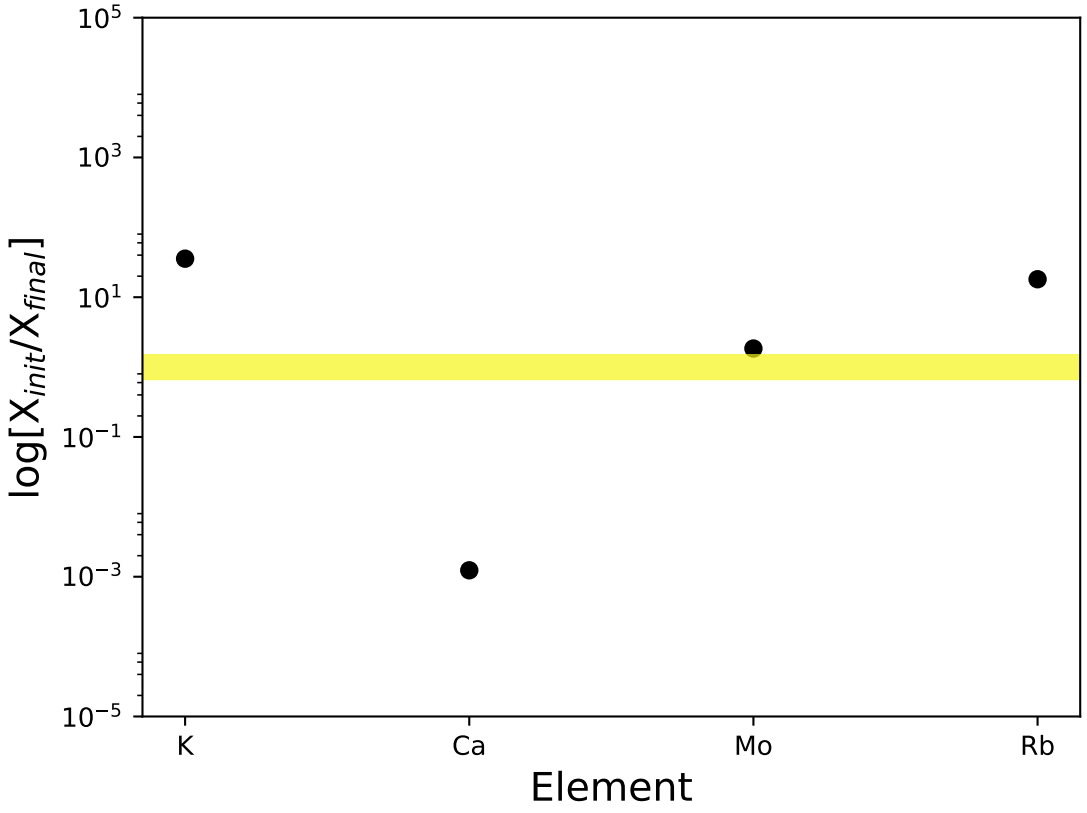

Figure 5.43: Enhancements in abundances of K, Ca, Mo and Rb for $\dot{M}$ = $10 M_{\odot}/yr$ and r = 80 km. Again Ca is destroyed at this accretion rate although K, Mo and Rb are all enhanced by factors of $\approx$ 30, 2 and 20 respectively.

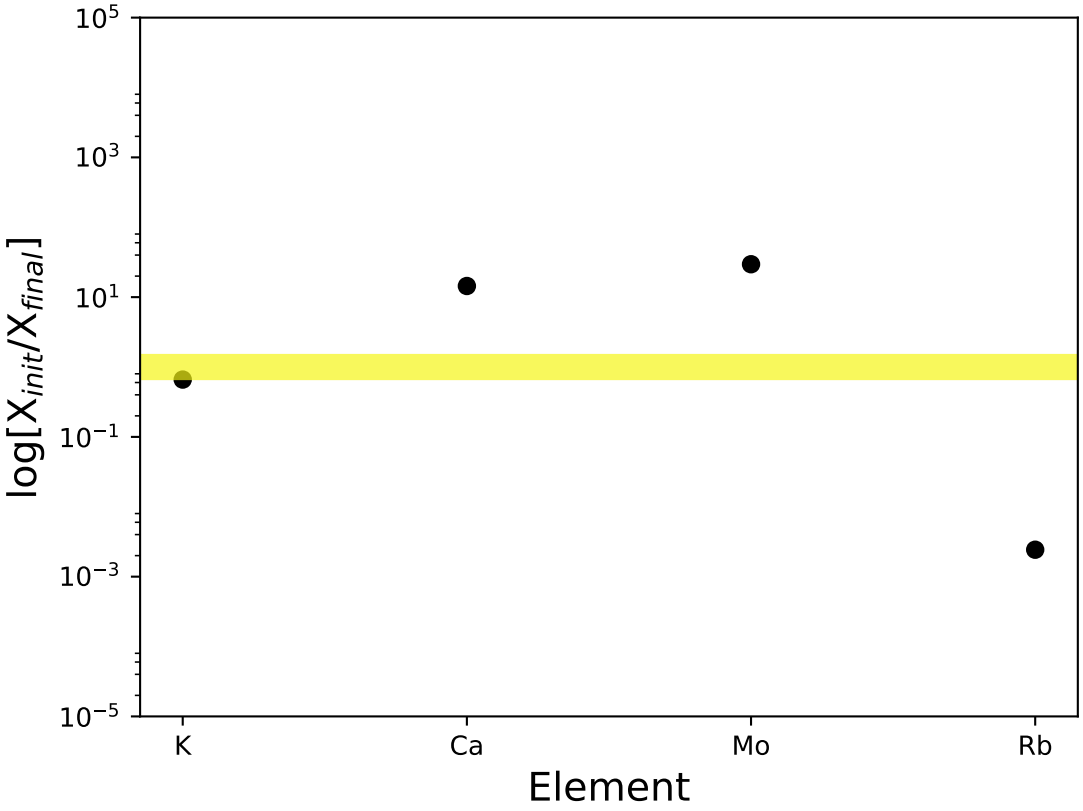

Figure 5.44: Enhancements in abundances of K, Ca, Mo and Rb for $\dot{M}$ = $10 M_{\odot}/yr$ and r = 60 km. Ca is here enhanced by a factor of $\approx$ 30, as is Mo. Rb is severly depleted by a factor of 10^{-3} and K by a factor of 2-3. Contributions at this accretion rate from the r = 80 km and r = 60 km casses may be able to account for the observed enrichments in the spectrum of HV2112.

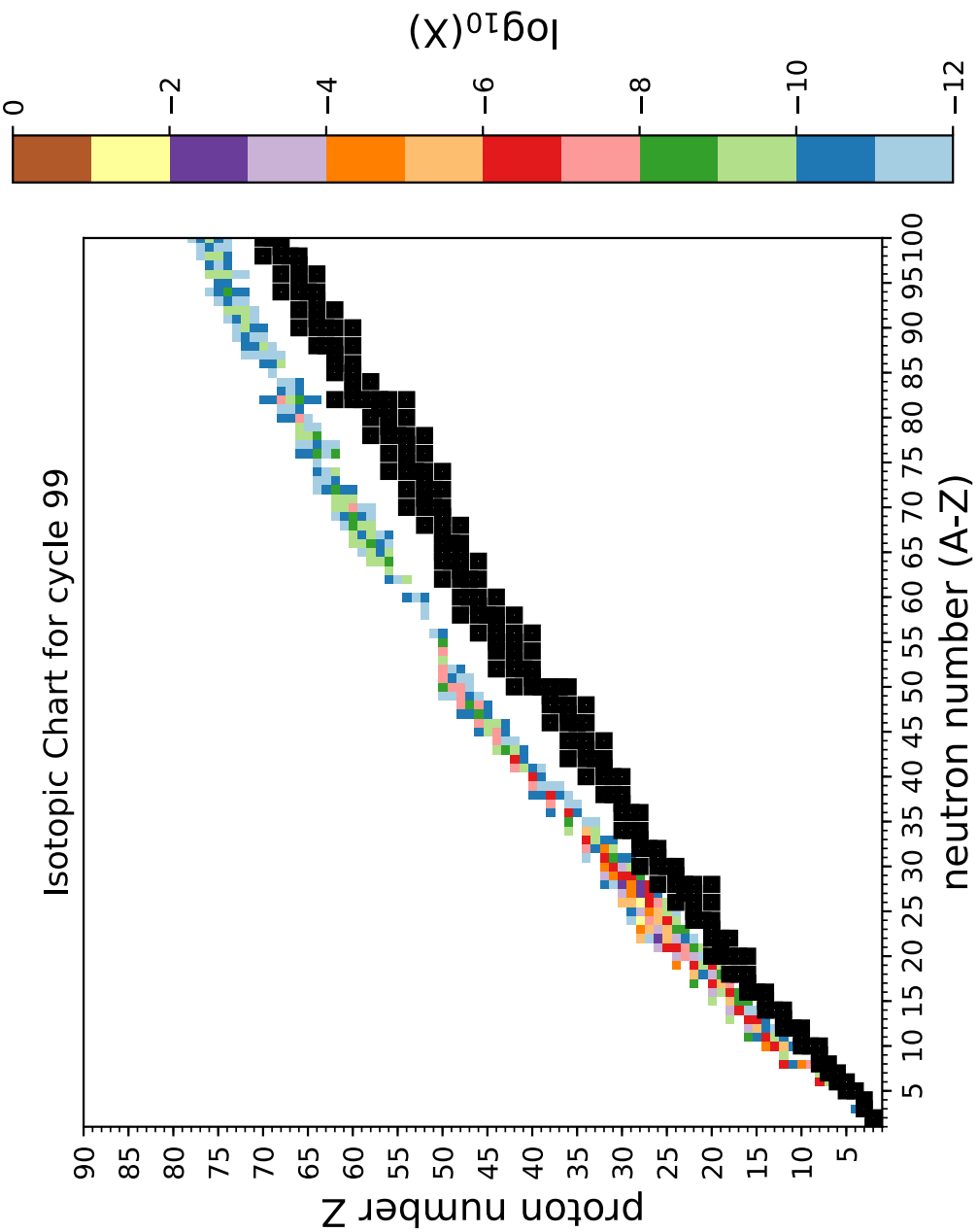

Figure 5.45: Abundance chart showing the extent of nuclesoynthesis for $\dot{M} = 10 M_{\odot}/yr$ and r = 60 km. material with A > 170 are produced, although with relatively low mass fractions.

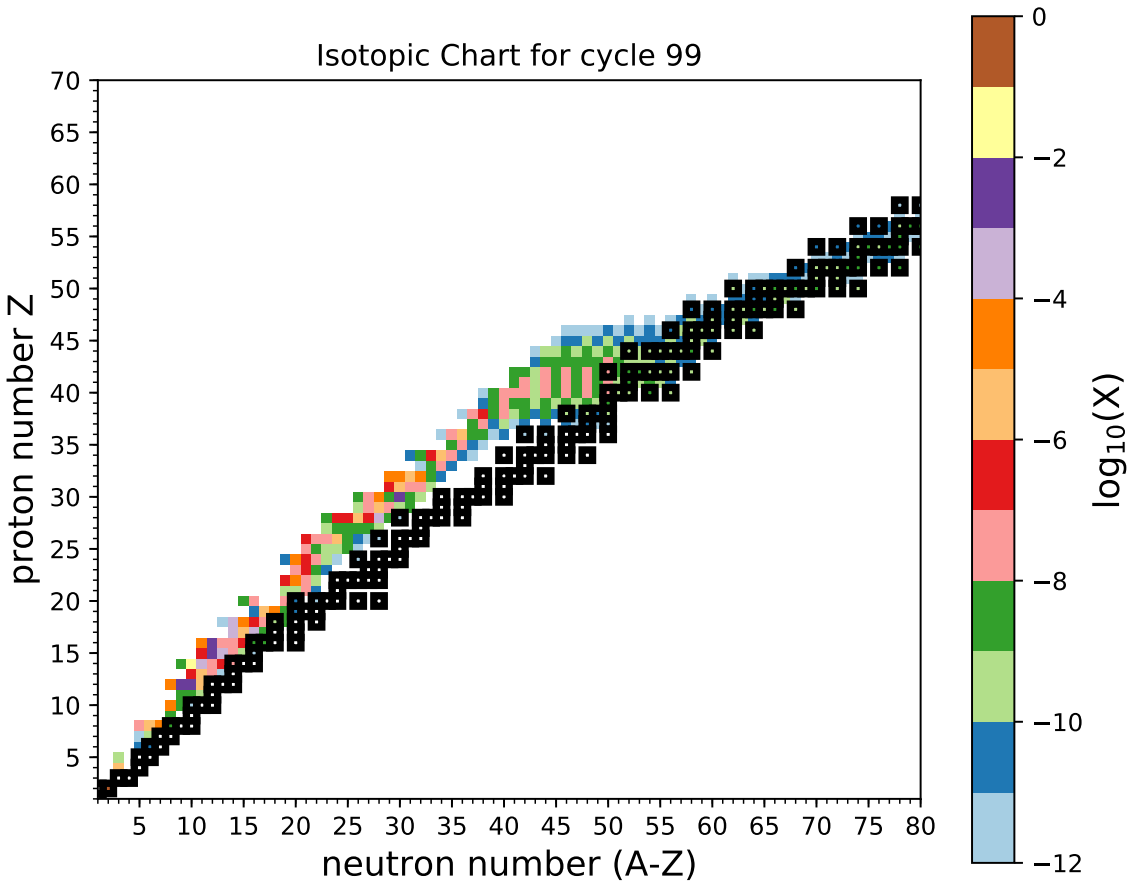

Figure 5.46: Abundance chart showing the extent of nuclesoynthesis for $\dot{M}$ = $10 M_{\odot}/yr$ and r = 40 km. The abundances of heavier elements are not significantly changed from the initial conditions to the relatively mild Temperature conditions at this accretion rate.

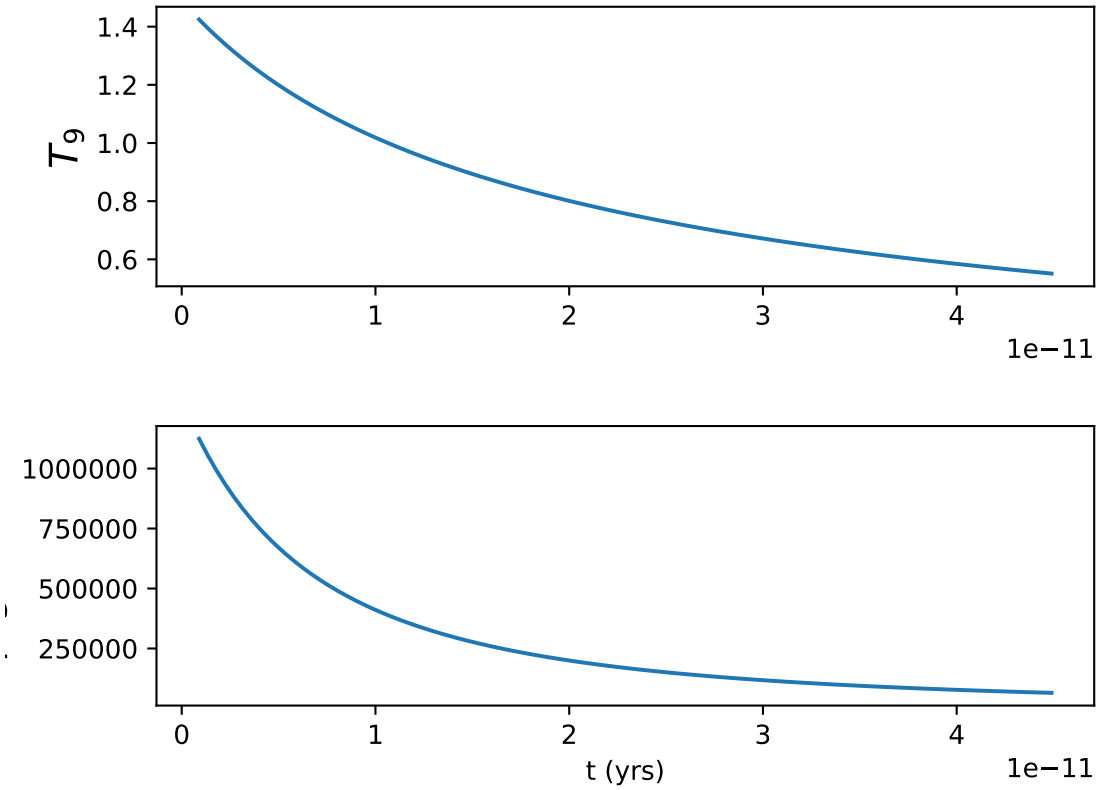

Figure 5.47: Temperature and density profiles for $\dot{M}$ = $10 M_{\odot}/yr$ and r = 40 km. Material reaches a temperature of T_9 = 1.4 under these conditions

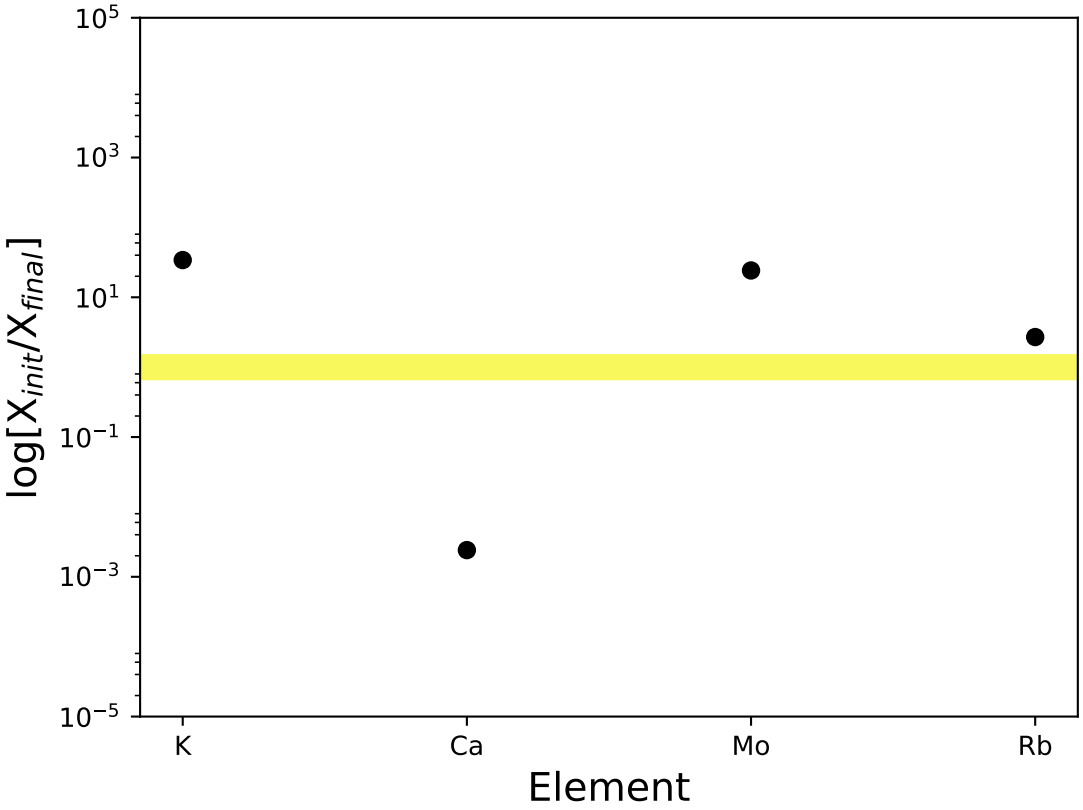

Figure 5.48: Enhancements of elements K, Ca, Mo and Rb for $\dot{M}$ = $10 M_{\odot}/yr$ and r = 40 km. K, Mo and Rb are enhanced under these conditions.

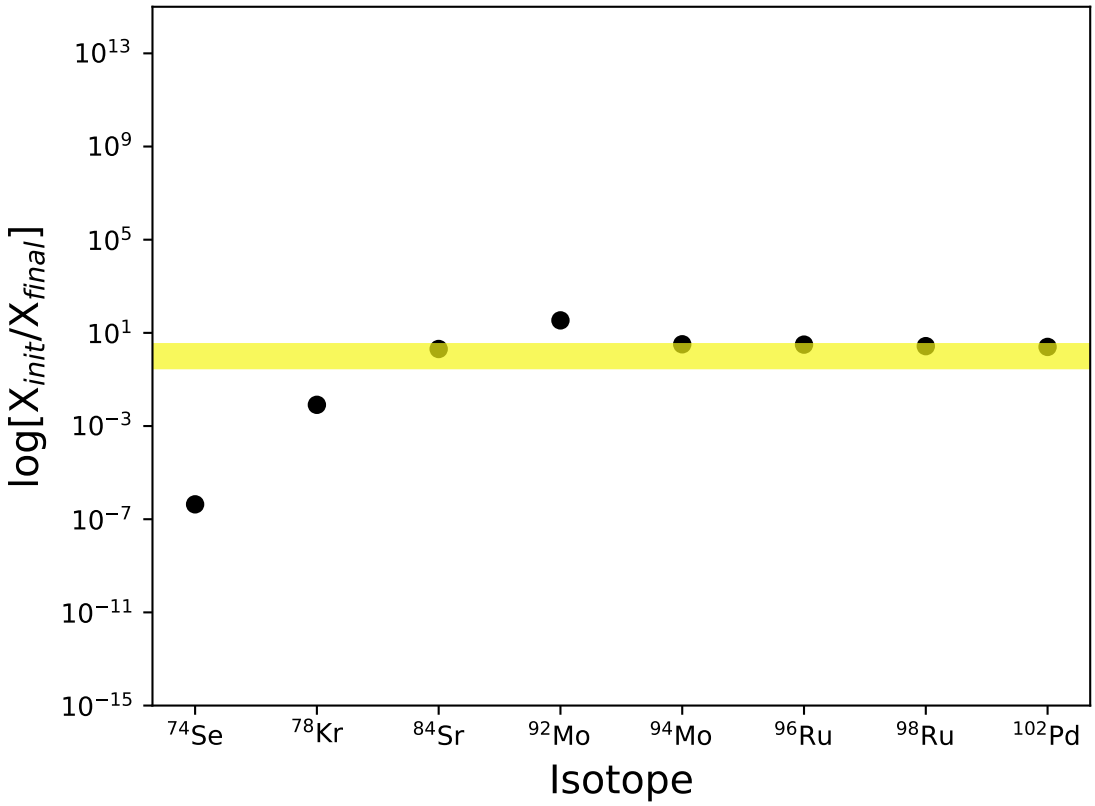

Figure 5.49: Enhancements of p nuclei for $\dot{M}$ = $10 M_{\odot}/yr$ and r = 40 km. Only ^{92}Mo has been enriched by in any significant way.

Chapter 6

Conclusion

It can be clearly seen from the results of the simulations that a significant enhancement of the elements highlighted in the work of Levesque et al can be reproduced in this system, for a wide range of accretion rates and depths, even without considering further parameters such as mixing in the system and reprocessing of burned material.

Material accreted at $\dot{\text{M}} = 10^5 M_\odot/yr$ at r = 50 km (Figure 5.12) shows an enhancement in all of the elements identified as being enhanced in the spectrum of HV2112. Although this will be the shortest lived accretion regime, as the neutron star begins to interact with the core of the companion star, it is encouraging that all of the elements observed to be enhanced in the spectrum of HV2112 can be produced under the same burning conditions, and at an accretion rate of $10^5 M_\odot/yr$, as each cycle in the model investigated here lasts $\approx 10^{-11}$yrs, around $10^{-6} M_\odot$ of processed material will be produced per cycle. As around 15% of this material can be ejected to enrich the envelope of the companion star 3000 cycles, a total time of $\approx$ 10 s, would release around $10^{-4} M_\odot$ of enriched material into the companion star's envelope. Quantifying the amount of material needed to reproduce the observed spectrum in HV2112 is beyond the scope of this work however it is clear that a significant mass of material can be processed. A full investigation into the stability of the system under these conditions and it's expected lifetime would be necessary to confirm that this is possible however.

This regime has some difficulties associated with it - by the time the neutron star has sunk so far into

the companion, will the companion star's envelope has been ejected? The problem of the stability of the system under such extreme conditions has been mentioned above, and diverse other effects such as neutrino interactions in the dense accreting medium changing the nuclear reaction pathways, the artificial limiting of the temperature to T_9 = 10, and the effect of being ejected completely from the NS are not addressed in this project. Happily, many other less extreme burning conditions reproduce enhancements in one or more of K, Ca, Mo and Rb.

At an accretion rate $\dot{M} = 10^4 M_\odot/yr$, K and Ca are overproduced at r = 50 km (Figure 5.24) by factors of $\approx$ 20 and 30 respectively, whilst at r = 100 km for the same accretion rate, Mo is similarly overproduced (Figure 5.17) and at r = 10 km, Rb is significantly enhanced by a factor of $>10^3$. If material is ejected from different heights above the surface of the neutron star, then it is possible that material is differently processed at these different heights and then mixed in the envelope of the companion star, giving rise to the observed over-abundances.

For an accretion rate of $\dot{M} = 10^3 M_\odot/yr$ we see the largest enhancement in any regime - at r = 40 km, the mass fraction of Mo is 10^5 times larger than in the unprocessed material, as well as Rb being enhanced by a factor of 10^3 (Figure 5.36), these conditions also resulted in a significant increase in the abundances of 7 p nuclei, unique in the runs investigated here (Figure 5.37). This introduces the possibility of an observational candidate to discriminate between different burning conditions in HV2112. Ca is also significantly enhanced at this accretion rate at larger radii. At r = 100 km, Ca is enhanced by a factor of 10^3 (Figure 5.33). Unfortunately, no radius for the $\dot{M} = 10^3 M_\odot/yr$ accretion rate appears to increase the fraction of K in the processed material, however it is not expected that the NS would only experience one rate of accretion through the lifetime of the system and so it is perhaps not surprising that different contributions may come from different accretion rates.

$\dot{M} = 10^2 M_\odot/yr$ shows increases in the abundances of K and Mo (Figure 5.39) of 20-30x initial abundance at r = 100 km and Ca and Mo with approximately the same enhancement for r = 80 km (Figure 5.41). Again, whilst this accretion rate cannot account for all observed enhancements in HV2112, it complements the results at other accretion rates.

Perhaps the most surprising result is that for the $\dot{M} = 10 M_{\odot}/yr$ regime. Here we see that K, Ca, Mo and Rb can be produced at the same accretion rate, as was the case for $\dot{M} = 10^5 M_{\odot}/yr$, if material can be ejected from different heights above the surface of the neutron star. K is produced at r = 100 km (Figure 5.42) , K, Mo and Rb at r = 80 km (Figure 5.43) and Ca and Mo at r = 60 km (Figure 5.44) all with an increase in their mass fractions of around 20 - 30 times their initial mass fractions, apart from Mo at r = 80 km which increases only by a factor of 2-3. Although the accretion rates are much lower than for the $\dot{M} = 10^5 M_{\odot}/yr$ case, because this regime is likely to be encountered in the early stages of the common envelope system, it is likely that this stage would last the longest and that more material could be processed at this accretion rate because of this. Again, a full hydrodynamics model of the system would be required to say with any certainty which of these burning regimes would contribute the most to ejected material in the envelope of the companion star.

Temperatures of approximately $T_9 = 3$ result in the production of the heaviest isotopes, who's masses exceed A=130. These therefore must be produced, at least partly, through α captures. This would allow some of the waiting-points to be bypassed in some cases, and so allow the production of these on the short time-scales seen in these simulations. In other cases the high flux of neutrinos would produce free neutrons which would provide alternative paths for the waiting-point nuclei to be bypassed.

Discrimination between burning regimes in the system may be achievable through analysing a broader range of emission lines, and comparing these to the observed extent of nucleosynthesis in the various burning regimes. For example, if heavier elements with Z > 50 are observed in the emission of HV2112, from the results presented here (for example, Figures 5.3, 5.35 etc.), it could be concluded that the milder conditions of low accretion rates and larger distances from the surface of the neutron star are the dominant conditions in the system. In order to make quantitative predictions of this nature however it would clearly be necessary to fully understand the motion of accreted and ejected material, initial abundances for the system and other quantities of the system.

Whilst accretion rates are extraordinarily high in some of these cases, because the burning takes place so quickly, the mass of material accreted onto the neutron star need only be a few thousandths of a solar

mass. In this case, the system may stay stable over many burning cycles, even when mass accretion is at it's maximum.

As the neutron star will be stable for approximately 1 year as it spirals into the red super giant, this system provides all the necessary conditions for the production of large quantities of proton rich nuclei, and a mechanism for their ejection and subsequent enrichment of the interstellar medium. After this time it is expected that the companion star's envelope will be fully ejected, leaving behind the neutron star and the core of the companion, this is caused by the motion of the neutron star through the envelope, ejecting material as it passes. It can be seen from figure **??** that the passage of a neutron star through a dense material can cause significant turbulent effects in that medium, and so it is unsurprising that material from the envolope of the companion star might be ejected due to the passage of the compact object. If the LIGO detector detects coalescing neutron star pairs, then this phenomenon must have occurred during the lifetimes of those systems. In conclusion, the presented simulations suggest that these common envelope systems may be the origin for at least some of the abundance of proton rich material observed in our solar system and that with further research the yields and expected spectral features of these environments may inform a number of astrophysical and nuclear considerations. Alternatively, a true TŻO object could be formed, with the neutron star merging with the core of the RSG, which may stay stable for a further $\approx$ 100 years, this would allow the enriched envelope from the transient system to remain observable for a time. The actual fate of the neutron star must be investigated using hydrodynamical models before any concrete conclusions about the fate of the system can be reached.

To fully quantify the abundances of elements produced in this model, it would also be necessary to follow the decay of any radioactive isotopes in the ejected material. There are tools which would allow this investigation to be undertaken, however there was not time in this project to pursue this. Because of this, comment on the production of the p nuclei is limited in this work. In some burning regimes (see Figures 5.37 and 5.30) a significant increase in the abundances of a number of the p nuclei - ^{74}Se, ^{78}Kr, ^{84}Sr, ^{92}Mo, ^{94}Mo, ^{96}Rb and ^{98}Rb for $\dot{M} = 10^3 M_{\odot}/yr$ and r = 40 km and ^{74}Se, ^{78}Kr, ^{84}Sr or $\dot{M} = 10^4 M_{\odot}/yr$ and r = 10 km. It is possible that the material produced in these conditions are significantly

enhanced in p-nuclei after subsequent radioactive decay has been investigated. This would be a useful possibility to investigate, and fairly easy to accomplish with the data generated for completion of this project.

Further Work

Further observations are needed to identify possible other enhancements in the spectra of candidate stars. van Paradijs et al [58] suggest a number of elements which may be enhanced in the spectra of these stars, as do the results of this investigation.

In order to improve the accuracy of the predictions of this work, the specifics of the mixing mechanisms (if any) in the common envelope system should be investigated further - is it possible for material to be reprocessed in the atmosphere of the neutron star? What would the effect of this reprocessing be on the elemental abundances in the system? A complete hydrodynamics model of the accreting system, being considered by Deibel (private communication: 14th April, 2016) would ensure that the temperature and density conditions in the system were as close to the current best models as possible.

The effects of neutrino interactions in the accreted material will furthermore need to be addressed - will their presence cause a significant increase in the free neutrons in the system? Would those neutrons then have an effect on the burning processes in the system? Have the energy losses due to neutrinos been accounted for correctly?

Finally, studies of the formation and stability of the system would be needed to predict how much material will be processed and ejected over it's lifetime.

Possible alternative motions of the material could also be investigated, to motivate further study and development of a hydrodynamics model in order to fully describe the system.

There are many unknowns, however the consistent production in this system of the elements of interest in the Levesque paper suggest that further study may yield interesting results pertinent to the production of proton rich material in stellar environments.

Appendix A

Hydrodynamics Simulation

The full hydrodynamical simulation of the CENS system is likely to take many months to complete. This is due to the exceptionally high accretion rates being investigated in the system, and because of the length of time over which the system is stable - approximately a year. As such, the only available data produced during the duration of this project covers accretion rates up to $\approx 2\times$ the Eddington accretion rate and for less than $\frac{1}{10}$ of the lifetime of the system. Once the full simulation has been completed it would be very valuable to revisit the nucleosynthesis in this environment and compare the results of the hydrodynamical and analytical models.

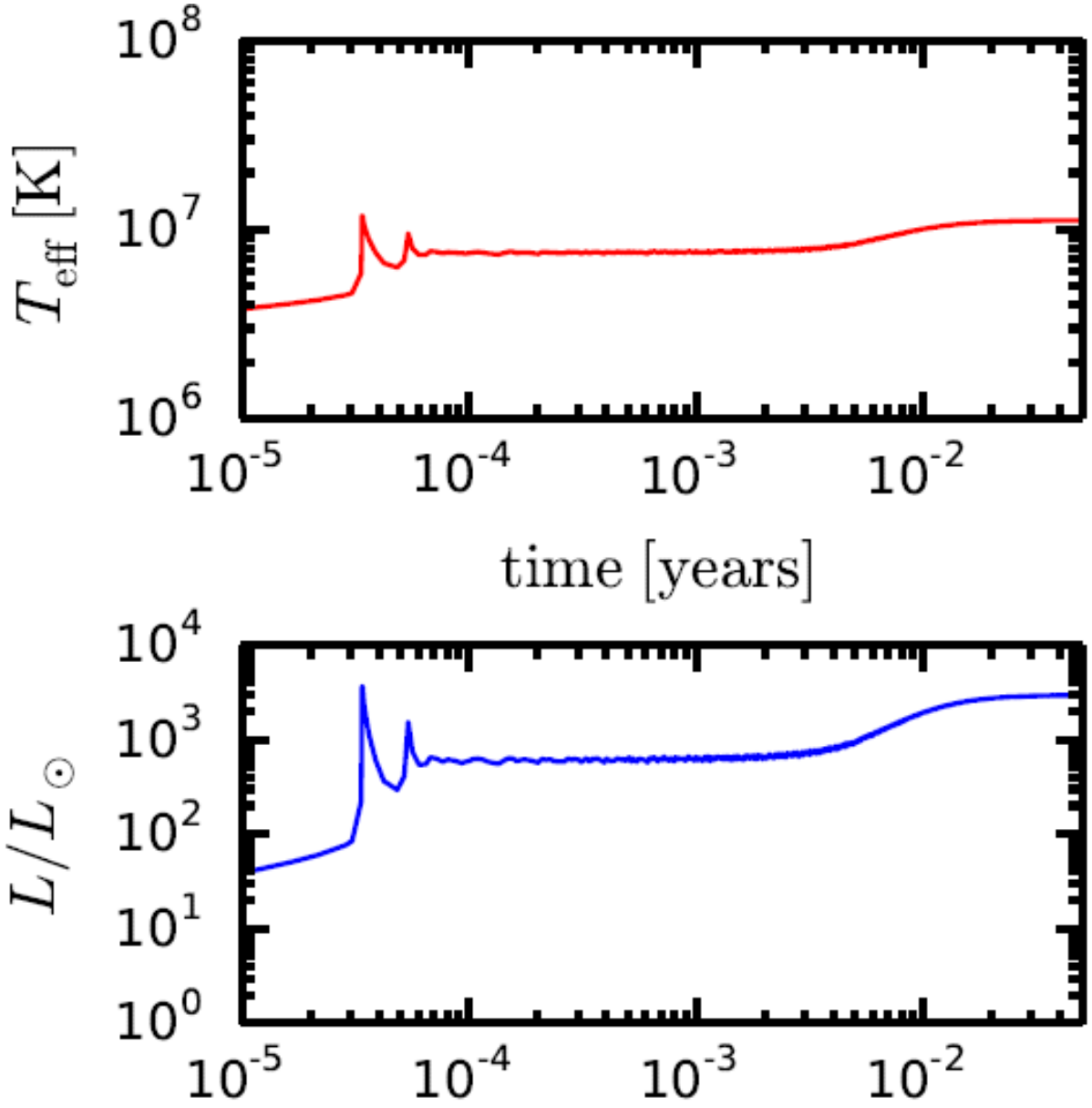

Figure A.1: Some of the work so far by Deibel modelling the CENS system. Temperatures are comparable with those found in the the presented model at, for example, $10^3 M_{sun}/yr$ and r = 50 km, representing some of the less extreme environments investigated. It is to be noted however that these results are only for accretion rates of 2$\times$ the Eddington and would therefore, presumably, be much higher for the higher accretion rates investigated in this project.

Appendix B

Additional Charts

Presented here are the first abundance charts for the r = 100 simulations. The broad difference in nucleosynthesis patterns illustrates the short burning time-scales experienced in most of the scenarios investigated in this thesis, and serves as justification for the choice of solar abundance as the metalicity of the accreted material as the abundance pattern in the simulations is quickly dominated by the choice of accretion rate (the first timestep is $\approx 8 \times 10^{-6}$s).

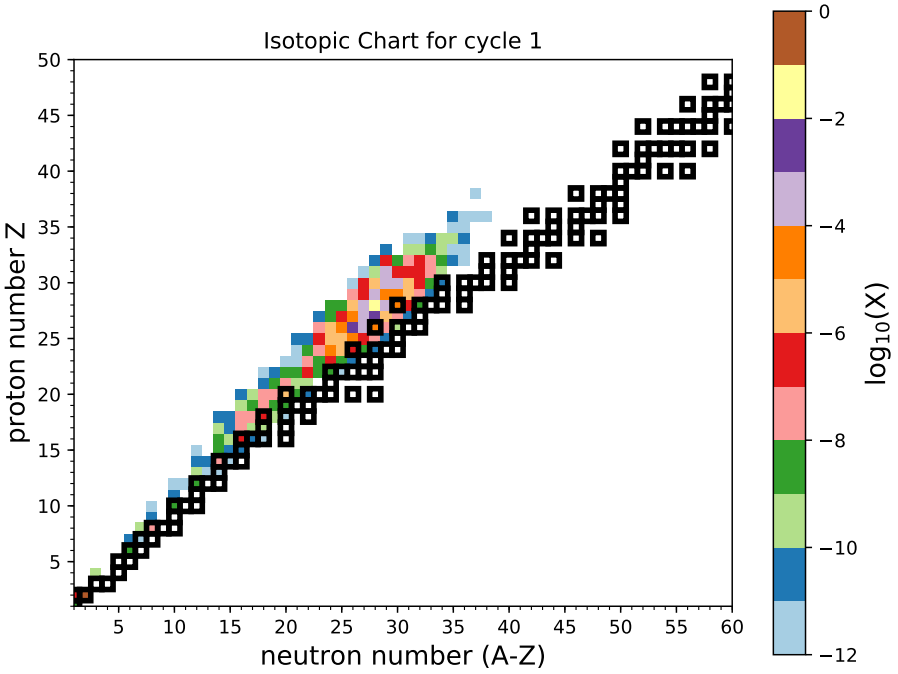

Figure B.1: Abundance chart for $\dot{\mathrm{M}} = 10^5 M_\odot/yr$

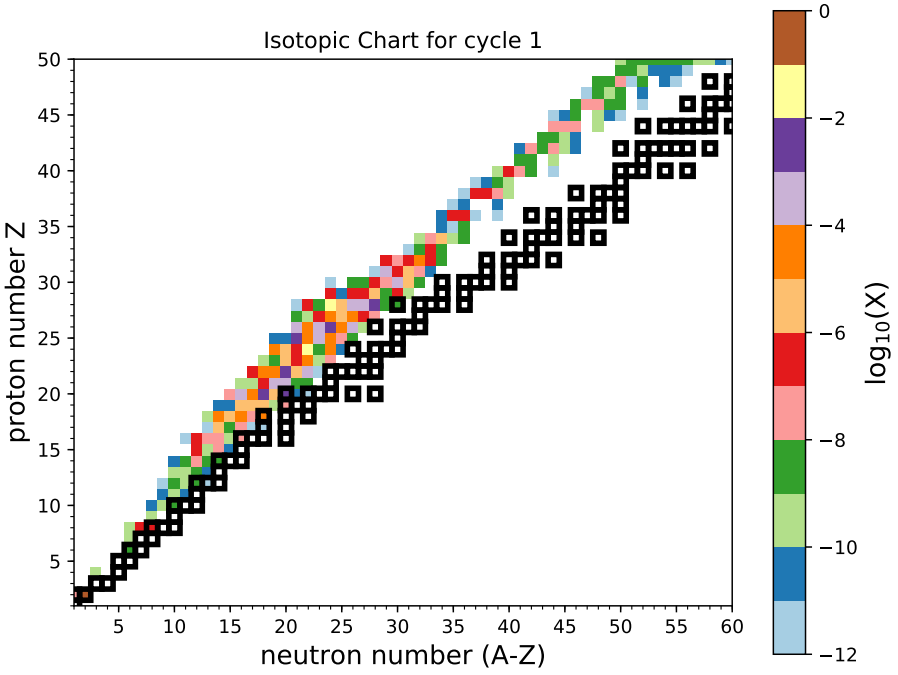

Figure B.2: Abundance chart for $\dot{\mathrm{M}} = 10^4 M_\odot/yr$

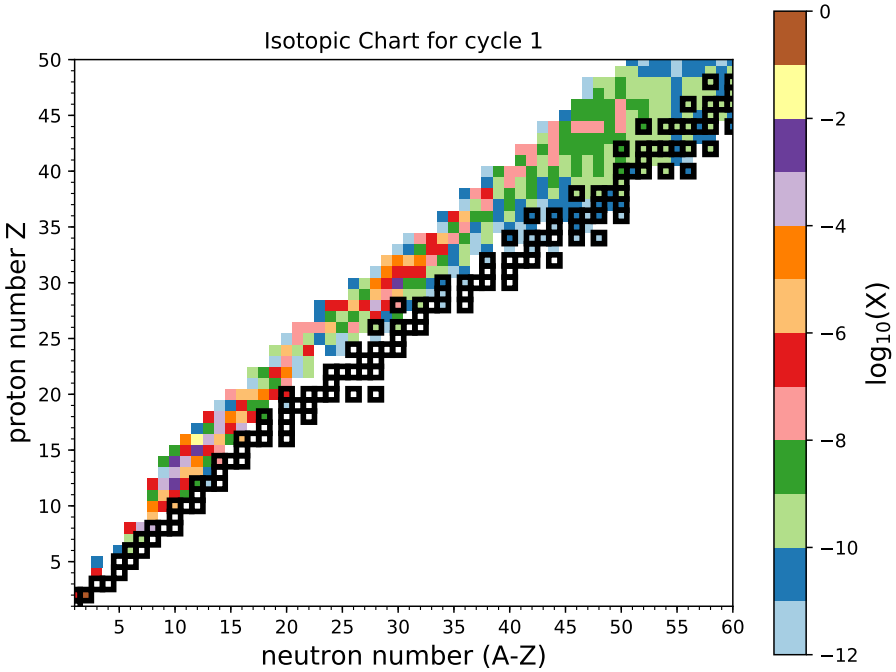

Figure B.3: Abundance chart for $\dot{M} = 10^3 M_\odot/yr$

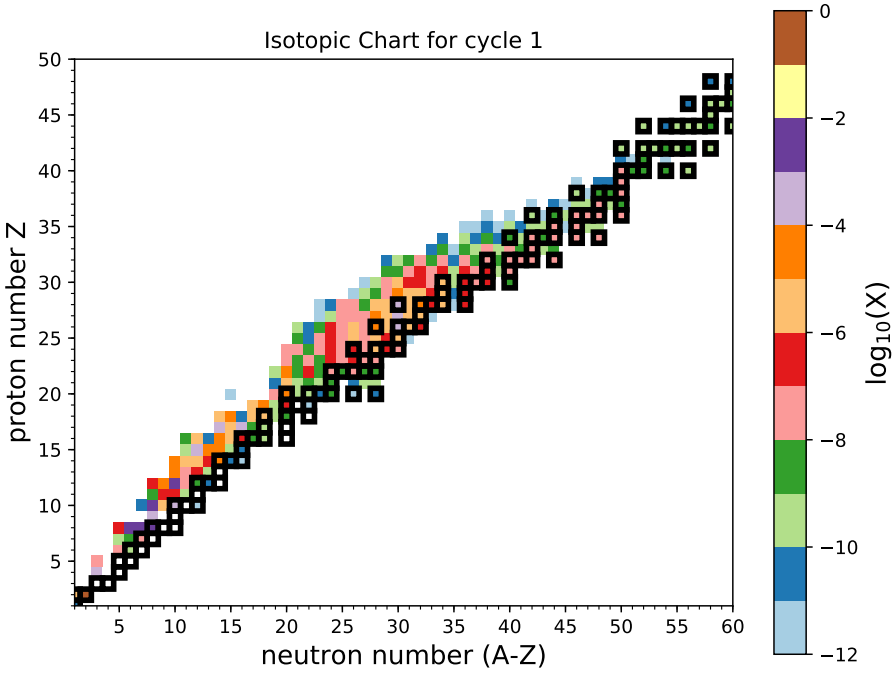

Figure B.4: Abundance chart for $\dot{M} = 10^2 M_\odot/yr$

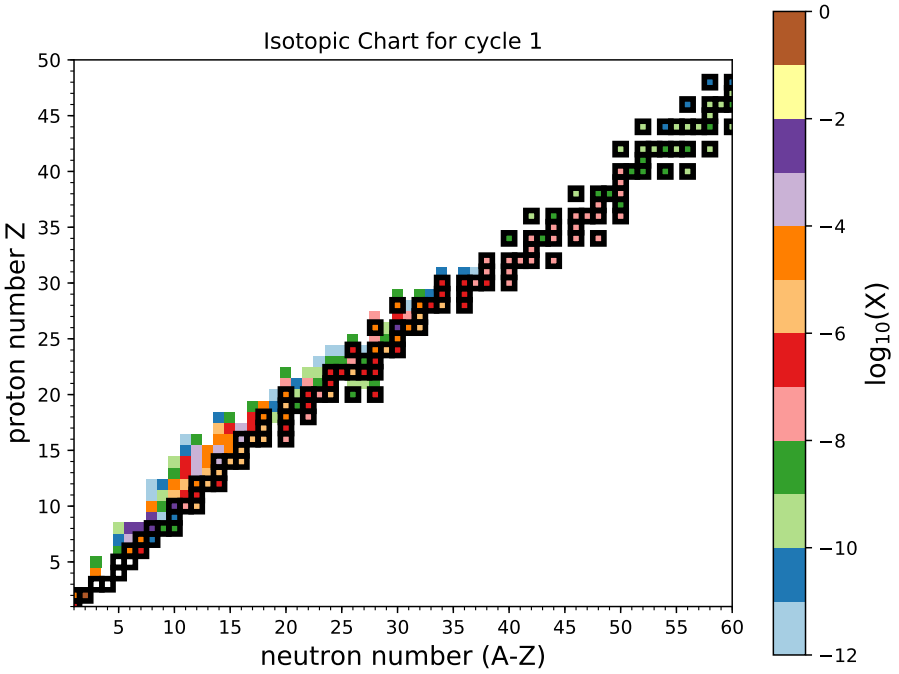

Figure B.5: Abundance chart for $\dot{\mathrm{M}} = 10^{1} M_{\odot}/yr$

Appendix C

Code For Modelling the CENS System

```
      rad=6.d6
      m_dot= 10e3

      mns= 1.4
      gamma= 4.0/3.0
      entropy= 5.5d3*((gamma+1)/2)**(0.75)*(gamma-1)/(gamma+1)* &
          mns**(7.0/8.0)*m_dot**(-0.25)
      print *, entropy

! Entropy calculated from work by Chevalier, taken from code from C.
! Fryer.
! Use Brunt-Vaisala frequency to describe the motion of the bubble of
! material.

      g=6.67d-8*mns*2.d33/1.d6**2
      N2=g/entropy*(1.d6)**(-11/8)
      tau=(1.d0/dsqrt(N2))

!     print *,g,N2,tau      ! Just to check that answers are consistent
                            ! betweeen codes and output is working as
                            ! expected.

! Set no_of_timesteps here - can be any number depending on how many
! cycles are required or how short the timesteps should be.

      no_of_timesteps=100
      dt=tau/no_of_timesteps
      t0=195/entropy*1.106d10
      rho0=3.9d15/entropy**3

! Loop over radii here:
!     do k=1,10
!         format_string="(A5,I0.3)"
!         write (filename, format_string)"trajectory",i
!         file_2=trim(filename)
!         open(unit=70,file=file_2,status='new')
!         rad=rad*k
      vel=0.9*dsqrt(6.67d-8*mns*2.d33/rad)
          do i=1,100
!         do i=1,no_of_timesteps ! for using variable timesteps
              write(70,*) dt*i,min(10.d0,t0*(1.d6/rad)/1.d9), &
              rho0*(1.d6/rad)**3
              rad=rad+vel*dt
! Many types of mixing available here. choose terms acordingly:
              if (i.lt.50) then
                  vel=0.9*dsqrt(6.67d-8*mns*2.d33/rad)
              else
                  vel=-0.9*dsqrt(6.67d-8*mns*2.d33/rad)
              end if
          end do
!         write(70,*)
!         close(70)
!     end do
      end program new_bubble
```


Figure C.1: Code used to produce trajectories for the common envelope system.

Bibliography

[1] Emily M. Levesque, Philip Massey, Anna N. Żytkow, and Nidia Morrell. Discovery of a thorne–Żytkow object candidate in the small magellanic cloud. *Monthly Notices of the Royal Astronomical Society: Letters*, 443(1):L94–L98, 2014.

[2] A Heger, CL Fryer, SE Woosley, N Langer, and DH Hartmann. How massive single stars end their life. *Astrophysical J*, 591(1):288, 2008.

[3] M Camenzind. *Compact Objects in Astrophysics: White Dwarfs, Neutron Stars and Black Holes*. Springer, 2007.

[4] MacLeod, Morgan and Ramirez-Ruiz, Enrico. ON THE ACCRETION-FED GROWTH OF NEUTRON STARS DURING COMMON ENVELOPE. *Astrophysical J Lett*, 798(1):L19, 2014.

[5] Roger A Chevalier. Neutron star accretion in a supernova. *The Astrophysical Journal*, 346:847–859, 1989.

[6] BP Abbott, R Abbott, R Adhikari, P Ajith, B Allen, G Allen, RS Amin, SB Anderson, WG Anderson, MA Arain, et al. Search for gravitational waves from low mass compact binary coalescence in 186 days of ligo's fifth science run. *Physical Review D*, 80(4):047101, 2009.

[7] Kenneth S Krane and David Halliday. *Introductory nuclear physics*, volume 465. Wiley New York, 1988.

[8] Christian Iliadis. *Nuclear physics of stars*. John Wiley & Sons, 2015.

[9] H Schatz, A Aprahamian, V Barnard, L Bildsten, A Cumming, M Ouellette, T Rauscher, F.-K. Thielemann, and M Wiescher. End point of the rp process on accreting neutron stars. *Phys Rev Lett*, 86(16):3471, 2001.

[10] Sandip K Chakrabarti, Liping Jin, and W David Arnett. Nucleosynthesis inside thick accretion disks around black holes. i-thermodynamic conditions and preliminary analysis. *The Astrophysical Journal*, 313:674–688, 1987.

[11] Marco Pignatari and Falk Herwig. The NuGrid research platform: A comprehensive simulation approach for nuclear astrophysics. *Nucl Phys News*, 22(4):18–23, 2012.

[12] E Margaret Burbidge, Geoffrey Ronald Burbidge, William A Fowler, and Fred Hoyle. Synthesis of the elements in stars. *Reviews of modern physics*, 29(4):547, 1957.

[13] RE Taam, P Bodenheimer, and JP Ostriker. Double core evolution. in a 16 solar mass star with a 1 solar mass neutron-star companion. *The Astrophysical Journal*, 222:269–280, 1978.

[14] Kip S Thorne and AN Zytkow. Red giants and supergiants with degenerate neutron cores. *The Astrophysical Journal*, 199:L19–L24, 1975.

[15] K So Thorne and AN Zytkow. Stars with degenerate neutron cores. i-structure of equilibrium models. *The Astrophysical Journal*, 212:832–858, 1977.

[16] Philipp Podsiadlowski, Robert C Cannon, and Martin J Rees. The evolution and final fate of massive thorne-żytkow objects. *Monthly Notices of the Royal Astronomical Society*, 274(2):485–490, 1995.

[17] Peter JT Leonard, Jack G Hills, and Rachel J Dewey. A new way to make thorne-zytkow objects. *The Astrophysical Journal*, 423:L19–L22, 1994.

[18] Thomas J Maccarone and Selma E de Mink. Large proper motion of the thorne–Żytkow object candidate HV 2112 reveals its likely nature as foreground galactic s-star. *Mon Notices Royal Astronomical Soc Lett*, 458(1):L1–L5, 2016.

[19] Clare C Worley, Mike J Irwin, Christopher A Tout, Anna N Żytkow, Morgan Fraser, and Robert G Izzard. The proper motion of HV2112: a TŻO candidate in the SMC. *Mon Notices Royal Astronomical Soc Lett*, 459(1):L31–L35, 2016.

[20] Emily M Levesque, Philip Massey, KAG Olsen, Bertrand Plez, Eric Josselin, Andre Maeder, and Georges Meynet. The effective temperature scale of galactic red supergiants: Cool, but not as cool as we thought. *Astrophysical J*, 628(2):973, 2008.

[21] Falk Herwig. EVOLUTION OF ASYMPTOTIC GIANT BRANCH STARS. *Annu Rev Astron Astr*, 43(1):435–479, 2005.

[22] C Georgy, S Ekström, G Meynet, P Massey, EM Levesque, R Hirschi, P Eggenberger, and A Maeder. Grids of stellar models with rotation. *Astron Astrophys*, 542:A29, 2012.

[23] A Mezzacappa, AC Calder, SW Bruenn, JM Blondin, MW Guidry, MR Strayer, and AS Umar. An investigation of neutrino-driven convection and the core collapse supernova mechanism using multigroup neutrino transport. *The Astrophysical Journal*, 495(2):911, 1998.

[24] Adam Burrows, Eli Livne, Luc Dessart, Christian D Ott, and Jeremiah Murphy. A new mechanism for core-collapse supernova explosions. *The Astrophysical Journal*, 640(2):878, 2006.

[25] BA Fryxell and W DAVID Arnett. Hydrodynamic effects of a stellar explosion on a binary companion star. *The Astrophysical Journal*, 243:994–1002, 1981.

[26] Vassiliki Kalogera. Orbital characteristics of binary systems after asymmetric supernova explosions. *The Astrophysical Journal*, 471(1):352, 1996.

[27] Vladimir Mikhailovich Lipunov. The astrophysics of neutron stars. *Astronomische Nachrichten Supplement*, 1, 1987.

[28] Nicolas Chamel, JM Pearson, Anthea Fantina, C Ducoin, Stéphane Goriely, and Alessandro Pastore. Brussels–montreal nuclear energy density functionals, from atomic masses to neutron stars. *Acta Physica Polonica B*, 46(3):349–358, 2015.

[29] Juhan Frank, Andrew King, and Derek Raine. *Accretion power in astrophysics*. Cambridge university press, 2002.

[30] Roger A Chevalier. Neutron star accretion in a stellar envelope. *The Astrophysical Journal*, 411:L33–L36, 1993.

[31] Chris L Fryer, Willy Benz, and Marc Herant. The dynamics and outcomes of rapid infall onto neutron stars. *Astrophysical J*, 460:801, 1996.

[32] SF Portegies Zwart and Lev R Yungelson. Formation and evolution of binary neutron stars. *Astronomy and Astrophysics*, 332:173–188, 1998.

[33] LIGO Scientific Collaboration. Ligo scientific collaborationhigher education resources. `http://www.ligo.org/students_teachers_public/highered.php`, note=Accessed: 30/12/2016.

[34] J Abadie, BP Abbott, Richard Abbott, TD Abbott, Matthew Abernathy, Timothee Accadia, Fausto Acernese, Carl Adams, Rana Adhikari, Christoph Affeldt, et al. Search for gravitational waves from low mass compact binary coalescence in ligo's sixth science run and virgo's science runs 2 and 3. *Physical Review D*, 85(8):082002, 2012.

[35] Donald D Clayton. *Principles of stellar evolution and nucleosynthesis*. University of Chicago press, 1968.

[36] EE Salpeter and HM Van Horn. Nuclear reaction rates at high densities. *The Astrophysical Journal*, 155:183, 1969.

[37] William A Fowler, Georgeanne R Caughlan, and Barbara A Zimmerman. Thermonuclear reaction rates. *Annual Review of Astronomy and Astrophysics*, 5:525, 1967.

[38] Christian Iliadis, John M D'Auria, Sumner Starrfield, William J Thompson, and Michael Wiescher. Proton-induced thermonuclear reaction rates for a= 20–40 nuclei. *The Astrophysical Journal Supplement Series*, 134(1):151, 2001.

[39] Alison Laird. Lecture notes nuclear atrophysics course, 2016.

[40] RK Wallace and SE Woosley. Explosive hydrogen burning. *Astrophysical J Suppl Ser*, 45:389, 1981.

[41] H. Schatz, A. Aprahamian, J. Görres, M. Wiescher, T. Rauscher, J.F. Rembges, F.-K. Thielemann, B. Pfeiffer, P. Möller, K.-L. Kratz, H. Herndl, B.A. Brown, and H. Rebel. rp-process nucleosynthesis at extreme temperature and density conditions. *Physics Reports*, 294(4):167 – 263, 1998.

[42] JL Fisker, V Barnard, J Görres, K Langanke, G Martínez-Pinedo, and MC Wiescher. Shell model based reaction rates for rp-process nuclei in the mass range a= 44–63. *Atomic Data and Nuclear Data Tables*, 79(2):241–292, 2001.

[43] L Van Wormer, J Görres, C Iliadis, M Wiescher, and F-K Thielemann. Reaction rates and reaction sequences in the rp-process. *The Astrophysical Journal*, 432:326–350, 1994.

[44] H. Schatz. The importance of nuclear masses in the astrophysical rp-process. *International Journal of Mass Spectrometry*, 251(2-3):293 – 299, 2006. ULTRA-ACCURATE {MASS} {SPECTROMETRY} {AND} {RELATED} {TOPICS} Dedicated to H.-J. Kluge on the occasion of his 65th birthday anniversaryJürgen Kluge Special Issue.

[45] H Herndl, J Görres, M Wiescher, BA Brown, and L Van Wormer. Proton capture reaction rates in the rp process. *Physical Review C*, 52(2):1078, 1995.

[46] BA Brown, RRC Clement, H Schatz, A Volya, and WA Richter. Proton drip-line calculations and the rp process. *Physical Review C*, 65(4):045802, 2002.

[47] J Ressler, A Piechaczek, W Walters, A Aprahamian, J Batchelder, C Bingham, D Brenner, T Ginter, C Gross, R Grzywacz, et al. Half-life for the rp-process waiting point nuclide 80zr using delayed gamma tagging. *The Nucleus: New Physics for the New Millennium*, page 463, 1999.

[48] A Wöhr, A Aprahamian, P Boutachkov, JL Galache, J Görres, M Shawcross, A Teymurazyan, MC Wiescher, DS Brenner, CN Davids, et al. The n= z rp-process waiting-point nucleus 68 se and its astrophysical implications. *Nuclear Physics A*, 742(3):349–362, 2004.

[49] Osamu Koike, Masa-aki Hashimoto, Reiko Kuromizu, and Shin-ichirou Fujimoto. Final products of the rp-Process on accreting neutron stars. *Astrophysical J*, 603(1):242, 2008.

[50] Stuart L Shapiro and Saul A Teukolsky. *Black holes, white dwarfs and neutron stars: the physics of compact objects*. John Wiley & Sons, 2008.

[51] Jordi José and Margarita Hernanz. Nucleosynthesis in classical novae: Co versus one white dwarfs. *The Astrophysical Journal*, 494(2):680, 1998.

[52] Anuj Parikh, Christian Iliadis, et al. The effects of variations in nuclear processes on type i x-ray burst nucleosynthesis. *The Astrophysical Journal Supplement Series*, 178(1):110, 2008.

[53] Liping Jin, W David Arnett, and Sandip K Chakrabarti. Nucleosynthesis inside thick accretion disks around black holes. ii-results for massive black holes. *The Astrophysical Journal*, 336:572–592, 1989.

[54] Shinya Wanajo. The rp-process in neutrino-driven winds. *The Astrophysical Journal*, 647(2):1323, 2006.

[55] H-Th Janka, K Langanke, A Marek, G Martínez-Pinedo, and B Müller. Theory of core-collapse supernovae. *Physics Reports*, 442(1):38–74, 2007.

[56] C Fröhlich, Gabriel Martinez-Pinedo, M Liebendörfer, F-K Thielemann, E Bravo, WR Hix, K Langanke, and Nikolaj Thomas Zinner. Neutrino-induced nucleosynthesis of a> 64 nuclei: the ν p process. *Physical Review Letters*, 96(14):142502, 2006.

[57] Jason Pruet, RD Hoffman, SE Woosley, H-T Janka, and R Buras. Nucleosynthesis in early supernova winds. ii. the role of neutrinos. *The Astrophysical Journal*, 644(2):1028, 2006.

[58] J Van Paradijs, HC Spruit, HJ Van Langevelde, and LBFM Waters. Strategies for detecting thorne-zytkow objects. *Astronomy and Astrophysics*, 303:L25, 1995.

[59] RC Cannon, PP Eggleton, AN Zytkow, and Ph Podsiadlowski. The structure and evolution of thorne-zytkow objects. *The Astrophysical Journal*, 386:206–214, 1992.

[60] NuGrid Collaboration. Nugrid project, 2016.

[61] Anuj Parikh, Jordi José, Fermín Moreno, and Christian Iliadis. The sensitivity of nucleosynthesis in type i x-ray bursts to thermonuclear reaction-rate variations. *New Astronomy Reviews*, 52(7):409–411, 2008.